

Dark Matter Working Group

recommendation for Two Higgs Doublet

Model (draft title)

Authorlist to be compiled: **Antonio Boveia,**^{3,*}
Caterina Doglioni,^{8,*} **Kristian Hahn,**^{14,*} **Ulrich Haisch,**^{15,16,*} **Steven**
Lowette,²² **Tim M.P. Tait,**^{25,*}

*DMWG organizers

³Ohio State University, 191 W. Woodruff Avenue Columbus, OH 43210

⁸Fysiska institutionen, Lunds universitet, Lund, Sweden

¹⁴Department of Physics and Astronomy, Northwestern University, Evanston, Illinois 60208,
USA

¹⁵Rudolf Peierls Centre for Theoretical Physics, University of Oxford, Oxford, OX1 3PN,
United Kingdom

¹⁶CERN, TH Department, CH-1211 Geneva 23, Switzerland

²²Physics Department, Vrije Universiteit Brussel, Brussels, Belgium

²⁵Department of Physics and Astronomy, University of California, Irvine, California 92697,
USA

Editor's E-mail: antonio.boveia@cern.ch, caterina.doglioni@cern.ch,
kristian.hahn@cern.ch, ulrich.haisch@physics.ox.ac.uk, ttait@uci.edu

Abstract. Draft abstract.

Contents

1	Introduction	1
2	Evolution of theories for LHC DM searches	2
3	Description of the 2HDM+a model	5
4	Constraints on the 2HDM+a parameter space	6
5	Comparison to other DM models	10
6	Model kinematics and mapping to existing models	12
6.1	Description of experimental searches	13
6.1.1	Signatures including a Higgs boson	13
6.1.2	Signatures including a Z boson	13
6.1.3	Signatures including heavy flavor quarks	14
6.2	Kinematic distributions justifying the choice of parameter scan	15
6.2.1	Masses of the A , H , and a bosons (M_A , M_H , and M_a)	15
6.2.2	Mixing angle between the two pseudoscalars A and a ($\sin \theta$)	18
6.2.3	Ratio of the doublet vacuum expectation values ($\tan \beta$)	19
6.2.4	Mass of DM fermion (M_χ)	22
6.3	Comparison with existing pseudoscalar models and recasting of HF+ E_T^{miss} search results	26
7	Parameter grid	29
8	Sensitivity studies	31
8.1	Studies of the $h(bb) + E_T^{\text{miss}}$ signature	31
8.2	Studies of the $Z+E_T^{\text{miss}}$ signature	35
8.3	Sensitivity of other signatures	37
8.3.1	Heavy flavor + E_T^{miss} signatures	37
8.3.2	Jet+ E_T^{miss} signature	37
9	Connection with cosmology	37
9.1	Technical setup	38
9.2	Results	38
10	Comparisons with non-collider experiments	41
10.1	Direct detection	41
10.2	Indirect detection	42
11	Conclusions	46

Appendix	46
A Details on MC generation	46
B Additional kinematic distributions	47
C Cross-section and acceptances for selected signatures	49
D Studies of other models of scalar sector	53
E Inert Doublet Model	53

1 Introduction

Reasoning behind this effort

- Simplified models only one signature at a time, sometimes not gauge invariant
- One step beyond this: less-simplified models
- Compare and confront different search sensitivity
- Combinations among different signatures
- Find new kinematic regimes / improve searches by exploring different signatures
- Still keeping the choice of model generic enough that this is reusable for theorists

Reasoning behind this effort

- Reasoning behind the choice of model
- Highlights more than one signature at a time, depending on parameters
- Leaves room for new unexplored kinematic signatures within existing searches (left for future work)
- Complete enough, still simplified so that one can choose grid planes
- Existing theory effort (HXSWG)

We investigate in detail the kinematics of three experimental signatures that are sensitive to this model:

- the Higgs+ E_T^{miss} signature, where the E_T^{miss} is produced by the decay of the pseudoscalar that couples to dark matter and the Higgs is produced either in association with this pseudoscalar or as a product of the decay of the second pseudoscalar;
- the Z+ E_T^{miss} signature, where the E_T^{miss} is produced by the decay of the pseudoscalar that couples to dark matter and the Z boson is either produced in association with this pseudoscalar or radiated by the heavy Higgs boson;

- the $t\bar{t}+E_T^{\text{miss}}$ signature, where pseudoscalar that couples to dark matter is produced in association with a $t\bar{t}$ pair or radiated by one of the top quarks.
-

The sensitivity of searches for this model in those signatures surpasses that of the jet+ E_T^{miss} searches, providing a motivation to explore their parameter space beyond the s -channel simplified models in [1].

Moreover, we identify a number of other signatures that have sensitivity to this model and can be studied in the future, such as ...

2 Evolution of theories for LHC DM searches

The experimental results of two of the three DM search strategies, namely direct and indirect detection, are commonly interpreted in the DM effective field theory (DM-EFT) framework. The operators in these DM-EFTs are build from SM fermions and DM fields. Schematically, one has in the case of spin-0 interactions and Dirac fermion DM

$$\mathcal{L}_{\text{DM-EFT}} = \sum_{f=u,d,\ell} \left(\frac{C_1^f}{\Lambda^2} \bar{f} f \bar{\chi} \chi + \frac{C_2^f}{\Lambda^2} \bar{f} \gamma_5 f \bar{\chi} \gamma_5 \chi + \dots \right), \quad (2.1)$$

where the ellipsis represents additional operators not relevant for the further discussion, the sum over $f = u, d, \ell$ includes all SM quarks and leptons, the DM candidate is called χ and γ_5 denotes the fifth Dirac matrix. The above DM-EFT is fully described by the parameters

$$\{m_\chi, C_n^f/\Lambda^2\}. \quad (2.2)$$

Here m_χ is the mass of the DM candidate, Λ is the suppression scale of the higher-dimensional operators and the C_n^f are the so-called Wilson coefficients. Notice that Λ and C_n^f are not independent parameters but always appear in the specific combination given in (2.2).

The DM-EFT approach is justified for the small momentum transfer $q^2 \ll \Lambda^2$ in DM-nucleon scattering (set by the non-relativistic velocities of DM in the halo) and in DM annihilation (set by the mass of the annihilating DM candidate). See Figure 1 for an illustration of the relevant scales in each experiment. Early articles [2–7] on DM searches at colliders quantify the reach of the LHC in the parameter space in terms of (2.2) and similar operators. The momentum transfer at the LHC is however larger than the suppression scale, i.e. $q^2 \gg \Lambda^2$, for many theories of DM. In this case, the mediator of the interaction between the dark sector and the SM can be resonantly produced and predictions obtained using the DM-EFT framework often turn out to be inaccurate (see for instance [5, 8–14] and [15, 16] for exceptions).

The kinematics of on-shell propagators can be captured in DM simplified models, which aim to represent a large number of extensions of the SM, while keeping only the

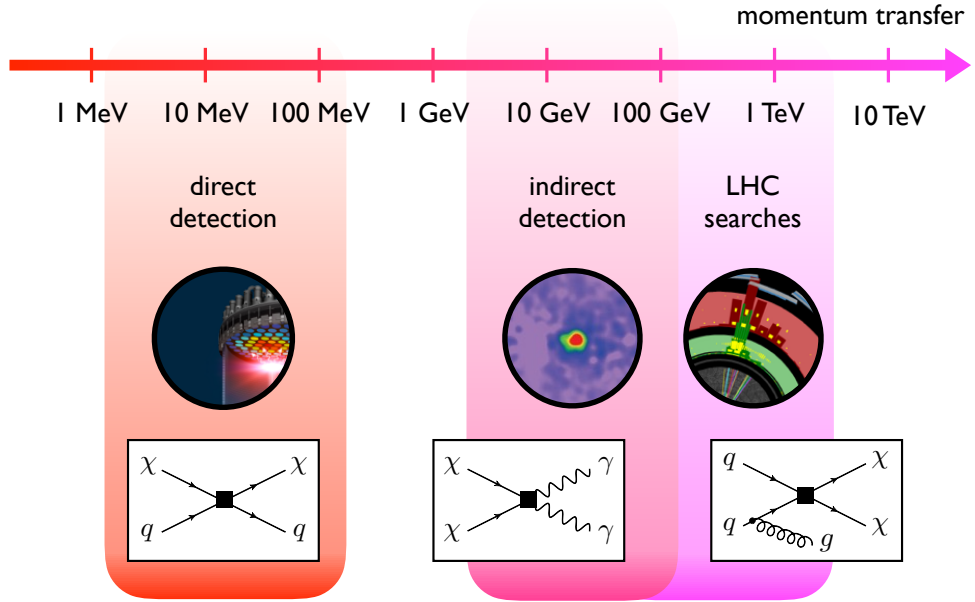


Figure 1: Range of momenta probed in direct-detection experiments, indirect-detection experiments and LHC searches. Prototypes of relevant Feynman diagrams are also shown.

degrees of freedom relevant for LHC phenomenology [17]. In the case of a pseudoscalar mediator a , the relevant DM-mediator and SM-mediator interactions read

$$\mathcal{L}_{\text{DM-SIMP}} = -ig_\chi a \bar{\chi} \gamma_5 \chi - ia \sum_j \left(g_u y_j^u \bar{u}_j \gamma_5 u_j + g_d y_j^d \bar{d}_j \gamma_5 d_j + g_\ell y_j^\ell \bar{\ell}_j \gamma_5 \ell_j \right), \quad (2.3)$$

with j representing a flavour index. Since the mediator a is a singlet it can also couple to itself and to $H^\dagger H$ where H denotes the SM Higgs doublet. The most general renormalisable scalar potential for a massive a is therefore

$$V_{\text{DM-SIMP}} = \frac{1}{2} m_a^2 a^2 + b_a a^3 + \lambda_a a^4 + b_H a H^\dagger H + \lambda_H a^2 H^\dagger H. \quad (2.4)$$

The parameters b_H and λ_H determine the couplings between the a and the H fields, thereby altering both the interactions and CP properties of the SM-like scalar h at 125 GeV as well as giving rise to possible new decay channels such as $h \rightarrow aa$ (see [18, 19] for details on the LHC phenomenology). Avoiding the resulting strong constraints for any choice of m_a , requires that $b_H \ll m_a$ and $\lambda_H \ll 1$. While the former requirement can be satisfied by imposing a Z_2 symmetry $a \rightarrow -a$, in the latter case one has to assume that λ_H is accidentally small if $m_a \lesssim 100$ GeV (cf. the related discussion on invisible decays of the Higgs boson in Section 4). Under such an assumption and noting that the self-coupling λ_a is largely irrelevant for collider phenomenology, the DM simplified model is fully described by the parameters

$$\{m_\chi, m_a, g_\chi, g_u, g_d, g_\ell\}. \quad (2.5)$$

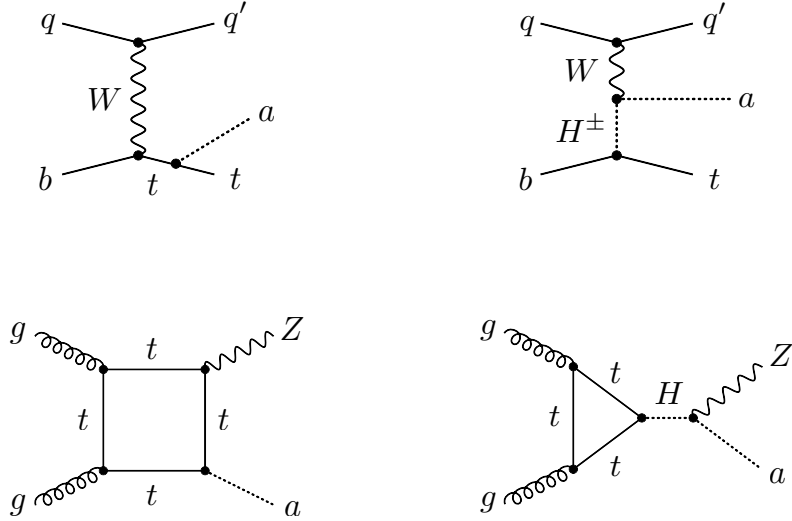


Figure 2: Diagrams contributing to the $qb \rightarrow q'ta$ (upper row) and $gg \rightarrow Za$ (lower row) scattering processes. Only the graphs on the left-hand side appear in the DM simplified model with a pseudoscalar, while in the 2HDM+a model in addition the diagrams on the right-hand side are present. See text for further details.

In fact, in the limit of infinite mediator mass $m_a \rightarrow \infty$, the DM-SIMP Lagrangian (2.3) matches onto the DM-EFT Lagrangian (2.1). The corresponding tree-level matching conditions are $C_2^f/\Lambda^2 = g_\chi g_f y_f / m_a^2$ and $C_n^f = 0$ for all other Wilson coefficients.

Unfortunately, the operators in both $\mathcal{L}_{\text{DM-EFT}}$ and $\mathcal{L}_{\text{DM-SIMP}}$ violate gauge invariance, because the left- and right-handed SM fermions belong to different representations of the SM gauge group. In the case of the DM-EFT this suggests the Wilson coefficients C_n^f introduced in (2.1) actually scale as $C_n^f = c_n^f m_{f_i} / \Lambda$ [20], whereas for the DM simplified model restoring gauge invariance requires the embedding of the mediator a into an electroweak (EW) multiplet. The absence of gauge invariance leads to unitarity-violating amplitudes in DM simplified models (cf. [20–23]). In the case of the DM simplified model described by (2.3), one can show for instance that the amplitudes $\mathcal{A}(qb \rightarrow q'ta) \propto \sqrt{s}$ and $\mathcal{A}(gg \rightarrow Za) \propto \ln^2 s$ diverge in the limit of large center-of-mass energy s . The Feynman diagrams that lead to this behaviour are depicted on the left-hand side in Figure 2. Similar singularities appear in other single-top processes and in the mono-Higgs case. Since the divergences are not power-like, weakly-coupled realisations of (2.3) do not break down for the energies accessible at the LHC. The appearance of the \sqrt{s} and $\ln^2 s$ terms however signals the omission of diagrams that would be present in any gauge-invariant extension that gives rise to $\mathcal{L}_{\text{DM-EFT}}$ in the limit where all additional particles are heavy. For example, the $pp \rightarrow tja$ cross section is made finite by the exchange of a charged Higgs H^\pm , while in the case of $pp \rightarrow Za$ an additional scalar H unitarises the amplitude. The corresponding diagrams are displayed on the right in Figure 2. Notice that the cancellation of unitarity-violating terms among the diagrams of the latter figure is not at all accidental, but a direct

consequence of the local gauge invariance of the underlying model.

The additional degrees of freedom necessary to unitarise the amplitudes cannot be arbitrarily heavy and hence may change the phenomenology of the DM simplified model. In fact, as can be seen from Figure 2, the presence of the H^\pm (H) allows to produce a mono-top (mono- Z) signal resonantly. Since resonant production is strongly enhanced compared to initial state radiation, the importance of the various mono- X signals in the extended DM model may then differ from the simplified model predictions [24–26]. In fact, we will see that in a specific extension of (2.3) called 2HDM+a model, the mono- Z , mono-Higgs and $tX + E_T^{\text{miss}}$ signals can be as or even more important than the mono-jet and $t\bar{t} + E_T^{\text{miss}}$ channel, which are the leading missing transverse energy (E_T^{miss}) signatures in the DM simplified pseudoscalar model [27–31]. We emphasise that the embedding of (2.3) is not unique, since both the mediator and the DM particle can belong to different EW multiplets. In this whitepaper, we consider the simplest embedding with a single SM-singlet DM candidate, which captures the maximal number of interesting $E_{T,\text{miss}}$ signatures. We will briefly comment on other possible embeddings and related DM models in Section 5.

3 Description of the 2HDM+a model

The 2HDM+a model is a two Higgs doublet model (2HDM) that contains, besides the Higgs doublets H_1 and H_2 , an additional pseudoscalar singlet P . It is the simplest renormalisable extension of (2.3) with a SM-singlet DM candidate [24, 25, 32–34]. The gauge symmetry is made manifest by coupling the P to the dark Dirac fermion χ via

$$\mathcal{L}_\chi = -iy_\chi P\bar{\chi}\gamma_5\chi, \quad (3.1)$$

while the Higgs doublets couple to the SM fermions through

$$\mathcal{L}_Y = -\sum_{i=1,2} \left(\bar{Q}Y_u^i \tilde{H}_i u_R + \bar{Q}Y_d^i H_i d_R + \bar{L}Y_\ell^i H_i \ell_R + \text{h.c.} \right). \quad (3.2)$$

Here y_χ is a dark-sector Yukawa coupling, Y_f^i are Yukawa matrices acting on the three fermion generations and we have suppressed flavour indices, Q and L are left-handed quark and lepton doublets, while u_R , d_R and ℓ_R are right-handed up-type quark, down-type quark and charged lepton singlets, respectively. Finally, $\tilde{H}_i = \epsilon H_i^*$ with ϵ denoting the two-dimensional antisymmetric tensor.

The particle that mediates the interactions between the dark sector and the SM is a superposition of the CP-odd components of H_1 , H_2 and P . We impose a Z_2 symmetry under which $H_1 \rightarrow H_1$ and $H_2 \rightarrow -H_2$, such that only one Higgs doublet appears in each operator in \mathcal{L}_Y . The different ways to construct these operators result in different Yukawa structures and in this whitepaper we will, for concreteness, consider only the so-called type-II 2HDM. This specific choice corresponds to setting $Y_u^1 = Y_d^2 = Y_\ell^2 = 0$ in (3.2). The Z_2 symmetry is the minimal condition necessary to guarantee the absence of flavour-changing neutral currents (FCNCs) at tree-level [35, 36] and such a symmetry is realised in many well-motivated complete ultraviolet (UV) theories in the form of supersymmetry, a $U(1)$ symmetry or a discrete symmetry acting on the Higgs doublets. We further choose

all parameters in the scalar potential real, such that CP eigenstates are identified with the mass eigenstates, i.e. two scalars h and H , two pseudoscalars A and a and a charged scalar H^\pm . Under these conditions, the most general renormalisable scalar potential can be written as

$$V = V_H + V_{HP} + V_P, \quad (3.3)$$

with the potential for the two Higgs doublets

$$\begin{aligned} V_H = & \mu_1 H_1^\dagger H_1 + \mu_2 H_2^\dagger H_2 + (\mu_3 H_1^\dagger H_2 + \text{h.c.}) + \lambda_1 (H_1^\dagger H_1)^2 + \lambda_2 (H_2^\dagger H_2)^2 \\ & + \lambda_3 (H_1^\dagger H_1)(H_2^\dagger H_2) + \lambda_4 (H_1^\dagger H_2)(H_2^\dagger H_1) + [\lambda_5 (H_1^\dagger H_2)^2 + \text{h.c.}], \end{aligned} \quad (3.4)$$

potential terms which connect doublets and singlets

$$V_{HP} = P (ib_P H_1^\dagger H_2 + \text{h.c.}) + P^2 (\lambda_{P1} H_1^\dagger H_1 + \lambda_{P2} H_2^\dagger H_2), \quad (3.5)$$

and the singlet potential

$$V_P = \frac{1}{2} m_P^2 P^2. \quad (3.6)$$

Notice that compared to [24, 32–34] which include only the trilinear portal coupling b_P , we follow [25] and also allow for quartic portal interactions proportional to λ_{P1} and λ_{P2} . A quartic self-coupling P^4 has instead not been included in (3.6), because such a term would not lead to any relevant effect in the E_T^{miss} observables studied in this whitepaper.

Upon rotation to the mass eigenbasis, we trade the five dimensionful and the eight dimensionless parameters in the potential for physical masses and mixing angles and four quartic couplings:

$$\left\{ \begin{array}{l} \mu_1, \mu_2, \mu_3, b_P, m_P, m_\chi \\ y_\chi, \lambda_1, \lambda_2, \lambda_3, \lambda_4, \lambda_5, \\ \lambda_{P1}, \lambda_{P2} \end{array} \right\} \longleftrightarrow \left\{ \begin{array}{l} v, M_h, M_A, M_H, M_{H^\pm}, M_a, m_\chi \\ \cos(\beta - \alpha), \tan \beta, \sin \theta, \\ y_\chi, \lambda_3, \lambda_{P1}, \lambda_{P2} \end{array} \right\}. \quad (3.7)$$

The parameters shown on the right-hand side of (3.7) will be used as input in the following. Out of these parameters, the EW vacuum expectation value (VEV) $v \simeq 246$ GeV and the mass of the SM-like CP-even mass eigenstate $M_h \simeq 125$ GeV are already fixed by observations. The experimental and theoretical constraints on the remaining parameter space will be examined in the next section.

4 Constraints on the 2HDM+a parameter space

In the following we examine the constraints on the input parameters (3.7) that arise from Higgs and flavour physics, LHC searches for additional Higgses, EW precision measurements and vacuum stability considerations. The discussed constraints will motivate certain parameter benchmarks. These will be summarised at the end of the section.

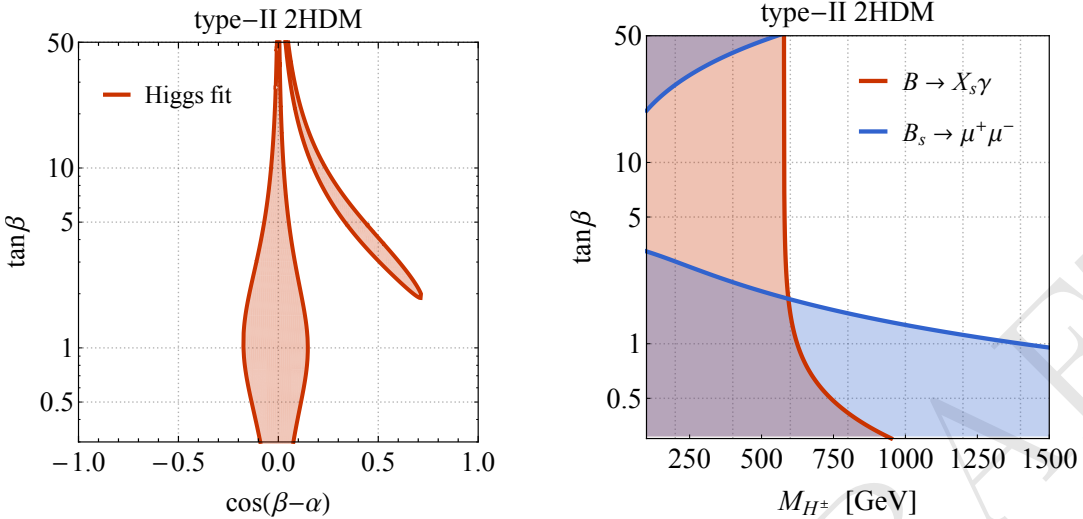


Figure 3: Left: Parameter space allowed by a global fit to the LHC Run-I Higgs coupling strength measurements. The lines show the contours which restrict the allowed parameter space at the 95% CL for a type-II 2HDM. Right: Parameter space in the M_{H^\pm} – $\tan\beta$ plane that is disfavoured by the flavour observables $B \rightarrow X_s\gamma$ (red) and $B_s \rightarrow \mu^+\mu^-$ (blue). The uncoloured region in the upper right corner of the plot is allowed at 95% CL.

Constraints on $\cos(\beta - \alpha)$

The mixing angle α between the CP-even scalars h and H is constrained by Higgs coupling strength measurements and we display the regions in the $\cos(\beta - \alpha)$ – $\tan\beta$ plane that are allowed by the LHC Run-I combination [37] in the left panel of Figure 3. The shown 95% confidence level (CL) contour has been obtained in the type-II 2HDM. One observes that for arbitrary values of $\tan\beta$ only parameter choices with $\cos(\beta - \alpha) \simeq 0$ are experimentally allowed. To avoid the constraints from Higgs physics and to simplify the further analysis, we will concentrate in this whitepaper on the so-called alignment limit of the 2HDM where $\cos(\beta - \alpha) = 0$ [38], treating $\tan\beta$ as a free parameter.

Constraints on $\tan\beta$

Indirect constraints on $\tan\beta$ as a function of M_{H^\pm} arise from $B \rightarrow X_s\gamma$ [39–41], B -meson mixing [42–45] as well as $B_s \rightarrow \mu^+\mu^-$ [46–52], but also follow from $Z \rightarrow b\bar{b}$ [53–55]. For the case of the type-II 2HDM, the most stringent constraints on the M_{H^\pm} – $\tan\beta$ plane are depicted in the right panel of Figure 3. From the shown results it is evident that $B \rightarrow X_s\gamma$ provides a lower limit on the charged Higgs mass of $M_{H^\pm} > 580$ GeV that is practically independent of $\tan\beta$ for $\tan\beta \gtrsim 2$, while $B_s \rightarrow \mu^+\mu^-$ is the leading constraint for very heavy charged Higgses, excluding for instance values of $\tan\beta < 1.3$ for $M_{H^\pm} = 1$ TeV. As discussed in [25], the constraints on $\tan\beta$ that follow from the existing LHC searches for heavy Higgses (see for instance [56–59]) are at the moment all weaker than the limits provided by flavour physics. Since the indirect constraints arise from loop corrections they can in principle be weakened by the presence of additional particles that are too heavy to

be produced at the LHC. We thus consider the bounds from flavour only as indicative, and will not directly impose them on the parameter space of the 2HDM+a in what follows.

Constraints on $\sin \theta$

EW precision measurements constrain the splittings between the masses M_H, M_A, M_{H^\pm} and M_a , since the exchange of spin-0 states modifies the propagators of the W - and Z -bosons at the one-loop level and beyond. For $M_H = M_{H^\pm}$ and $\cos(\beta - \alpha) = 0$, these corrections vanish due to a custodial symmetry in the tree-level potential V_H [60–64] introduced in (3.4) and the masses of the CP-odd mass eigenstates can be treated as free parameters. This custodial symmetry is also present if $M_A = M_{H^\pm}$ and $\cos(\beta - \alpha) = 0$, but the presence of the pseudoscalar mixing term in (3.5) breaks this symmetry softly [25]. As a result, the pseudoscalar mixing angle θ and the mass splitting between M_H, M_A and M_a are constrained in such a case. An illustrative example of the resulting constraints is given in the left panel of Figure 4. To keep $\sin \theta$ and M_a as free parameters, we consider below only 2HDM+a model realisations in which the masses of the H, A and H^\pm are equal. Notice that the choice $M_H = M_A = M_{H^\pm}$ is also adopted in some 2HDM interpretations of the searches for heavy spin-0 resonances performed at the LHC (cf. [65–67] for example).

Constraints on M_a

Invisible decays of the Higgs boson allow to set a lower limit on the mass of the pseudoscalar a in 2HDM+a scenarios with light DM [25]. In the case of $m_\chi = 1$ GeV, it turns out for instance that mediator mass $M_a \lesssim 100$ GeV are excluded by imposing the 95% CL limit $\text{BR}(h \rightarrow \text{invisible}) \lesssim 25\%$ [68, 69]. This limit is largely independent of the choices of the other parameters since $\text{BR}(h \rightarrow \text{invisible}) \simeq \text{BR}(h \rightarrow aa^* \rightarrow 2\chi 2\bar{\chi}) \simeq 100\%$ for sufficiently light DM. To evade the limits from invisible Higgs decays, we consider in this whitepaper only a masses larger than 100 GeV when studying E_T^{miss} signatures at the LHC.

Constraints on λ_3

The requirement that the scalar potential (3.3) of the 2HDM+a is bounded from below (BFB), restricts the possible choices of the Higgs masses, mixing angles and quartic couplings. Assuming that $\lambda_{P1}, \lambda_{P2} > 0$, it is easy to see that the BFB conditions in the 2HDM+a are identical to those found in the pure 2HDM [38]. For our choice $M_H = M_A = M_{H^\pm}$ of heavy Higgs masses, one finds that the tree-level BFB conditions can be cast into two inequalities. The first inequality connects λ_3 with the cubic SM Higgs self-coupling $\lambda = M_h^2/(2v^2) \simeq 0.13$ and simply reads

$$\lambda_3 > 2\lambda. \quad (4.1)$$

The second BFB condition relates λ_3 with $\tan \beta, \sin \theta$, the common heavy Higgs mass M_H and M_a and turns out to be more complicated. In the limit $M_H \gg M_h, M_a$ it however takes a rather simple form that we quote here for illustration:

$$\lambda_3 > \frac{M_H^2 - M_a^2}{v^2} \sin^2 \theta - 2\lambda \cot^2(2\beta). \quad (4.2)$$

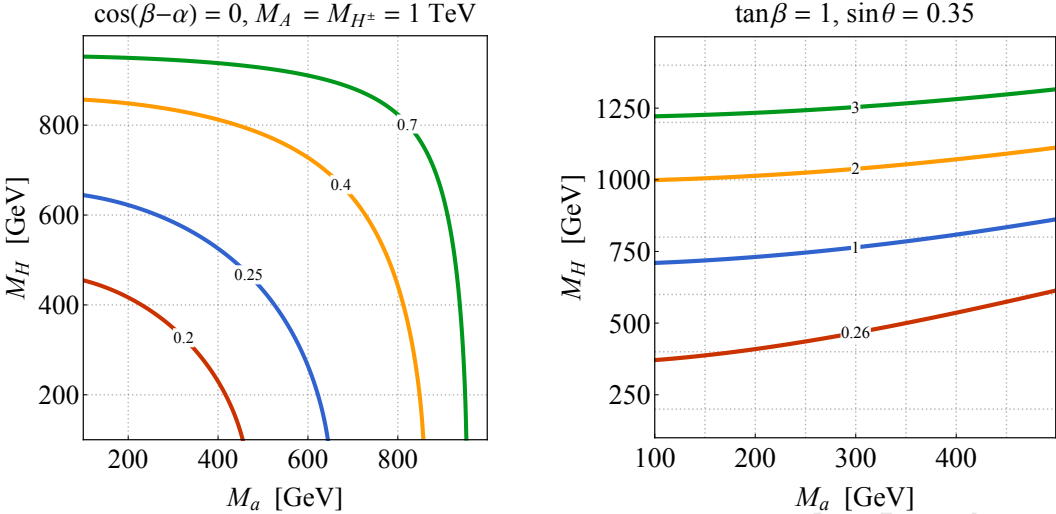


Figure 4: Left: Values of M_a and M_H allowed by EW precision constraints assuming $\cos(\beta - \alpha) = 0$, $M_A = M_{H^\pm} = 1 \text{ TeV}$ and four different values of $\sin \theta$, as indicated by the contour labels. The parameter space below and to the left of the contours is excluded. Right: Constraints in the $M_a - M_H$ plane following from the requirements of having a BFB 2HDM+a scalar potential. The shown results correspond to $\tan \beta = 1$, $\sin \theta = 0.35$ and degenerate heavy Higgs masses $M_H = M_A = M_{H^\pm}$. The region above each contour is excluded for the indicated value of λ_3 .

This formula in essence implies that large values of $M_H^2/v^2 \sin^2 \theta$ are only compatible with the requirements from BFB if the quartic coupling λ_3 is sufficiently large. Notice that the interplay between BFB and perturbativity of λ_3 , i.e. $\lambda_3 < 4\pi$, leads to a non-decoupling of H, A and H^\pm for $|M_H - M_a| \neq 0$ and $\sin \theta \neq 0$ [24] such that the spin-0 states are potentially within LHC reach. The right plot in Figure 4 which shows the constraints in the $M_a - M_H$ plane that derive from the exact version of (4.2) puts the latter statement on solid ground. From the figure one observes that for $\tan \beta = 1$, $\sin \theta = 0.35$ and $M_H = M_A = M_{H^\pm}$, values of $\lambda_3 \gtrsim 2$ are needed in order for $M_H \simeq 1 \text{ TeV}$ to be allowed by BFB. Notice that due to the $\sin^2 \theta$ dependence in (4.2), close to non-perturbative couplings $\lambda_3 \gtrsim 8$ would be required to make 1 TeV 2HDM Higgses viable for larger pseudoscalar mixing angle of $\sin \theta = 0.7$. In order for heavy Higgs above 1 TeV to be acceptable while keeping λ_3 perturbative, we will choose $\sin \theta = 0.35$ and $\lambda_3 = 3$ as our benchmark in this whitepaper.

Constraints on λ_{P1} and λ_{P2}

The quartic couplings λ_3 , λ_{P1} and λ_{P2} affect all cubic Higgs interactions. In the case of the Haa and Aah couplings, one obtains under the assumption that $\cos(\beta - \alpha) = 0$ and

$M_H = M_A = M_{H^\pm}$, the following expressions [25]

$$\begin{aligned} g_{Haa} &= \frac{1}{M_H v} \left[\cot(2\beta) (2M_h^2 - 2\lambda_3 v^2) \sin^2 \theta + \sin(2\beta) (\lambda_{P1} - \lambda_{P2}) v^2 \cos^2 \theta \right], \\ g_{Aah} &= \frac{1}{M_H v} \left[M_h^2 + M_H^2 - M_a^2 - 2\lambda_3 v^2 + 2(\lambda_{P1} \cos^2 \beta + \lambda_{P2} \sin^2 \beta) v^2 \right] \sin \theta \cos \theta. \end{aligned} \quad (4.3)$$

Because $\Gamma(H \rightarrow aa) \propto g_{Haa}^2$ and $\Gamma(A \rightarrow ah) \propto g_{Aah}^2$, the relations (4.3) imply that in order to keep the total widths Γ_H and Γ_A small, parameter choices of the form $\lambda_3 = \lambda_{P1} = \lambda_{P2}$ are well suited.

Benchmark parameter choices

The above discussion motivates the following choice of parameters

$$\begin{aligned} M_H &= M_A = M_{H^\pm}, \quad m_\chi = 10 \text{ GeV}, \\ \cos(\beta - \alpha) &= 0, \quad \tan \beta = 1, \quad \sin \theta = 0.35, \\ y_\chi &= 1, \quad \lambda_3 = \lambda_{P1} = \lambda_{P2} = 3. \end{aligned} \quad (4.4)$$

In these type-II 2HDM+a benchmark scenarios the only free parameters are then

$$\{M_H, M_a\}, \quad (4.5)$$

and the results of our E_T^{miss} sensitivity studies will always be presented in the corresponding two-dimensional parameter plane.

We emphasise that small departures from the above parameter choices will lead to a qualitatively similar mono- X phenomenology in the 2HDM+a model. The signatures that are most sensitive to the mass splitting between the H and the A , the parameter $\sin \theta$ and the quartic couplings $\lambda_3, \lambda_{P1}, \lambda_{P2}$ turn out to be the mono- Z and mono-Higgs channels. Four benchmark scenarios that illustrate these model dependences have been proposed and studied in [25]. We believe that the specific benchmark chosen in this whitepaper nicely exemplifying the rich structure of E_T^{miss} signatures in the 2HDM+a model, and the choices (4.4) should therefore serve well as a starting point for further more detailed experimental and theoretical investigations.

As a final validation (or first application) of the proposed benchmark scenario, we present in Figure 5 the predictions for the ratios Γ_H/M_H (left) and Γ_A/M_A (right). We see that the heavy neutral Higgs states H and A are relatively narrow even for values $M_H > 1 \text{ TeV}$ and $M_a = 100 \text{ GeV}$. The narrow width approximation (NWA) is thus applicable in the entire parameter space considered in our $M_a - M_H$ scans.

5 Comparison to other DM models

In this section we briefly discuss DM models that also feature a 2HDM sector. Our discussion will focus on the similarities and differences between these scenarios and the 2HDM+a model for what concerns the mono- X phenomenology.

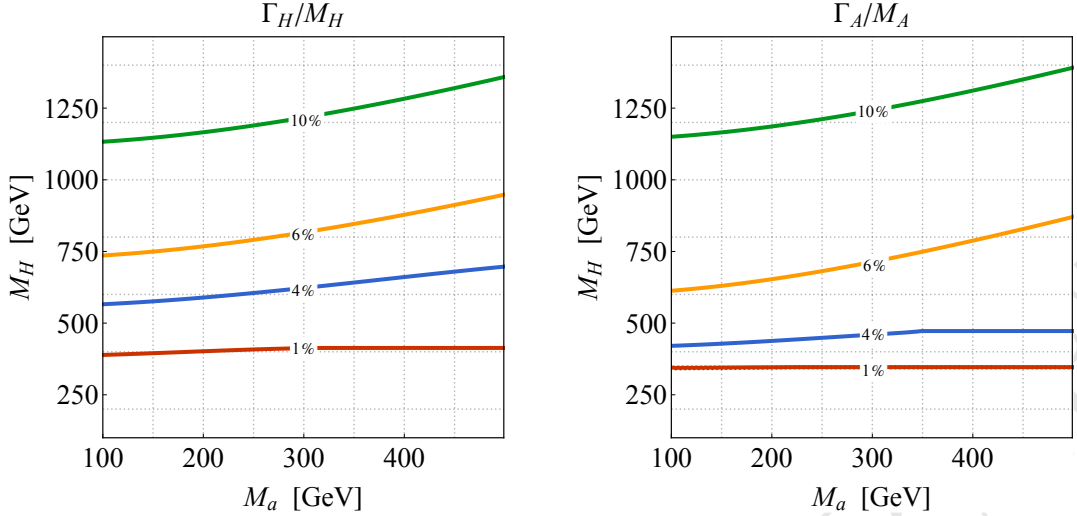


Figure 5: Predictions for Γ_H/M_H (left panel) and Γ_A/M_A (right panel). The shown results correspond to the type-II 2HDM+a benchmark parameter choices given in (4.4).

2HDM with an extra scalar singlet

Instead of mixing an additional CP-odd singlet P with the pseudoscalar A , as done in (3.5), it is also possible to consider the mixing of a scalar singlet S with the CP-odd spin-0 states h, H . Detailed studies of the direct-detection and relic-density phenomenology of this so-called 2HDM+s model have been presented in [70, 71]. Like in the case of the 2HDM+a model, the presence of non-SM Higgs bosons in the 2HDM+s model can lead to novel E_T^{miss} signatures that are not captured by a simplified DM model with just a single scalar mediator. In the pure alignment limit, the most interesting collider signals are mono- Z , mono-Higgs and the $tX + E_T^{\text{miss}}$ channels, because these signatures can all arise resonantly. Away from alignment, the scalar mediator couples to the EW gauge bosons and as a result it may also be possible to have a sizeable amount of E_T^{miss} in association with a Z or W boson or in vector boson fusion (VBF). Notice that due to the CP properties of the a the latter E_T^{miss} signatures are not present in the 2HDM+a model.

2HDM with doublet-singlet DM

In both the 2HDM+a and the 2HDM+s model the DM particle is a EW singlet. The DM particle may however also be a mixture of a EW singlet and doublet(s) [72–75], as in the minimal supersymmetric SM where it has both bino and higgsino components. Generically, this is referred to as singlet-doublet DM. The phenomenology of 2HDM models with singlet-doublet DM has been discussed in [76, 77]. In these works only the $b + E_T^{\text{miss}}$ and $t\bar{t} + E_T^{\text{miss}}$ signatures have been considered and found to provide only weak constraints. The recent study [78] suggests that stronger constraints may arise in the 2HDM with doublet-singlet DM from $Z + E_T^{\text{miss}}$ and $tX + E_T^{\text{miss}}$ searches. This feature warrants further investigations.

2HDM with higher-dimensional couplings to DM

A gauge-invariant DM model where a pseudoscalar is embedded into a 2HDM that has renormalisable couplings to SM fields but an effective coupling to DM via the dimension-five operator $H_1^\dagger H_2 \bar{\chi} \gamma_5 \chi$ has been discussed in [78]. It has been shown that such an effective DM coupling can be obtained in different UV completions such as the 2HDM+a model or a 2HDM with doublet-singlet DM by integrating out heavy particles. Apart from the $tX + E_T^{\text{miss}}$ signatures, the whole suit of mono- X signals has been considered in [78]. It was found that a resonant mono- Z signal via $pp \rightarrow H \rightarrow AZ \rightarrow Z + \chi\bar{\chi}$ is a universal prediction in all DM pseudoscalar mediator models, while other signatures such as mono-Higgs are model dependent. Given that a sizeable $H^\pm \rightarrow AW$ rate is also a generic feature of DM pseudoscalar models if $M_{H^\pm} > M_A + M_W$, channels like $tW + E_T^{\text{miss}}$ [26] should also provide relevant constraints on the DM model introduced in [78].

Inert doublet model

In the scenarios discussed so far the DM particle has always been a fermion. The so-called inert doublet model (IDM) [79–81] is an intriguing DM model based on a 2HDM sector that can provide DM in the form of the spin-0 resonances H, A . A Z_2 symmetry renders the DM candidate stable and also implies that the bosonic states that originate from the second (dark) Higgs doublet can only be pair-produced. Since the dark scalars do not couple to the SM fermions, H, A, H^\pm production arises in the IDM dominantly from Drell-Yan processes. The IDM offers a rich spectrum of LHC E_T^{miss} signatures that ranges from mono-jet, mono- Z , mono- W , mono-Higgs to VBF + E_T^{miss} [82–92]. While the prospects to probe the IDM parameter space via the mono-jet channel seem to be limited [91], LHC searches for multiple leptons [82–85, 88, 89], multiple jets [87, 92] or a combination thereof [89] are expected to allow to test the IDM in limits that are not accessible by direct detection of DM or measurements of the invisible decay width of the SM Higgs. Furthermore, in scenarios in which the mass of DM is almost degenerate with M_{H^\pm} , searches for disappearing charged tracks provide a rather unique handle on the IDM high-mass regime [91]. Notice that while the IDM can lead to the same E_T^{miss} signals than the 2HDM+a model, the resulting kinematic distributions will in general not be the same, due to the different production mechanisms and decay topologies in the two models. Selection cuts that are optimised for a 2HDM+a interpretation of a given mono- X search will thus often not be ideal in the IDM context. Dedicated ATLAS and CMS analyses of the mono- X signatures in the IDM do unfortunately not exist at the moment. Such studies would however be highly desirable.

2HDM with an extra scalar mediator and scalar DM

The DM scenario proposed in [93] contains like the 2HDM+s model an extra scalar singlet, which however does not couple to a fermionic DM current $\bar{\chi}\chi$ but to the scalar operator χ^2 . The latter work focuses on the parameter space of the model where the mediator s is dominantly produced via either $pp \rightarrow H + j \rightarrow 2s + j \rightarrow j + 4\chi$ or $pp \rightarrow H \rightarrow sh \rightarrow h + 2\chi$. The resulting mono-jet and mono-Higgs cross sections however turn out to be safely below the existing experimental limits. In case the mass hierarchy $M_A > M_H + M_Z$ is realised,

the channel $pp \rightarrow A \rightarrow HZ$ is also interesting, since it either leads to a mono- Z or a $Zh + E_T^{\text{miss}}$ signature, depending on whether $H \rightarrow 2s \rightarrow 4\chi$ or $H \rightarrow hs \rightarrow h\chi^2$ is the leading decay. We add that an effective version of the model brought forward in [93] has already been constrained by ATLAS [94] using the mono-Higgs channel.

6 Model kinematics and mapping to existing models

The signature and kinematic distributions of the 2HDM+a model at colliders are driven by the values assigned to the parameters described in the previous chapter. The model parameters can affect the total signal cross-section, the kinematic distributions, or both. In order to obtain a representative grid of benchmark points for collider searches and reduce this multi-dimensional parameter space, we scan ranges of the possible values of these parameters and observe the impact on the kinematic distributions for representative collider searches.

In this chapter, we will outline the existing experimental searches that can be used to search for this model, and present the distributions of the kinematic variables for each of the searches as a function of the free parameters of the model. We note that in the following we have chosen to fix the DM coupling y_χ to unity, and $\lambda_{P1} = \lambda_{P2} = \lambda_P = 3$ as explained in ??.

6.1 Description of experimental searches

6.1.1 Signatures including a Higgs boson

Events with a 125 GeV Higgs boson, recently discovered with ATLAS and CMS [95, 96], and E_T^{miss} can indicate the production of Dark Matter candidates that recoil against the Higgs boson [97, 98]. The initial-state radiation (ISR) production of a Higgs boson is suppressed by the small Yukawa couplings of the Higgs boson to light quarks. Thus $h + E_T^{\text{miss}}$ searches such as [94, 99] directly probe potential new interactions of the Higgs and Dark Matter, as predicted by the 2HDM+a model [25, 33] due to the $a - A - h$ vertex.

$h(bb) + E_T^{\text{miss}}$ signature For the case where the Higgs boson decays into two b -quarks, such as studied in [99], the signal kinematics are studied at parton level. This allows a straightforward comparison to the model-independent results in [99], as described in subsection 8.1, and fast iteration over different model scenarios.

6.1.2 Signatures including a Z boson

Events with a Z boson and E_T^{miss} may signal the presence of invisible particles recoiling against the Z boson [100, 101]. LHC searches (e.g. [102, 103] for the most recent ones) have focused on invisible decays of the SM-like Higgs bosons or on topologies where the Z boson is produced as ISR from a quark. The ISR-based topologies generically favor radiation of a gluon or photon rather than a massive gauge boson, thus limiting the discovery sensitivity of a Z-based approach compared to monojet and mono-photon searches. In contrast, the model studied in this document generates the mono-Z signature dominantly via the all-bosonic H-a-Z vertex, which can lead to enhancements in the mono-Z sensitivity compared to jet and photon signatures.

Mono-Z (leptonic) signature Three consecutive stages of event selection are considered in the case the Z decays leptonically:

- Inclusive: Lepton p_T and η requirements corresponding to the typical experimental trigger acceptance are applied.
- Preselection: A dilepton candidate with an invariant mass in a window around the Z mass is required, and a minimum transverse momentum of the $\chi\bar{\chi}$ system is required.
- Final selection: Requirements on the main discriminating variables used in the relevant analyses are added: The angular separation in the transverse plane between the $\chi\bar{\chi}$ and $l^+ l^-$ systems $\Delta\Phi(l\bar{l}, E_T^{\text{miss}})$, the relative transverse momentum difference between them $|p_{T,l} - E_T^{\text{miss}}|/p_{T,l}$ and the angular separation between the leptons $\Delta R(l\bar{l})$. Additionally, the E_T^{miss} requirement is tightened.

The exact event selection criteria are listed in the appendix, in [Table 1](#). The results in this and in the following section are at particle level.

Mono-Z (hadronic) signature The hadronic signature in $Z+E_T^{\text{miss}}$ events ($Z \rightarrow q\bar{q}$ decays in association with large missing transverse momentum) is complementary to the leptonic signature. Hadronic decays are more frequent than leptonic decays, but suffer from larger backgrounds. For these reasons, the Z (hadronic) + E_T^{miss} search is favored if the model include higher mass scalar and pseudoscalar bosons.

The event selection in this case changes depending on the production transverse momentum of the Z-boson, as in the case of the exchange of a high-mass CP-even H boson. If the Z-boson is boosted, then its hadronic decay products could be merged into a single jet, and the Z to QCD background discrimination can be improved by exploiting the presence of substructure within a single, large-radius jet (denoted by J). The *boosted* search is performed in addition to the *resolved* search, where the Z decay products are reconstructed as two separate small-radius jets (denoted by j).

For mono- $Z(\rightarrow q\bar{q})$ events intermediated by the exchange of a high-mass CP-even H boson, the Z-boson will be produced with a large transverse momentum and the hadronic decay products of such Z-boson could be merged into a single jet. Such “boosted” event topology is investigated by exploiting the reconstruction technique with a large-radius jet (denoted by J), in addition to more conventional “resolved” event topology where the Z decay products are reconstructed as two separate small-radius jets (denoted by j). The jet reconstruction and the following analysis are all performed at particle level after showering and hadronization implemented in Pythia 8.212 described above.

Two consecutive stages of event selection are considered for the boosted and resolved event topologies:

- Inclusive: minimal kinematic requirements are applied to a pair of small-radius jets (a single large-radius jet) for the resolved (boosted) event topology. These selection criteria are applied separately, i.e, not sequentially.

- Final selection: selection criteria are applied to the a number of variables. The invariant mass of the pair of small-radius jets or the single large-radius jet is required to be within a window around the Z mass. In addition, selection is applied to the azimuthal angular difference between the $\chi\bar{\chi}$ and the hadronic Z -boson system, $\Delta\Phi(jj \text{ or } J, E_T^{\text{miss}})$, and the magnitude of E_T^{miss} . These final selection cuts are applied sequentially to mimic a realistic analysis; in this study the boosted selection cuts are applied first and then the resolved selection cuts are applied to those events that fail the boosted ones.

The exact event selection criteria are listed in the appendix, in [Table 2](#). The results in this and in the following section are at particle level.

6.1.3 Signatures including heavy flavor quarks

Heavy flavor final state can have sizable contributions to the production of the CP-even and CP-odd scalar mass eigenstates, due to the Yukawa structure of the couplings in the SM sector.

6.2 Kinematic distributions justifying the choice of parameter scan

6.2.1 Masses of the A , H , and a bosons (M_A , M_H , and M_a)

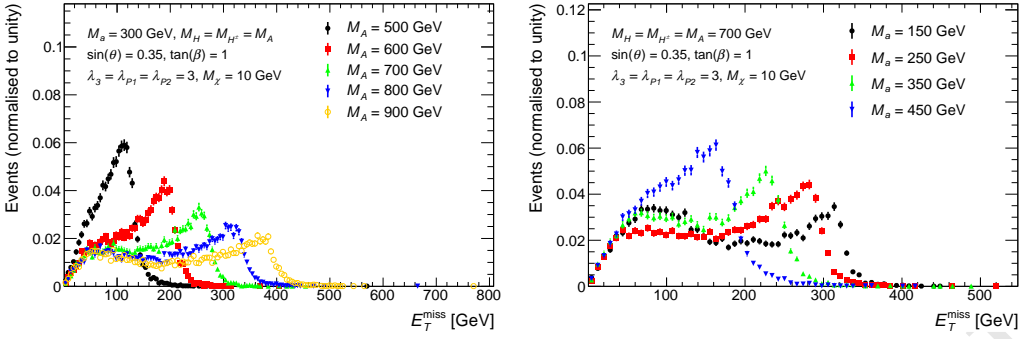
The **masses of the mediators M_A , M_H , and M_a of the pseudoscalars A and a and the scalar H** , which are the mediators of the resonant mono- h and mono- Z processes, affect the shape of the E_T^{miss} distribution of these processes. In the mono- Z and mono- H channels, the resonant production occurs through the $2 \rightarrow 1 \rightarrow 2$ processes $gg \rightarrow A \rightarrow ah$ and $gg \rightarrow H \rightarrow aZ$, respectively, with the light pseudoscalar decaying invisibly as $a \rightarrow \chi\chi$. In this case, the $A/H \rightarrow ah$ process produces a resonance in the invariant mass distribution of the final state system with a width determined by the widths of a , A/H , and of the SM bosons. This results in a peak in the transverse momentum distribution of the DM system, reconstructed as E_T^{miss} in the detector.

The location of this Jacobian peak can be calculated analytically starting from the masses of the particles involved in the decay [\[25\]](#):

$$E_T^{\text{miss},\max} \approx \frac{\sqrt{(M_{A/H}^2 - M_a^2 - M_{h/Z}^2)^2 - 4M_a^2M_{h/Z}^2}}{2M_{A/H}}. \quad (6.1)$$

Thus, increasing M_A results in a Jacobian peak at higher E_T^{miss} , as shown in [Figure 6a](#), [Figure 7](#) and [Figure 46](#). Conversely, models with higher M_a have a Jacobian peak at lower E_T^{miss} , as indicated in [Figure 6b](#) and [Figure 47](#). For $M_{A/H} \approx M_a + m_{Z/h}$, both the a and Z/h bosons are produced approximately at rest, leading to an event population with overall low boost. These qualitative trends are consistent with the distributions of the other main selection variables as shown in the appendix ([Appendix B](#)).

A potentially large fraction of the mono- h signal events is also produced in non-resonant $2 \rightarrow 3$ processes $gg \rightarrow h\chi\chi$, as in [??](#), leading to a broader distribution of the



(a) E_T^{miss} distribution for points with different M_A and fixed $M_a = 300$ GeV. (b) E_T^{miss} distribution for points with different M_a and fixed $M_A = 700$ GeV.

Figure 6: Parton-level E_T^{miss} distribution of mono-Higgs events for different M_a and M_A , with $M_H = M_{H^\pm} = M_A$, $\sin \theta = 0.35$, $\tan \beta = 1$, $M_\chi = 10$ GeV and $\lambda_{P1} = \lambda_{P2} = \lambda_3 = 3$

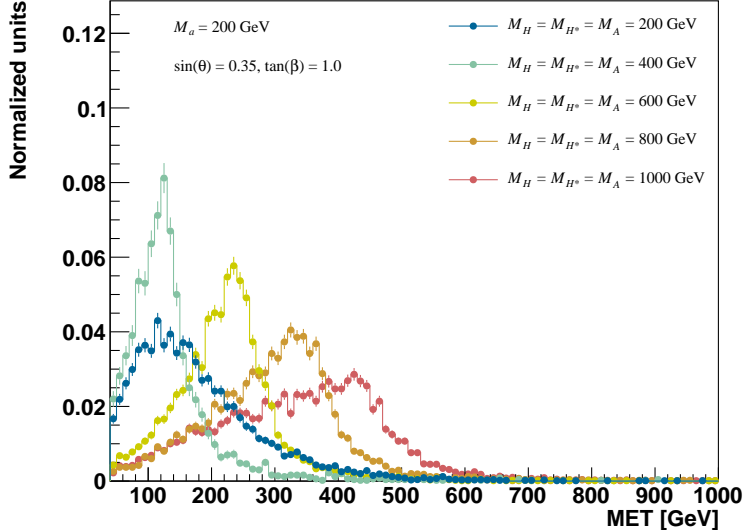


Figure 7: The E_T^{miss} distribution in signatures including a Z boson after preselection in the leptonic channel, with varying M_H values for fixed $M_a = 200$ GeV and $M_A = M_{H^\pm} = M_H$.

invariant mass of the decay products. Consequently, this results in a broader and softer E_T^{miss} distribution that is distinct from the Jacobian peak discussed above, and contributes to the off-peak features of [Figure 6b](#) and [Figure 6a](#).

The masses M_a and M_A influence the kinematics in the $t\bar{t} + E_T^{\text{miss}}$ signature as well. As shown in [Figure 10](#), the E_T^{miss} , and leading and trailing top quark p_T distributions broaden with increasing M_a . Similarly, for values of $M_A < M_a$, as M_A increases, the kinematic distributions mentioned above also broaden, as shown in [Figure 11](#).

Since the shape of the E_T^{miss} distribution affects the design of experimental searches,

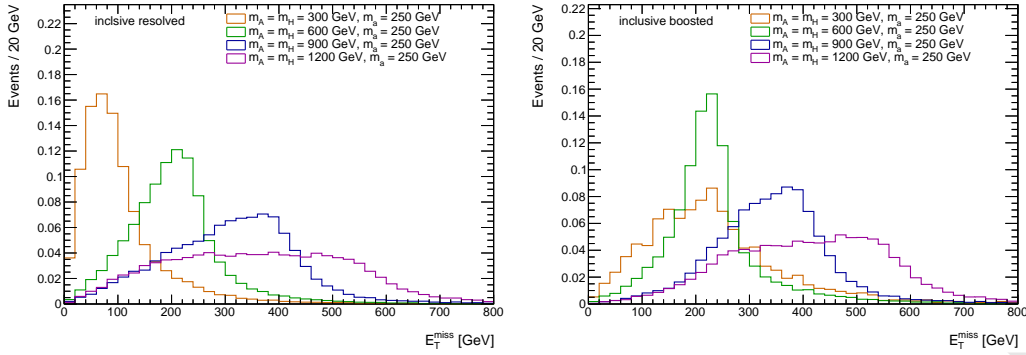


Figure 8: E_T^{miss} distributions in the resolved (left) and boosted (right) hadronic Z search, after applying the inclusive selection. The signal masses are chosen to be $M_H = 300, 600, 900$ and 1200 GeV with the fixed $M_a = 250$ GeV and $M_A = M_{H^\pm} = M_H$.

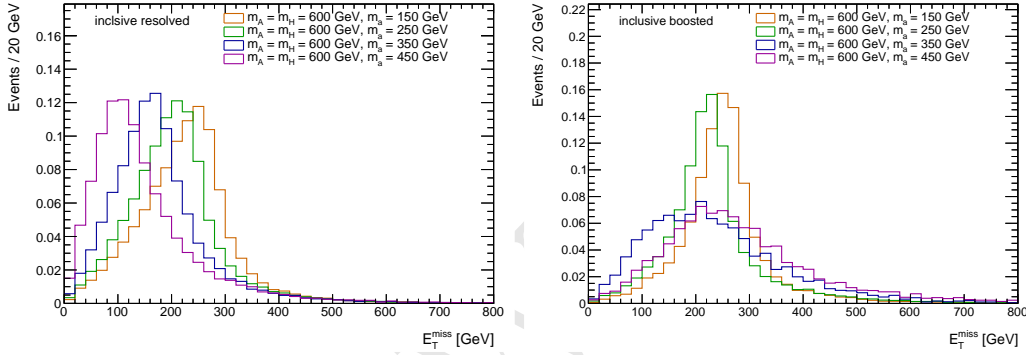


Figure 9: E_T^{miss} distributions in the resolved (left) and boosted (right) hadronic Z search, after applying the inclusive selection. The signal masses are chosen to be $M_a = 150, 250, 350$ and 450 GeV with the fixed $M_H = 600$ GeV ($= M_A = M_{H^\pm}$).

and to a large extent their sensitivity, *it is desirable to scan the M_A and M_a parameter space.*

In designing a search for evidence of this particular model, it may be useful to consider not only the E_T^{miss} , but also the transverse mass M_T ¹ variable. The distributions of both variables after final selection are shown in Figure 12 for the $Z+E_T^{\text{miss}}$ searches. Both distributions show Jacobian peak structures due to dominant effect of the diagram with resonant H exchange. In the case of $M_a < M_H$, the peak structure is more defined in the M_T distribution than in the E_T^{miss} , thus helping to distinguish a possible signal from background. Where the resonant diagram does not contribute, i.e. for $M_a \approx M_H$ or $M_a > M_H$, the M_T distribution does not show a significantly different structure from the E_T^{miss} distribution and will not provide an improved sensitivity.

For mono- h , the **mass of the heavy neutral scalar Higgs boson H** has an indirect effect on the rate and kinematics of the signal. This is caused by the dependence of the

¹The massless definition is used here: $M_T = \sqrt{2E_T^{\text{miss}} p_{T,Z} (1 - \cos(\Delta\phi))}$

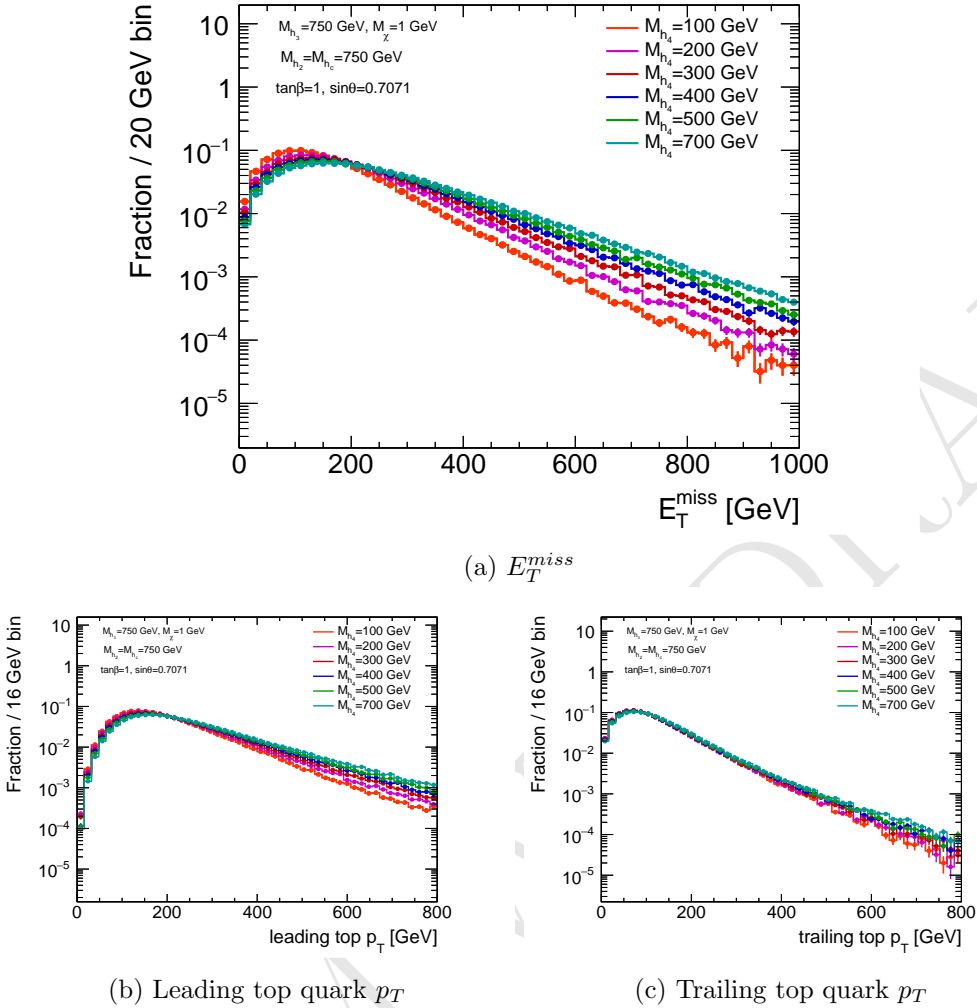


Figure 10: The E_T^{miss} , leading and trailing top p_T distributions for inclusive $t\bar{t} + \chi\bar{\chi}$ production for various values of M_a , with $M_A = 750$ GeV, $M_H = M_{H^\pm} = 750$ GeV, $\tan\beta = 1$, and $\sin\theta = 0.7071$.

coupling strength of the $a - A - h$ vertex, and thus decay width of the pseudoscalar A , on M_H [25]. Therefore, a change of M_H can strongly affect the relative contribution of resonant versus non-resonant signal processes, as illustrated in Figure 13. For mono- Z , there is no corresponding effect of M_A on the resonant and non-resonant signal yields, since the $a - H - h$ vertex has a simpler structure with no M_A dependence.

The choice $M_H = M_A$ results in a detectable total cross section and a dominant contribution of the resonant mono- h signal process for many signal points. This choice allows us to test diverse E_T^{miss} distributions and results in about equal contributions to the sensitivity through the $Z + E_T^{miss}$ and $h + E_T^{miss}$ signatures, highlighting their complementarity. For this reason *the choice $M_H = M_A$ is adopted* for all scans.

The mass of the neutral scalar H^\pm does not affect the model kinematics, as shown in

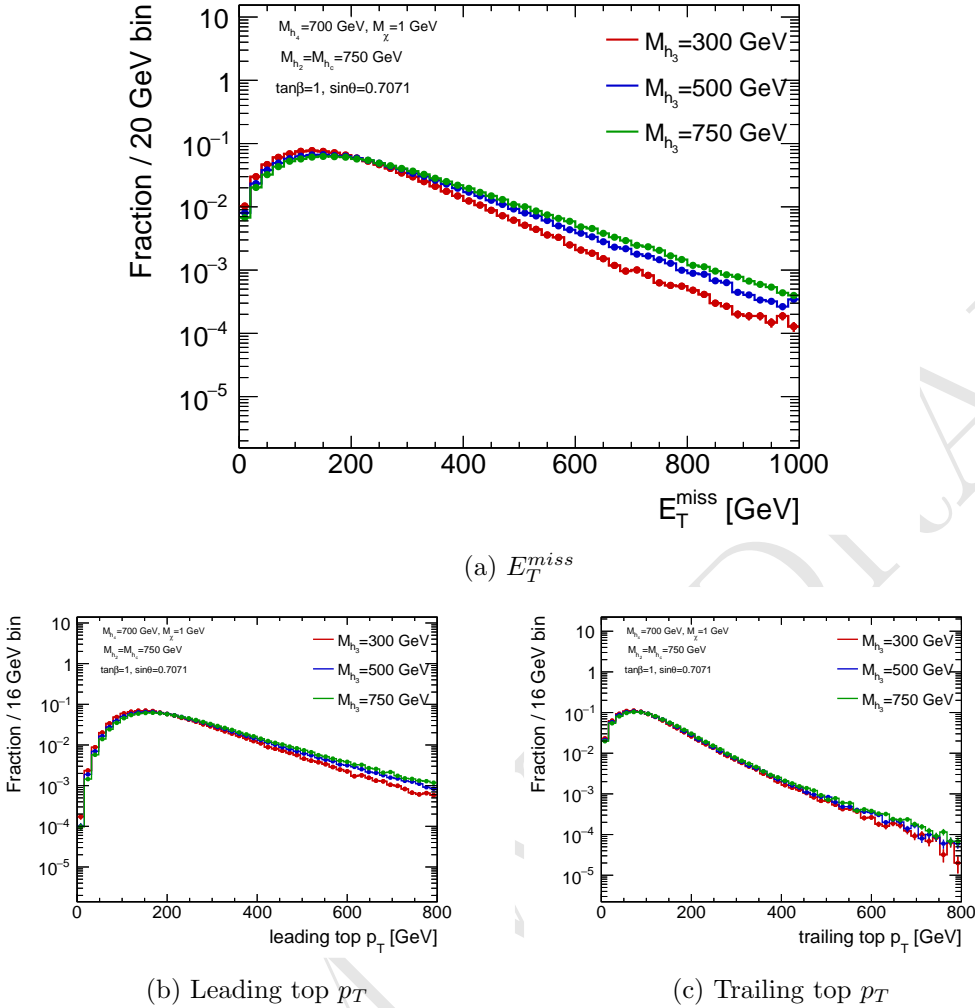


Figure 11: The E_T^{miss} , leading and trailing top p_T distributions for inclusive $t\bar{t} + \chi\bar{\chi}$ production for various values of M_A , with $M_A = 700$ GeV, $M_H = M_{H^\pm} = 750$ GeV, $\tan\beta = 1$, and $\sin\theta = 0.7071$, before any analysis selection.

Appendix ???. Models with $M_{H^\pm} \neq M_H$ are moreover strongly constrained by electroweak precision measurements of the ρ parameter [25]. Therefore, for simplicity, the *neutral scalar* H^\pm is assumed to be mass-degenerate to H .

6.2.2 Mixing angle between the two pseudoscalars A and a ($\sin\theta$)

The sine of the mixing angle between the two pseudoscalars A and a , $\sin\theta$, affects not only the cross section, but also the shape of the E_T^{miss} distribution in searches including a Higgs boson, as shown in Figure 17a. For the resonant diagram $gg \rightarrow A \rightarrow ah \rightarrow \chi\bar{\chi}h$, the product of cross section times branching ratios $\mathcal{B}(A \rightarrow ah)\mathcal{B}(a \rightarrow \chi\bar{\chi})$ scales with $\sin^2\theta \cos^6\theta$, while for the diagram $gg \rightarrow a \rightarrow A^*h \rightarrow \chi\bar{\chi}h$, the product of cross section times branching ratios $\mathcal{B}(a \rightarrow Ah)\mathcal{B}(A \rightarrow \chi\bar{\chi})$ scales with $\sin^6\theta \cos^2\theta$. This is shown in

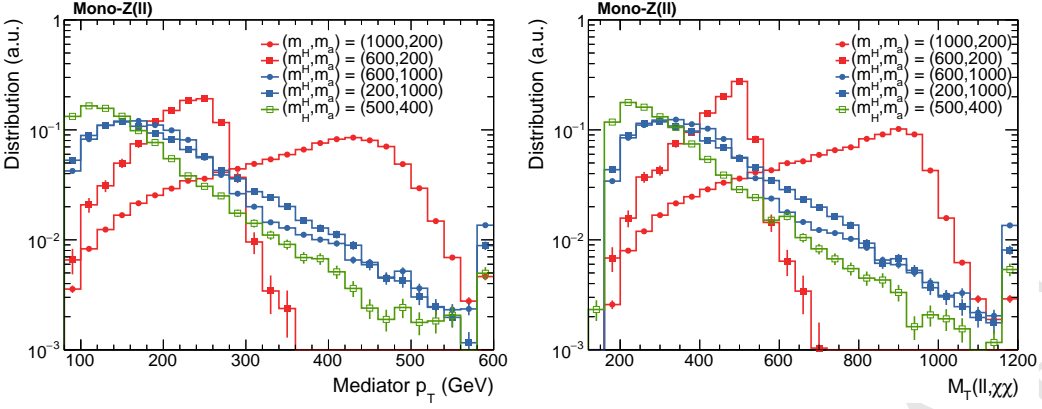


Figure 12: E_T^{miss} and M_T distributions after the full selection of $Z(\text{lep})+E_T^{\text{miss}}$ search. Both distributions show a peaked structure around M_H in the $M_H > M_a$ regime, reflecting the resonant production of H with a subsequent decay $H \rightarrow aZ$.

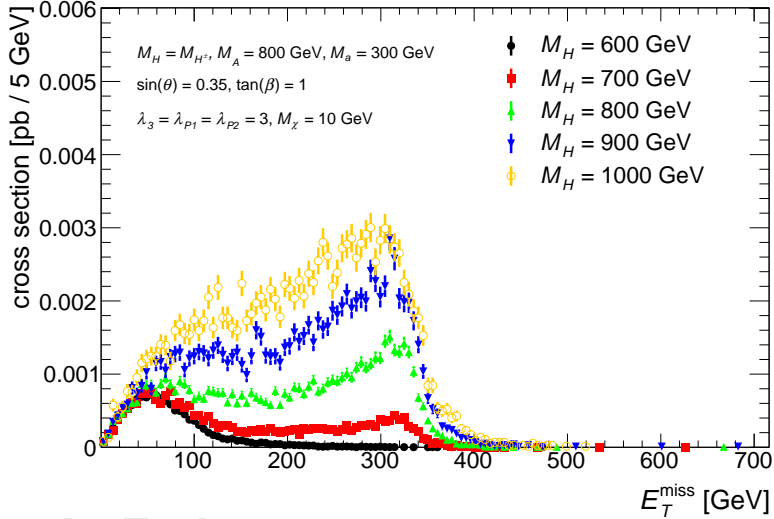


Figure 13: The E_T^{miss} distribution, accounting for the production cross section, of $h(bb) + E_T^{\text{miss}}$ signal events for five representative choices of $M_H = M_{H^\pm}$.

Figure 14: E_T^{miss} distribution in $h(bb) + E_T^{\text{miss}}$ and $Z+E_T^{\text{miss}}$ events for different M_H

Appendix ???. Therefore, at small $\sin\theta$, the resonant diagram $A \rightarrow ah$ is the dominant production mode and the E_T^{miss} distribution has a Jacobian peak following Equation 6.1; while at large $\sin\theta$, the $a \rightarrow A^*h$ diagram starts to dominate and produces a second peak at a lower E_T^{miss} value.

Scans of the $\sin\theta$ parameter show they have minimal effect on the kinematic distributions for searches with a Z boson (Figure 17b).

In the $t\bar{t} + E_T^{\text{miss}}$ signature, the A (h_3 in the figure) and a (h_4 in the figure) mass peaks are quite narrow for values where $\sin\theta$ approaches 1, and $a \rightarrow \chi\bar{\chi}$ is the dominant $\chi\bar{\chi}$ production mode, as shown in Figure 15. However, no significant kinematic dependence on

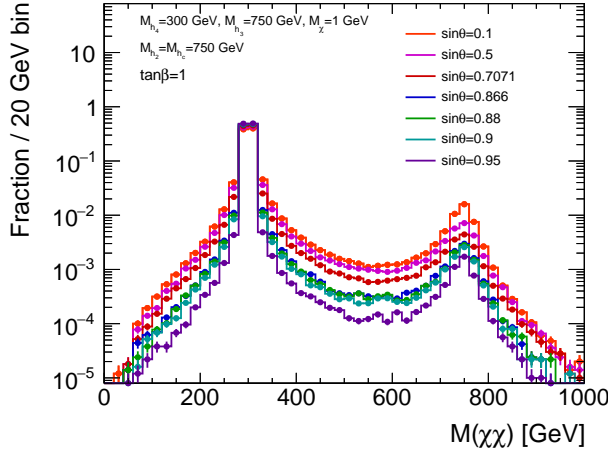


Figure 15: The mass distribution of the $\chi\bar{\chi}$ system for various values of $\sin \theta$, with $M_a = 300$ GeV, $M_A = 750$ GeV, $M_H = M_{H^\pm} = 750$ GeV, and $\tan \beta = 1$.

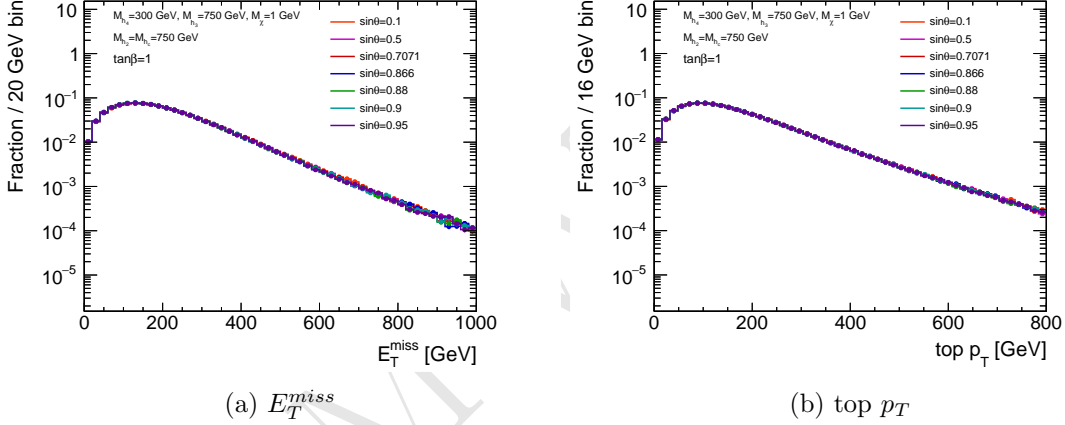
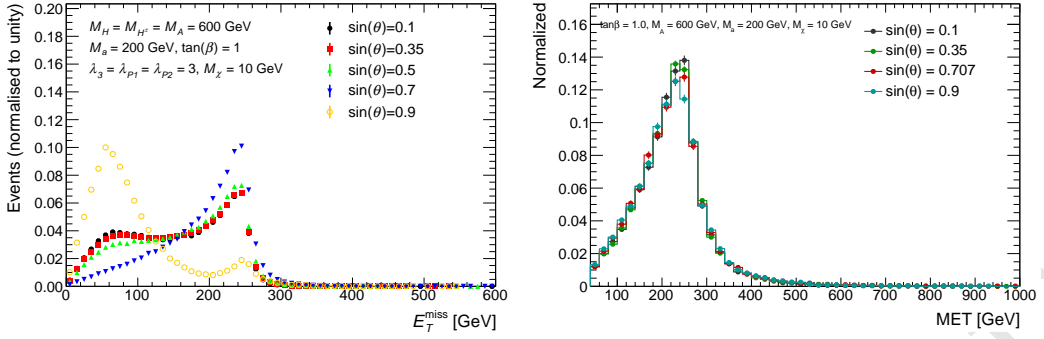


Figure 16: The E_T^{miss} and top p_T distribution for inclusive $t\bar{t} + \chi\bar{\chi}$ production for various values of $\sin \theta$, with $M_a = 300$ GeV, $M_A = 750$ GeV, $M_H = M_{H^\pm} = 750$ GeV, and $\tan \beta = 1$.

$\sin \theta$ is observed in the E_T^{miss} and top quark p_T as shown in Figure 16 before any analysis cuts are applied.

6.2.3 Ratio of the doublet vacuum expectation values ($\tan \beta$)

For mono- h signals, the shape of the E_T^{miss} distribution also has a non-trivial dependence on $\tan \beta$, as can be seen in Figure 18. As discussed in the sensitivity study later, at small $\tan \beta$, the Yukawa coupling to top quark is large and the signal production mode is dominated by the non-resonant 3-body process $gg \rightarrow h\chi\bar{\chi}$, which gives a broad and soft E_T^{miss} spectrum. As $\tan \beta$ increases, Γ_A decreases. With a more narrow A , the relative contribution of resonant A decays increases, and the Jacobian peak grows more pronounced, eventually dominating the E_T^{miss} spectrum. When the on-shell $A \rightarrow ah$ decay is kinemati-



(a) E_T^{miss} distribution for five representative models with different $\sin\theta$ and fixed scans of $\sin\theta$ for fixed $M_A = M_H = M_{H^\pm} = M_A = M_H = M_{H^\pm} = 600$ GeV, $M_a = 600$ GeV and $M_a = 200$ GeV. 200 GeV.

(b) E_T^{miss} distribution after preselection for fixed $\tan\beta = 1.0$, $M_A = 600$ GeV, $M_a = 200$ GeV, $M_h = 200$ GeV, $M_\chi = 10$ GeV.

Figure 17: E_T^{miss} distributions in $h(bb) + E_T^{\text{miss}}$ and $Z(\text{lep}) + E_T^{\text{miss}}$ events for different $\sin\theta$. In both cases, $\tan\beta = 1$ and $M_\chi = 10$ GeV.

cally forbidden, i.e. when $M_A < M_a + M_h$, the shapes of E_T^{miss} distributions become similar and the dependence on $\tan\beta$ almost disappears. For small values of $\tan\beta$ there is a slight softening and broadening of the E_T^{miss} distribution caused by the increased contribution from non-resonant $Z + a$ production in $Z + E_T^{\text{miss}}$ searches.

In the $t\bar{t} + E_T^{\text{miss}}$ signature, and in the limit of small $\tan\beta$ values, the couplings of A (h_3 in the figure) and a (h_4 in the figure) to down-type quarks are heavily suppressed regardless of the Yukawa assignment. At LO, $t\bar{t} + \chi\bar{\chi}$ associated production is mediated through either CP-odd weak eigenstate, A or a , though it is shown in Figure 20 that $a \rightarrow \chi\bar{\chi}$ is the dominant production mode. Although the relative mediator contribution is dependent on $\tan\beta$, observables such as E_T^{miss} and top quark p_T only have a moderate kinematic dependence on $\tan\beta$ as demonstrated in Figure 21 before any analysis cuts. Other variables, such as the transverse mass M_T , are more affected by the contribution of the high mass mediator, as shown in Figure 21 after kinematic cuts.

The production cross-section for a, h, H and A are driven by top-quark loops in the gluon-fusion channel [27], as shown e.g. [as shown in the Feynman diagram], and enhanced for small values of $\tan\beta$. For this reason, and to highlight the complementarity of the $H + E_T^{\text{miss}}$ and $Z + E_T^{\text{miss}}$ signatures, the main focus of the parameter scans should be on the small $\tan\beta$ region. Setting $\tan\beta$ to unity leads to a sufficiently large on-shell contribution even at low masses. This in turn increases the number of events at higher E_T^{miss} , so that the $H + E_T^{\text{miss}}$ search can have a comparable sensitivity to the $Z + E_T^{\text{miss}}$ search even though it requires higher E_T^{miss} . Moreover, since the cross-section times branching ratio for the $b\bar{b} + E_T^{\text{miss}}$ signature is enhanced at high values of $\tan\beta$ (see Eq. 3.2 and 3.3 in Ref. [25]) it is desirable to perform a coarse scan in $\tan\beta$ as well.

It is interesting to note however that the relative total width for the heavy scalar H becomes unphysically large at high $\tan\beta$ when all scalars have the same mass, due to the very large $H \rightarrow aa$ rate. This can be cured by tuning the mass of the heavy scalar so that

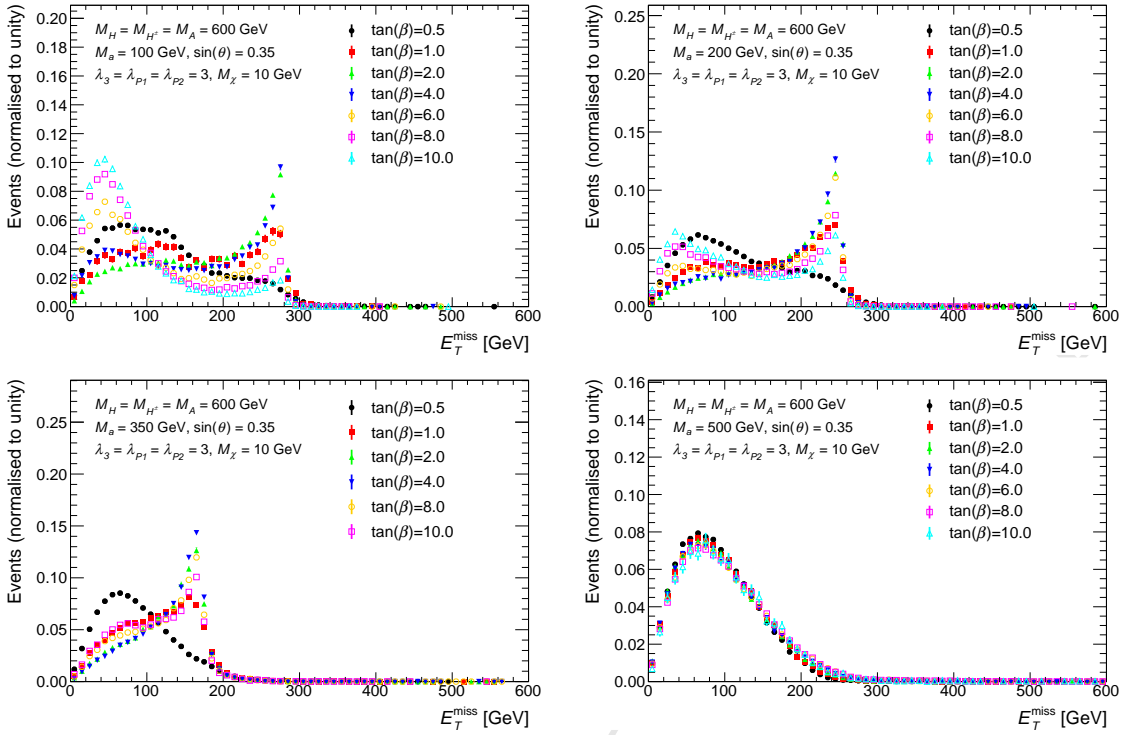


Figure 18: Missing transverse momentum distribution of $h \rightarrow bb + E_T^{\text{miss}}$ signal events at parton level with different $\tan\beta$ and fixed $M_A = M_H = M_{H^\pm} = 600 \text{ GeV}$, $M_\chi = 10 \text{ GeV}$, $\sin\theta = 0.35$, and $\lambda_{P1} = \lambda_{P2} = \lambda_3 = 3$. The values of M_a are set to 100, 200, 350, and 500 GeV, respectively. The shapes of the E_T^{miss} distributions for different $\tan\beta$ are similar when $M_A < M_h + M_a$. Note, in these figures, both the contributions of gg and $b\bar{b}$ initiated processes are included and a combined histogram is produced according to their corresponding cross sections.

the coupling between the heavy scalar and the light pseudoscalar g_{Haa} becomes small for this scan only, therefore suppressing the $H \rightarrow aa$ rate that drives the width. An example of the heavy scalar width as a function of $\tan\beta$, with $M_H = M_A = 600 \text{ GeV}$, $M_{H^\pm} = 664 \text{ GeV}$, $\sin\theta = 0.35$, $M_\chi = 10 \text{ GeV}$ and $g_{DM} = 1$ is shown in Fig. 22.

Even though this choice of parameters for this scan introduces a specific tuning and therefore model-dependence, it can be justified by noting that the trilinear scalar couplings are very sensitive to changes in the model’s masses and couplings, and this in turn changes the decay partner of the heavy scalar and of the Higgs partners. Furthermore, the Higgs width does not influence the $b\bar{b} + E_T^{\text{miss}}$ signal directly. Nevertheless, if this is tuning is not performed, particular care has to be taken at high $\tan\beta$ values to obtain reasonable results outside the narrow-width approximation, both for the generation of the signal and for the interpretation of the results.

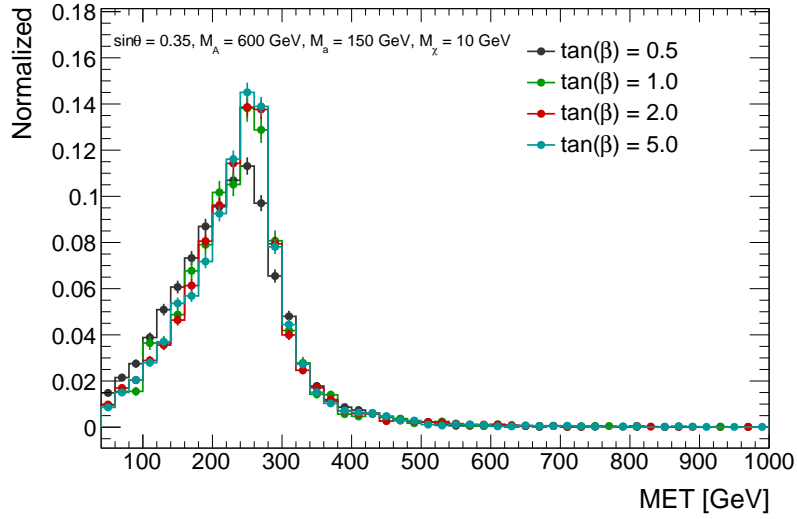


Figure 19: E_T^{miss} distribution after preselection for scans of $\tan \beta$ for fixed $M_A = 600$ GeV and $M_a = 150$ GeV. This parameter has little impact on the kinematic distributions, except for small values of $\tan \beta$ where there is a slight softening and broadening of the E_T^{miss} distribution caused by the increased contribution from the top box Feynman diagram.

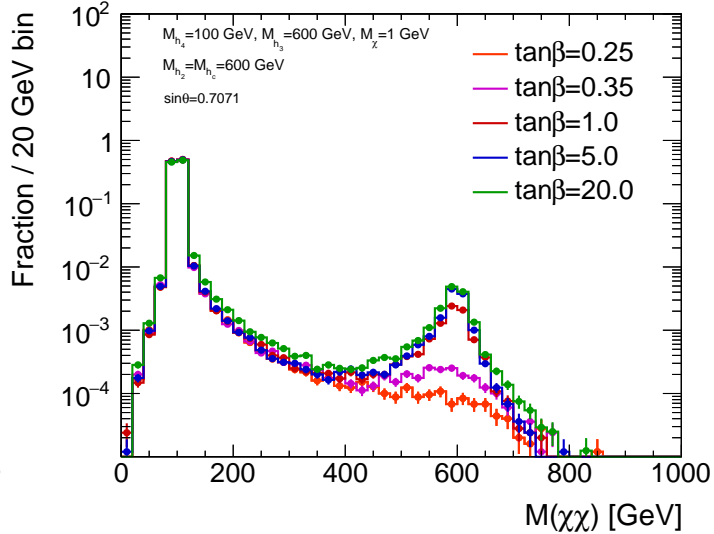


Figure 20: The mass distribution of the $\chi\bar{\chi}$ system for various values of $\tan \beta$, with $M_a = 100$ GeV, $M_A = 600$ GeV, $M_H = M_{H^\pm} = 600$ GeV, and $\sin \theta = 0.7071$.

6.2.4 Mass of DM fermion (M_χ)

The mass of the DM fermion M_χ can change the total cross section and shape of the E_T^{miss} distribution, depending on the mass hierarchy of the A, a, h, χ particles. This is demonstrated in Figure 24. Provided on-shell decays $a \rightarrow \chi\chi$ are possible, i.e., $M_\chi < M_a/2$, the exact value of M_χ has no effect on either kinematics or the total cross section. The

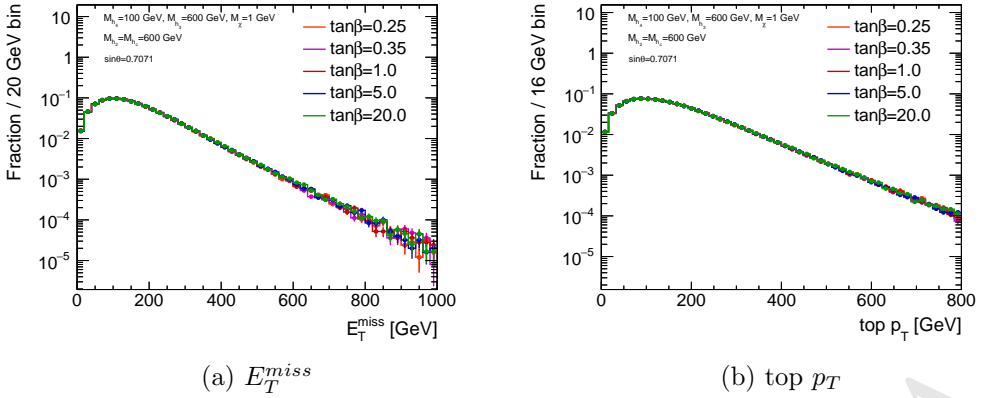


Figure 21: The E_T^{miss} and top p_T distribution for inclusive $t\bar{t} + \chi\bar{\chi}$ production for various values of $\tan\beta$, with $M_a = 100$ GeV, $M_A = 600$ GeV, $M_H = M_{H^\pm} = 600$ GeV, and $\sin\theta = 0.7071$.

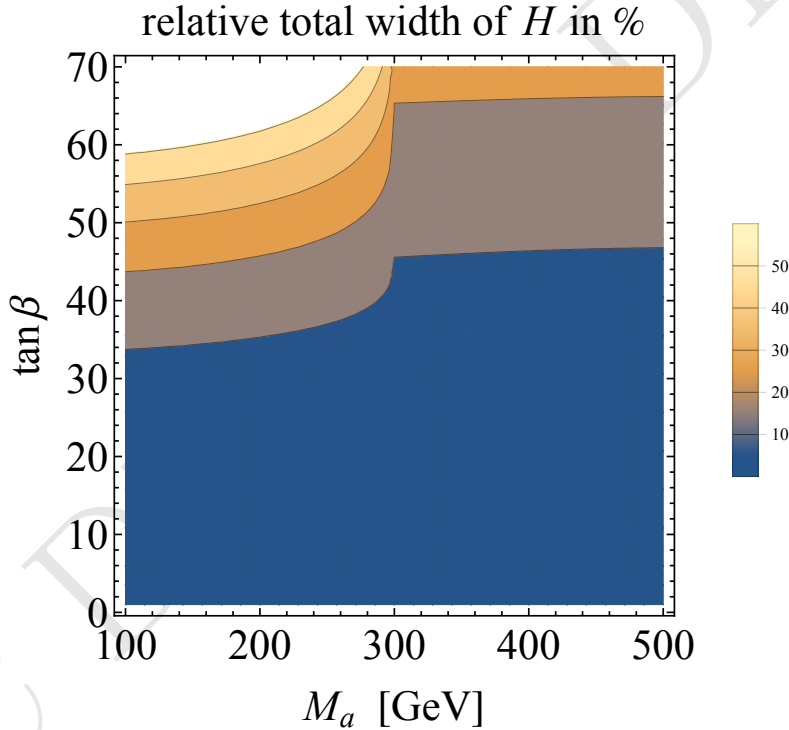


Figure 22: The width of the heavy scalar as a function of $\tan\beta$, with $M_H = M_A = 600$ GeV, $M_{H^\pm} = 664$ GeV, $\sin\theta = 0.35$, $M_\chi = 10$ GeV and $g_{DM} = 1$.

only exception is the case $M_a/2 > M_\chi > \frac{1}{2}(M_a - M_h)$. In this M_χ range, the non-resonant process $a \rightarrow hA^*(\chi\chi)$ is kinematically inaccessible. This reduces the overall cross section relative to the $M_\chi \leq \frac{1}{2}(M_a - M_h)$ case, and slightly changes the soft part of the total E_T^{miss} spectrum. However, since the contribution of the $a \rightarrow hA^*(\chi\chi)$ process is minor in any case, the differences are negligible.

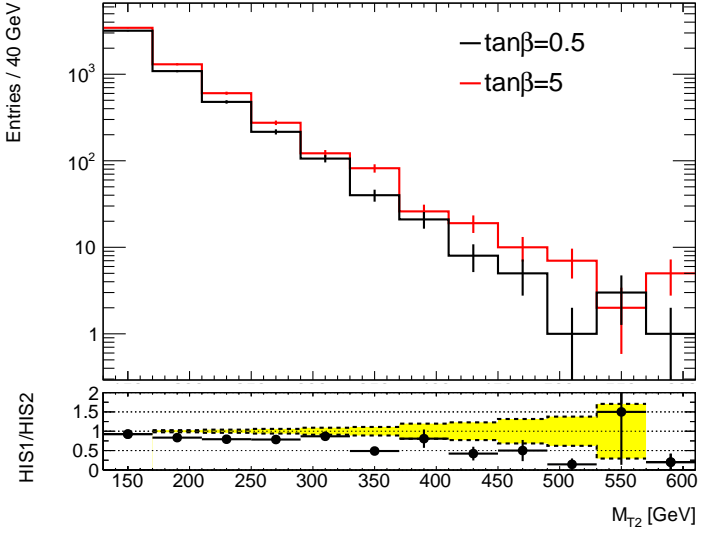


Figure 23: The M_T distribution in the $t\bar{t} + E_T^{\text{miss}}$ signature for different values of $\tan\beta$, after all selection cuts.

If the DM particle mass is exactly on threshold, i.e., $M_\chi = M_a/2$, the total cross section is resonantly enhanced. This resonant threshold enhancement drops rapidly towards both higher and lower M_χ . Furthermore, the shape of the E_T^{miss} distribution at threshold, where amplitudes involving $a \rightarrow \chi\chi$ decays make up a larger fraction of the signal, differs significantly from the one below threshold. Below threshold ($M_\chi > M_a/2$), the total cross section quickly drops by several orders of magnitude. In this regime, the shape of the E_T^{miss} distribution changes with M_χ continuously.

Similar effects are seen in Figure 25. In the $M_\chi < \frac{M_a}{2}$ region, M_χ has no effect on event yield or E_T^{miss} distribution, at $M_\chi = \frac{M_a}{2}$ a resonant enhancement to the cross section occurs, and in the off-shell region where $M_\chi > \frac{M_a}{2}$ cross section steeply drops. The E_T^{miss} shape remains the same up to, and even slightly above, $M_\chi = \frac{M_a}{2}$, but further off shell the E_T^{miss} distribution becomes increasingly disperse. For $M_\chi = 200$ GeV, DM can still decay on-shell through the A . For $M_\chi = 500$ GeV both pseudoscalars are off-shell leading to an event yield too low to fit on the figure on the left and a E_T^{miss} distribution without structure.

A value of $M_\chi = 10$ is chosen as the baseline for the following studies, as it produces a cross-section that is sufficiently large for this model to be detected with Run-2 LHC data and highlights the resonant features of the E_T^{miss} spectrum.

6.3 Comparison with existing pseudoscalar models and recasting of HF+ E_T^{miss} search results

To date, simplified models of DM [1, 104] that add a single scalar or pseudoscalar mediator and the DM particle to the SM are used as benchmarks for the Run II CMS and ATLAS HF+ E_T^{miss} searches. These are called **DMsimp** models in the following. The kine-

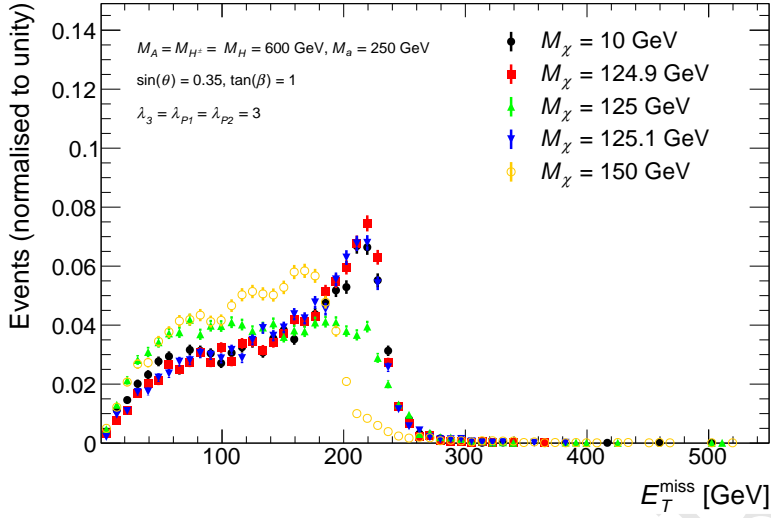


Figure 24: Missing transverse momentum distribution of $h(bb) + E_T^{\text{miss}}$ signal events at parton level for five representative models with different M_χ and fixed $M_A = M_H = M_{H^\pm} = 600$ GeV, $M_a = 250$ GeV, $\sin \theta = 0.35$, $\tan \beta = 1$ and $\lambda_{P1} = \lambda_{P2} = \lambda_3 = 3$. The shape of the E_T^{miss} distribution does not change for $M_\chi < M_a/2$, then changes significantly for $M_\chi \geq M_a/2$.

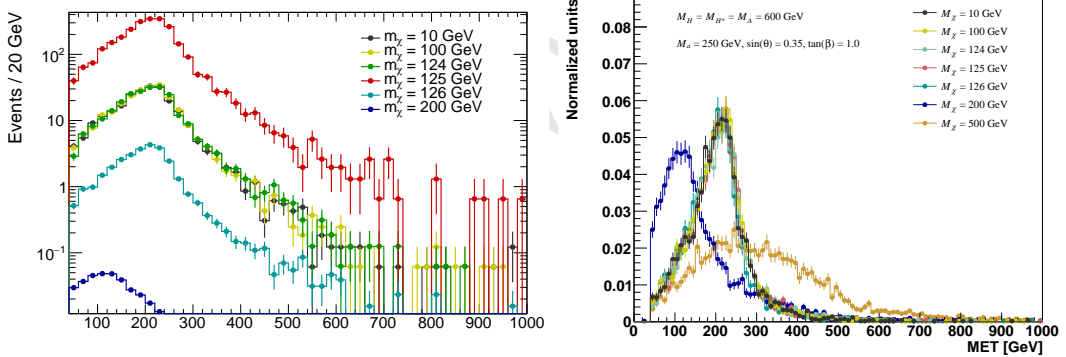


Figure 25: E_T^{miss} distributions following preselection in the $Z(\text{lep}) + E_T^{\text{miss}}$ search are shown (left) scaled to 40 fb^{-1} and (right) normalized to unity for different values of M_χ with fixed $M_A = 600$ GeV and $M_a = 250$ GeV.

matics and cross-section of the pseudoscalar `DMsimp` models can map directly onto those of the 2HDM+a model, when accounting for the contributions from the light and heavy pseudoscalar mediators.

The comparison of some of the relevant kinematic distributions between the pseudoscalar simplified model and the 2HDM+a model using two different values of M_a , is shown in Figure 26. In these figures, the parameters used are: $M_A = 600$ GeV, $M_H = M_{H^\pm} = 600$ GeV, $\sin \theta = 0.7071$, $\tan \beta = 1$, while M_a is either 100 or 600 GeV. The distributions for

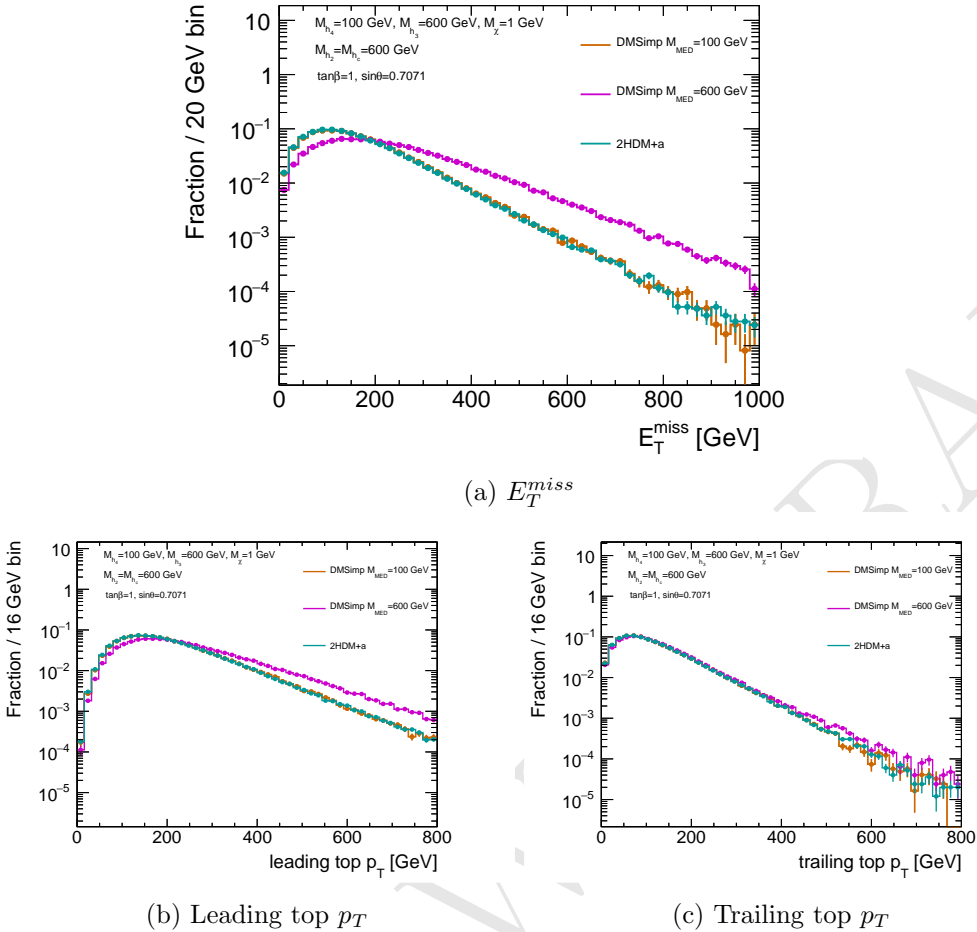


Figure 26: The E_T^{miss} , leading and trailing top p_T distributions for inclusive $t\bar{t} + \chi\bar{\chi}$ production for different values of M_a , with $M_A = M_H = M_{H^\pm} = 600$ GeV, $\tan\beta = 1$, $M_\chi = 1$ GeV and $\sin\theta = 0.7071$, compared to the DMsimp pseudoscalar model.

the two models agree when the mediator mass in the DMsimp model is set to M_a and the contribution from A decays is smaller since A is more massive than a .

The DMsimp model has only one mediator particle. Figure 27 shows that the 2HDM+a model can be represented as the sum of two contributions, one from the light pseudoscalar and the other one from the heavy pseudoscalar. This is because the HF+ E_T^{miss} signatures are dominantly produced in diagrams involving the invisible decays of the two CP-odd scalars. The 2HDM+a model is equivalent to the single pseudoscalar simplified model DMsimp when A is much heavier than a , and therefore the former does not contribute to the considered final state. However, when the two mediators are closer in mass, the $pp \rightarrow t\bar{t}A$ contribution becomes more relevant. This can be seen in Figure 28, where the two models are compared assuming $m(A) = 750$ GeV and two different values for $m(a)$. An excellent agreement is observed between DMsimp and 2HDM+a at parton-level variables sensitive to the helicity structure of the interaction between top and the mediator[105], if

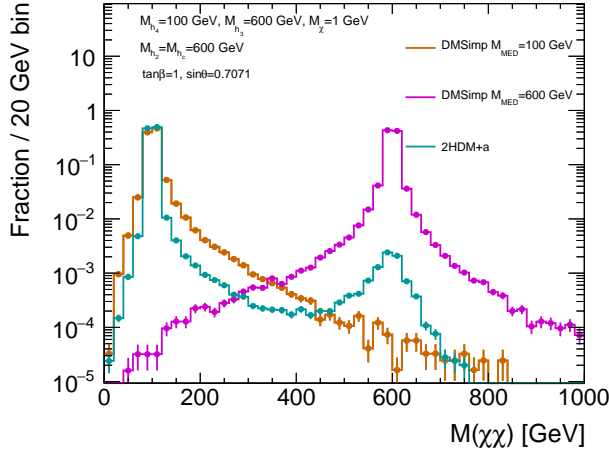


Figure 27: The mass distribution of the $\chi\bar{\chi}$ system for **DMSimp** pseudoscalar models with $M_a = 100$ GeV and $M_a = 600$ GeV, compared with 2HDM+a with $M_a = 100$ GeV, $M_A = 600$ GeV, $M_H = M_{H^\pm} = 600$ GeV, $\sin \theta = 0.7071$ and $\tan \beta = 1$. TODO: needs different markers.

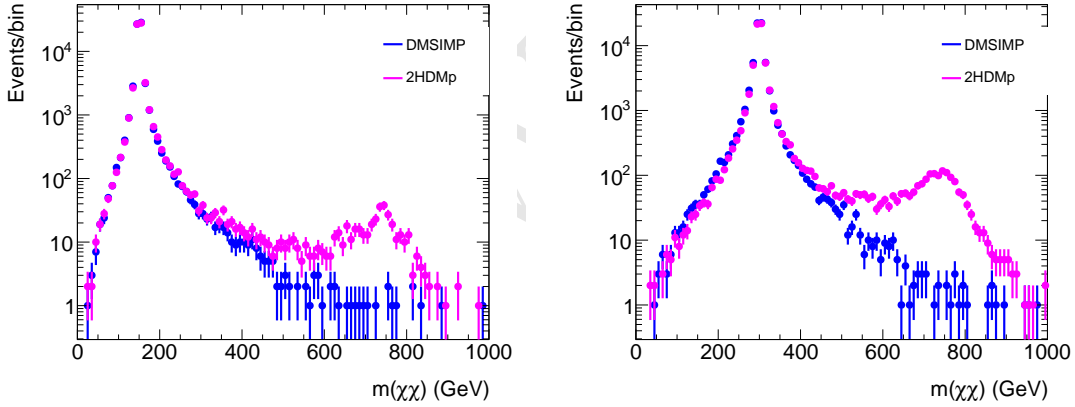


Figure 28: Comparison of $m(\chi\chi)$, the invariant mass of the two DM particles for the **DMSimp** (blue) and the **2HDMp** model (magenta) with $m(A) = M_{med} = 750$ GeV. The plot on the left uses $M_a = 150$ GeV, while the plot on the right uses $M_a = 300$ GeV.

the invariant mass of the two DM particles in the 2HDM is smaller than 200(300) GeV for $m(a) = 150(300)$ GeV respectively. This gives confidence that, once the contribution from A production is identified and separated, it is possible to fully map the $2HDM + a$ kinematics to the existing **DMSimp** model.

The mapping that can be used to reinterpret existing searches that use the **DMSimp** model is achieved by taking, for each set of the parameters, the average of the selection acceptances for $m(A)$ and $M(A)$ obtained from the **DMSimp** model, weighted by the respective

cross-section for A (σ_A) and a (σ_a) production:

$$Acc_{2HDM}(m(A), M(a)) = \frac{\sigma_a \times Acc_{DMSimp}(m(a)) + \sigma_A \times Acc_{DMSimp}(m(A))}{\sigma_a + \sigma_A} \quad (6.2)$$

The acceptance in this case is obtained as a parton-level implementation of the two-lepton analysis described in [arXiv:1710.11412]. The acceptance estimated in this way is shown as red triangles in Figure 29, and an excellent agreement can be seen with the acceptances evaluated directly on the 2HDM samples. Further validation was performed also on the acceptances calculated as a function of $\sin\theta$ and $\tan\beta$. Finally, the formula was successfully tested also with $|M_A - M_a| \sim 50$ GeV, where interference between the production of the two bosons is possible.

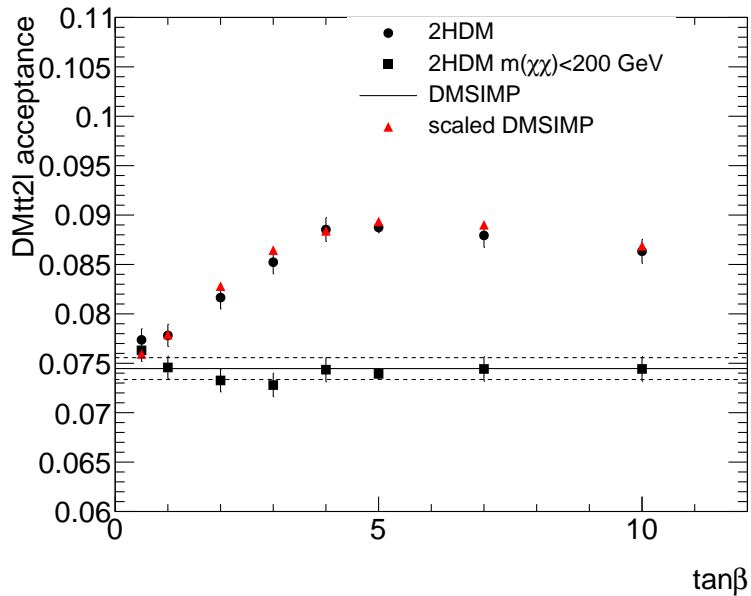


Figure 29: Acceptance of the two-lepton analysis as a function of $\tan\beta$ for the $2HDM_p$ model (round markers), for the $2HDM_p$ model considering only events with $m(\chi\chi) < 200$ GeV (square markers), and for the $DMSIMP$ model (full line) for a mediator mass of 150 GeV. The two dashed lines indicate the statistical error of the $DMSIMP$. The value of $m(A)$ is fixed at 600 GeV, and $\sin\theta = 0.35$. The acceptance calculated from the $DMSIMP$ acceptance rescaled following the prescription in Equation 6.2 (red triangles) is also shown.

7 Parameter grid

The studies in the previous section show that varying most of the model parameters lead to non-trivial modifications of the for the $H+E_T^{\text{miss}}$ and $Z+E_T^{\text{miss}}$ searches. We decide to investigate the model parameter space through two-dimensional and one-dimensional scans of five parameters: the light pseudoscalar mass (M_a), the heavy pseudoscalar mass (M_A)

that we set equal to the mass of the heavy and charged Higgs bosons ($M_A = M_H = M_{H^\pm}$), the mixing angle $\sin \theta$, the ratio of VEVs of the Higgs doublets $\tan \beta$ and the dark matter particle mass M_χ . The benchmark model points that have been agreed within the DMWG and are suggested here do not provide an exhaustive scan the entire parameter space of this model, but highlights many of the features that are unique of this model and showcases the complementarity of the various signatures.

Scan in the M_a , $M_A = M_H = M_{H^\pm}$ plane The main parameter grid proposed to investigate this model with LHC data spans combinations of the light pseudoscalar mass (M_a) and the heavy pseudoscalar mass (M_A) plane, fixing $M_A = M_H = M_{H^\pm}$. The mixing angle $\sin \theta$ is fixed to 0.35 (leading to asymmetric mixing between the pseudoscalars), to evade precision constraints. $\tan \beta$ is fixed to unity to obtain a mixture of resonant and non-resonant processes for the $H+E_T^{\text{miss}}$ and $Z+E_T^{\text{miss}}$ searches. The DM particle mass is fixed to 10 GeV, to obtain cross-sections that are sufficiently large to be probed by Run-2 LHC searches. The spacing of the grid in M_a and M_A is left to the individual searches. The parameters $\sin \theta$, $\tan \beta$ and M_χ are scanned separately.

Scan in the M_a , $\tan \beta$ plane A two-dimensional scan in the M_a , $\tan \beta$ plane, fixing $M_A = M_H = M_{H^\pm} = 600$ GeV, is used to emphasize the complementarity of the $H+E_T^{\text{miss}}$ and $Z+E_T^{\text{miss}}$ searches with the heavy flavor + E_T^{miss} searches. The scan in M_a includes masses between 10 and 350 GeV, while the $\tan \beta$ scan includes $\tan \beta = 50, 45, 40, 35, 30, 25, 20, 15, 10, 5$, where the high- $\tan \beta$ points are of primary interest for the heavy flavor searches.

Scans in $\sin \theta$ Two one-dimensional scans in $\sin \theta$ are also suggested for further comparison of the $H/Z+E_T^{\text{miss}}$ and $b\bar{b}+E_T^{\text{miss}}$ analyses, as the latter is more sensitive at higher values of $\sin \theta$. In the first scan, resonant processes dominate with $M_A = M_H = M_{H^\pm} = 600$ GeV and $M_a = 200$ GeV, while in the second scan $M_A = M_H = M_{H^\pm} = 1000$ GeV and $M_a = 350$ GeV. For both scans, $\tan \beta$ and the DM mass are fixed to $\tan \beta = 1$ and $M_\chi = 10$ GeV. [TODO: add statement about precision constraints?]

Scan in M_χ A one-dimensional scan in M_χ spanning from 1 GeV to 500 GeV, with fixed $M_A = M_H = 600$ and $M_a = 250$ GeV, is also suggested to connect this model to a standard cosmological history. Even though the model points with where the DM particle has a mass above 100 GeV are not within immediate reach of Run-2 searches, the measured relic density is satisfied by this model at values of DM mass around 100 GeV, as shown in section 9.

8 Sensitivity studies

In the first part of this section we present the sensitivity estimates for two of the main signatures that are sensitive to the model, the $Higgs+E_T^{\text{miss}}$ and the $Z+E_T^{\text{miss}}$ signature where the Z boson decays leptonically, in the parameter scans chosen for comparison. These estimates are based on generator-level reinterpretation of existing results with 36 fb^{-1} of LHC data at a center-of-mass energy of 13 TeV. These results contain different amounts of public information. In the case of the $Higgs+E_T^{\text{miss}}$ from [99], model-independent limits

are used for the reinterpretation, while for the $Z + E_T^{\text{miss}}$ signature an estimate of the sensitivity is obtained using generator-level information from signal and published background estimates. Finally, we conclude this section with a brief outline additional signatures that are also sensitive to this model.

8.1 Studies of the $h(bb) + E_T^{\text{miss}}$ signature

The sensitivity estimates of the ATLAS and CMS $h(bb) + E_T^{\text{miss}}$ searches to the 2HDM+a scenarios are based on limits on the minimally model-dependent anomalous production of 125 GeV Higgs bosons in association with E_T^{miss} in [99]. As these limits are set in terms of the observed production cross-section of non-SM events with large E_T^{miss} and a Higgs boson, they can be compared directly to the cross-sections obtained from the 2HDM+a model after folding the detection efficiency ε times the kinematic acceptance \mathcal{A} of the event selection. This approach reduces the need for computing resources to simulate further event generation steps and detector response. The variable of interest for the sensitivity study of the $h(bb) + E_T^{\text{miss}}$ searches is the ratio between the parton-level cross-section $\sigma_i^{\text{parton}, h+\text{DM}}$ times the $H \rightarrow b\bar{b}$ branching ratio $\mathcal{B}^{\text{SM}, h \rightarrow bb}$ predicted by the SM for the 125 GeV Higgs boson, multiplied by the acceptance \mathcal{A} and detector efficiency ε , and the upper observed cross-section of the anomalous production of Higgs bosons in association with E_T^{miss} ($\sigma_i^{\text{obs}, h(bb)+E_T^{\text{miss}}}$):

$$\mathcal{S}_i \equiv \frac{\sigma_i^{\text{parton}, h+\text{DM}} \times \mathcal{B}^{\text{SM}, h \rightarrow bb} \times (\mathcal{A} \times \varepsilon)_i}{\sigma_i^{\text{obs}, h(bb)+E_T^{\text{miss}}}}, \quad (8.1)$$

where $\mathcal{B}^{\text{SM}, h \rightarrow bb}$ is the $H \rightarrow b\bar{b}$ branching ratio predicted by the SM for the 125 GeV Higgs boson. This quantity is summed over the i E_T^{miss} bins of the search, since the model will populate more than one E_T^{miss} bin at a time. A particular point in the space is excluded by the current search if $\mathcal{S}_i \geq 1$.

The expected sensitivity of $h(bb) + E_T^{\text{miss}}$ searches to the 2HDM+a model in the (M_a, M_A) plane is shown in Figure 30. The sensitivity decreases with increasing $M_A = M_H = M_{H^\pm}$ for $M_A \geq 1$ TeV because the fraction of resonant signal events drops. This drop is caused by increasingly large Γ_A , which allows for an increasing fraction of non-resonant signal events, driven by events with very off-shell A . Near the mass diagonal $M_a = M_A$, there is little to no sensitivity. This is because the Jacobian peak moves to low E_T^{miss} for a small mass splitting $|M_A - M_a|$ (as shown in Equation 6.1, Figure 6a, and Figure 6b). Moreover, the coupling g_{Aah} is small when all Higgs bosons are nearly degenerate in mass, cf. Equation 4.12 in Ref. [25], resulting in a small total cross section and therefore a further decrease in sensitivity. The sensitivity above the mass diagonal, $M_A > M_a$, is larger than below the mass diagonal. Two parameter choices cause this asymmetry:

1. The choice of $M_A = M_H = M_{H^\pm}$ forces the neutral and charged CP -even scalars to have lower masses below the diagonal and higher masses above the diagonal, leading to configurations with a lower fraction of resonant signal events. One can use Figure 13 to exemplify this behaviour. Considering the symmetry between the two

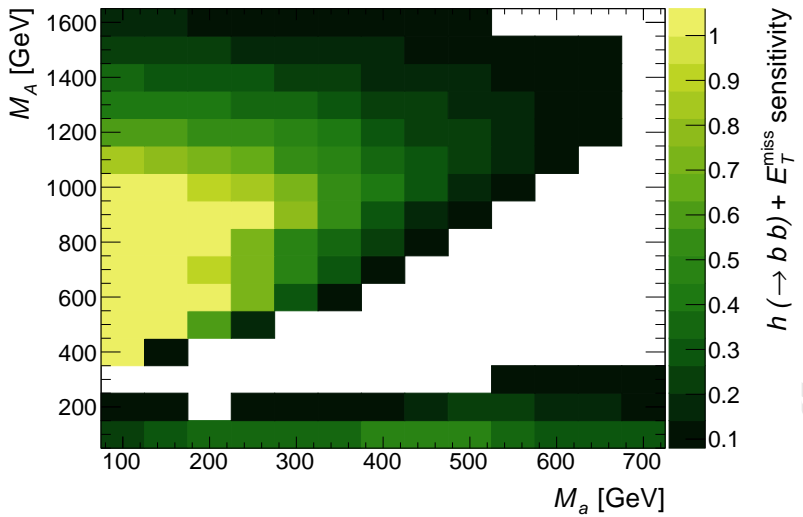


Figure 30: Sum over all E_T^{miss} -bins of the estimated sensitivity to $H \rightarrow b\bar{b} + E_T^{\text{miss}}$ events as a function of (M_A, M_a) . The sensitivity, defined as the sum of Equation 8.1 over the E_T^{miss} bins, is based on the limits with reduced model dependence from Ref. [99]. The remaining parameters take the values $M_H = M_{H^\pm} = M_A$, $\sin \theta = 0.35$, $\tan \beta = 1$, $M_\chi = 10$ GeV and $\lambda_{P1} = \lambda_{P2} = \lambda_3 = 3$. Bins with no content have a negligible sensitivity.

pseudoscalars, when the neutral and charged scalars $M_H = M_{H^\pm}$ are lighter than one of the two pseudoscalars (marked as A in the figure, but effectively representing a in the case of this scan because of the symmetry), one can see that non-resonant configurations are preferred. This also yields a reduced total cross-section.

2. The choice of $\sin \theta = 0.35 \neq 1/\sqrt{2}$ means that the mixing between the pseudoscalars A and a is asymmetric. A couples more strongly to SM particles than a , while the opposite happens to the DM fermion χ . The situation below the diagonal corresponds to the case of $\sin \theta = \sqrt{1 - 0.35^2} \approx 0.938$ and $M_A > M_a$. As it can be seen in Figure 17a, this $\sin \theta$ configuration yields a higher fraction of non-resonant signal events with low E_T^{miss} , and correspondingly a lower sensitivity is found, as also seen in Figure 32.

The scan of the sensitivity in the $(M_a, \tan \beta)$ plane is shown in Figure 31. At very low $\tan \beta$, the Yukawa coupling to top quarks is large, and most of the signal events come from non-resonant processes, as can be seen from Figure 18. The non-resonant processes are characterised by soft E_T^{miss} , which lowers the kinematic acceptance and reduces the sensitivity of the search. For higher $\tan \beta$, the fraction of resonant events increases due to the reduced top Yukawa coupling, resulting in an increase of sensitivity. However, reducing the top Yukawa coupling also reduces the total production cross section. Above $\tan \beta \approx 1.2$, the sensitivity loss due to reduced cross section outpaces the sensitivity gain due to the resonant signal. At very high $\tan \beta$ (≥ 10), this trend is reversed again because the

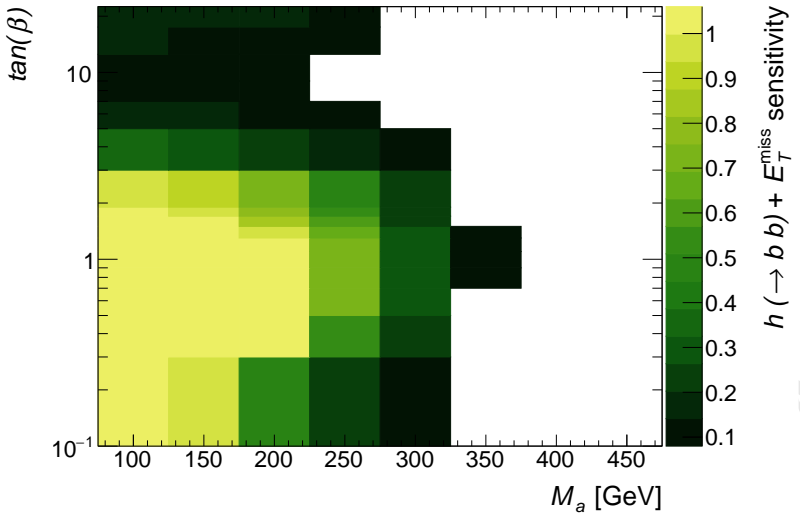


Figure 31: Sum over all E_T^{miss} -bins of the estimated signal sensitivity to $h \rightarrow bb + E_T^{\text{miss}}$ events as a function of $(M_a, \tan \beta)$. The sensitivity, defined as the sum of Equation 8.1 over the E_T^{miss} bins, is based on the limits with reduced model dependence from Ref. [99]. The remaining parameters take the values $M_H = M_{H^\pm} = M_A = 600 \text{ GeV}$, $\sin \theta = 0.35$, $M_\chi = 10 \text{ GeV}$ and $\lambda_{P1} = \lambda_{P2} = \lambda_3 = 3$. Bins with no content have a negligible sensitivity.

$\tan \beta$ enhancement² of the coupling to b -quarks compensates for the small b -quark mass. At this point bb initiated processes start to dominate the production cross section and drive the increase in sensitivity.

The sensitivity as a function of $\sin \theta$ is shown in Figure 32. The sensitivity vanishes at $\sin \theta = 0$ and $\sin \theta = 1$, since those values correspond to no mixing between A and a , and thus no connection between the SM and the dark sector. For its intermediate values, the $\sin \theta$ parameter influences the couplings of the pseudoscalars to DM as well as to SM fermions, as well as the coupling strength of the trilinear scalar vertices such as g_{Aah} [25]. Increasing these couplings increases the total cross section, but it can also increase Γ_A and thereby decrease the resonant fraction of signal events and the overall search sensitivity. For this reason, the dependence of the sensitivity on $\sin \theta$ depends on the interplay of the couplings. As a consequence, the sensitivity curve as a function of $\sin \theta$ has more than one local maximum, as shown the right panel of Figure 32.

The sensitivity to models with varying M_χ is shown in Figure 33. Below the threshold of $M_\chi < M_a/2$, the sensitivity is constant since the E_T^{miss} distribution and the total signal cross section remain unchanged. The region at threshold $M_\chi = M_a/2 \pm 5 \text{ GeV}$ (shaded in red in Figure 33) is numerically unstable and should be avoided. Above threshold, the sensitivity drops rapidly because $M_\chi > M_a/2$ requires an off-shell $a^* \rightarrow \chi\chi$ decay, which is strongly suppressed by the typically narrow width of a . The width of a is substantially reduced once $a \rightarrow \chi\chi$ is kinematically inaccessible, as $\Gamma_{a \rightarrow \chi\chi}$ is a large contribution to the total width of a for $M_\chi \leq M_a/2$ [25]. There is a slight increase in sensitivity for $M_\chi \approx M_A/2$

²The 2HDM+a scenario assumes a Yukawa sector of type II.

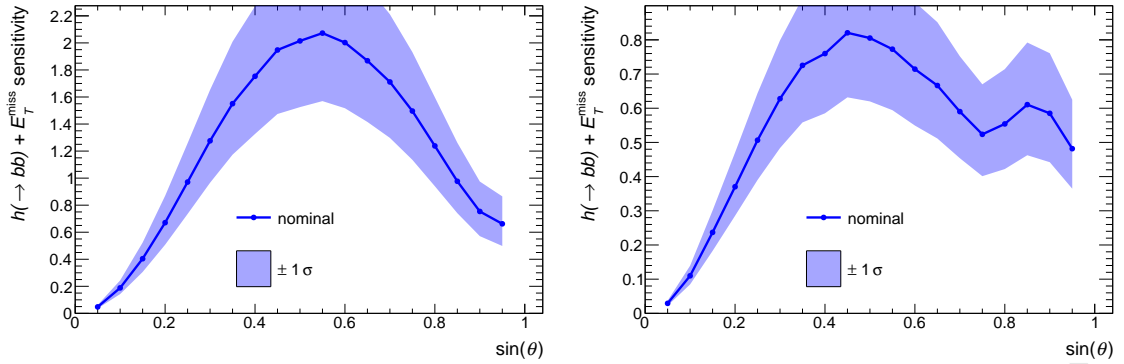


Figure 32: Sum over all E_T^{miss} -bins of the estimated signal sensitivity to $h \rightarrow bb + E_T^{\text{miss}}$ events as a function of the pseudoscalar mixing parameter $\sin \theta$, for $M_a = 200$ GeV and $M_H = M_{H^\pm} = M_A = 600$ GeV (left) as well as $M_a = 350$ GeV and $M_H = M_{H^\pm} = M_A = 1000$ GeV (right). The remaining parameters take the values $M_\chi = 10$ GeV, $\tan \beta = 1$, and $\lambda_{P1} = \lambda_{P2} = \lambda_3 = 3$. The sensitivity, defined as the sum of Equation 8.1 over the E_T^{miss} bins, as well as the uncertainty on the sensitivity (shaded blue) are based on the limits with reduced model dependence from Ref. [99] and the uncertainties described therein. Bins with no content have a negligible sensitivity.

when the $A \rightarrow \chi\chi$ decay hits its kinematic threshold, yet the absolute sensitivity remains negligible.

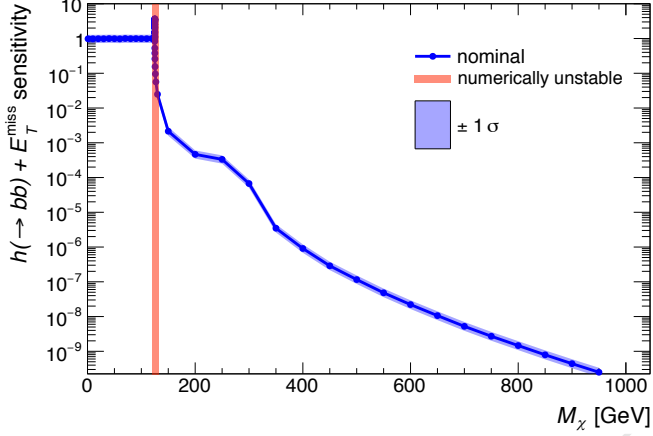


Figure 33: Sum over all E_T^{miss} -bins of the estimated signal sensitivity to $h \rightarrow bb + E_T^{\text{miss}}$ events as a function of the DM mass M_χ . The sensitivity, defined as the sum of Equation 8.1 over the E_T^{miss} bins, as well as the uncertainty on the sensitivity (shaded blue) are based on the limits with reduced model dependence from Ref. [99] and the uncertainties described therein. The remaining parameters take the values $M_a = 250$ GeV, $M_H = M_{H^\pm} = M_A = 600$ GeV, $\sin \theta = 0.35$, $\tan \beta = 1$, and $\lambda_{P1} = \lambda_{P2} = \lambda_3 = 3$. The sensitivity is constant below $M_\chi < M_a/2$, and rapidly drops for $M_\chi > M_a/2$. The sensitivity is resonantly enhanced for $M_\chi = M_a/2$.

8.2 Studies of the Z+E_T^{miss} signature

In the absence of generic limits on anomalous production of Z+E_T^{miss} events, the expected sensitivity of the Z+E_T^{miss} search to this model is approximated comparing the number of generator-level signal events to the background estimate.

The published background estimates for the leptonic channel of the Z+E_T^{miss} search, corresponding to 36 fb⁻¹ of 13 TeV data [102], are used. A reconstruction efficiency of 75% is assumed for signal events. The same selection cuts applied to data in [102] are applied to signal. Signal and background are binned in the same published E_T^{miss} bins, and a conservative background systematic uncertainty of 20% is assumed for $E_T^{\text{miss}} < 120$ GeV and 10% for $E_T^{\text{miss}} > 120$ GeV.

Following the Asimov approximation, the significance for individual bins is calculated as a Poisson ratio of likelihoods modified to incorporate systematic uncertainties on the background [106]:

$$Z'_{\text{bin}} = \sqrt{2 \cdot \left((s+b) \ln \left[\frac{(s+b)(b+\sigma_b^2)}{b^2 + (s+b)\sigma_b^2} \right] - \frac{b^2}{\sigma_b^2} \ln \left[1 + \frac{\sigma_b^2 s}{b(b+\sigma_b^2)} \right] \right)} \quad (8.2)$$

This metric has the advantage that it accounts for background systematics and is still valid for $s \gg b$. Similarly to the $h(bb) + E_T^{\text{miss}}$, case, the total significance is defined as

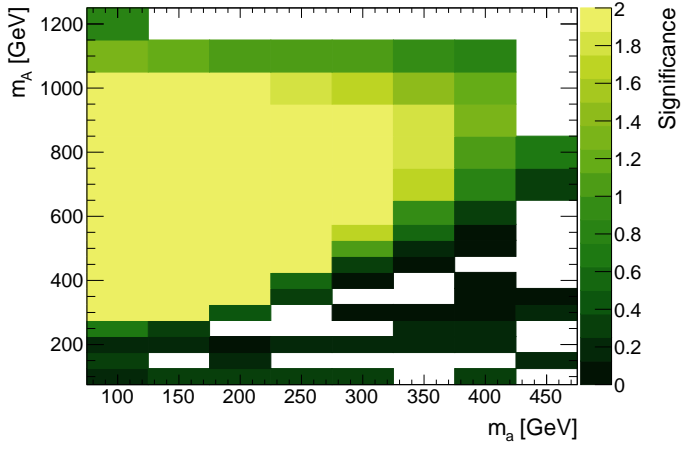


Figure 34: Expected significances for the $Z+E_T^{\text{miss}}$ leptonic signature in the (M_a, M_A) plane. Bins with no content have a negligible sensitivity.

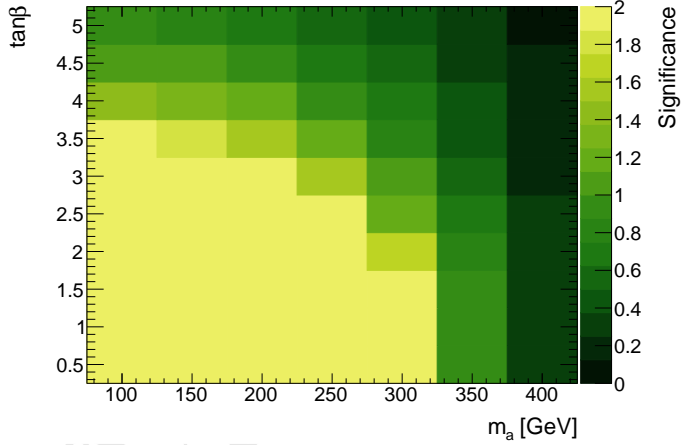


Figure 35: Expected significances for the $Z+E_T^{\text{miss}}$ leptonic signature in the $(M_a, \tan \beta)$ plane. Bins with no content have a negligible sensitivity.

the per bin significances summed in quadrature. The ATLAS and CMS experiments are expected to be sensitive to regions with significances greater than 2.

The expected sensitivity of $Z+E_T^{\text{miss}}$ searches to the 2HDM+a model in the (M_a, M_A) plane is shown in [Figure 35](#) for the leptonic case.

The sensitivity for the $Z+E_T^{\text{miss}}$ signature in the $(M_a, \tan \beta)$ plane is shown in [Figure 35](#).

The leptonic $Z+E_T^{\text{miss}}$ search provides experimental coverage of this model for a broad part of the parameter space. The pseudoscalar mediator a can be probed up to mass values of ≈ 350 GeV, depending on the choice of parameters. Leptonic $Z+E_T^{\text{miss}}$ searches are mostly sensitive in the region of $\tan \beta < 4$.

8.3 Sensitivity of other signatures

8.3.1 Heavy flavor + E_T^{miss} signatures

The choice of $\sin \theta = 0.35$ and $\tan \beta = 1$ means that the searches with heavy flavors are not sensitive to parameter scans other than the $\tan \beta$ and $\sin \theta$ scans. As discussed in subsection 6.3, it is possible to recast the results of searches reinterpreted with the pseudoscalar model from [1], but this has not been done for this whitepaper.

8.3.2 Jet+ E_T^{miss} signature

The search for events with at least one jet and large missing transverse momentum in the final states can be also interpreted in the context of the 2HDM+a model. In this scenario the pseudoscalar mediator can be radiated from heavy quark loops providing such a signature. This channel is able to probe a phase space with low $\tan \beta$ and high $\sin \theta$ in which the cross-sections of this kind of processes are enhanced, as shown in Fig. 13 of [25]. The choice of $\tan \beta = 1$ for the studies in this whitepaper highlights the complementarity between $H + E_T^{\text{miss}}$ and $Z + E_T^{\text{miss}}$ signatures; however the jet + E_T^{miss} signature is only sensitive to values of $\tan(\beta)$ up to 0.5 and is not studied in detail in this whitepaper.

Since the models used for the interpretation of the jet+ E_T^{miss} search in terms of scalar DM mediators are the same used for the HF+ E_T^{miss} searches, it is possible to reinterpret the results of the search in terms of this model using the same rescaling strategy discussed in subsection 6.3.

9 Connection with cosmology

In this section, we check the consistency of the 2HDM+a model as a function of the parameters chosen for the scans with the measured DM relic density, according to the standard thermal relic "freeze-out" scenario. This exercise requires the following assumptions, already described in Ref. [107]:

- The DM annihilation cross section receives only contributions from the interactions of the simplified model, while possible additional degrees of freedom and couplings not included in the model are irrelevant.
- The DM number density in the Universe today is entirely determined by the DM annihilation cross section predicted by the 2HDM+a. In particular, no additional mechanisms exist that enhance or deplete the relic density.

It is important to realize that if one or both of these assumptions are violated there is no strict correlation between the relic density and the strength of mono-X signals. For instance, if DM is overproduced, the relic density can be reduced if the DM has large annihilation cross sections to new hidden sector states. These states might however not be directly accessible at LHC energies. Conversely, the correct DM relic density can still be obtained if the DM is underproduced. For instance, if the hidden sector carries an particle-antiparticle asymmetry (similar to the baryon asymmetry) then this necessarily leads to a larger relic density compared to the conventional freeze-out picture.

9.1 Technical setup

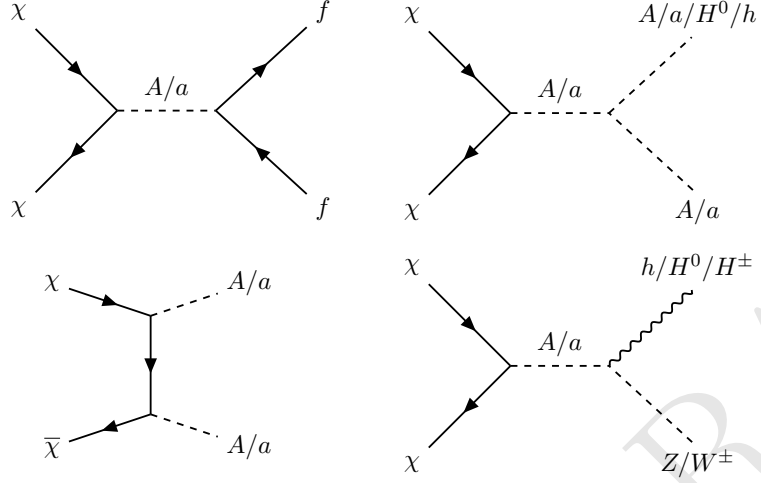


Figure 36: Annihilation diagrams taken into account in the relic density calculation.

The MADDM [108, 109] plugin for MG5_aMC@NLO is used to calculate the present-day relic density for this model. All tree-level annihilation processes are taken into account, and the Yukawa couplings of all fermions are taken to be non-zero. The Feynman diagrams of annihilation processes taken into account in this calculation are shown in Figure 36. Generally, the annihilation proceeds via single or double s-channel exchange of the pseudoscalars a and A , with subsequent decays. Since MADDM uses only tree-level diagrams, contributions from off-shell pseudoscalars can only be taken into account for the case of single s-channel mediation with direct decay of the pseudoscalars to SM fermions. If the pseudoscalars instead decay to other bosons or if the annihilation proceeds through double s-channel diagrams, the outgoing bosons are taken to be on-shell and their decays are not simulated.

Following ??, we use the parameter choices $\sin(\theta) = 0.35$, $m_h = 125\text{GeV}$, $g_\chi = 1$, $\lambda_i = 3$ for all scans in this section.

9.2 Results

The relic density is shown for in the M_a - M_χ plane in Figure 37. For small values of M_χ below the mass of the top quark, DM is mostly overabundant. In this regime, annihilation to quarks is suppressed by the small Yukawa couplings of the light fermions. The observed relic density can only be achieved for $M_\chi \approx M_a/2$, where annihilation is resonantly enhanced, or for $M_\chi \approx (M_a + M_h)/2$, close to the threshold for the $\chi\chi \rightarrow ha$ process. Above the top threshold, annihilation into fermions becomes very efficient and DM is underabundant. As M_χ increases further, annihilation via single s-channel diagrams is increasingly suppressed and the relic density rises again. The observed density is produced by this model for $M_\chi \approx 1\text{TeV}$ at low M_a . [The following sentence is being checked with Andreas Albert - would remove] For values of M_a beyond the LHC reach of a few TeV, the allowed parameter region at the top threshold $M_\chi \approx m_{\text{top}}$ remains independent

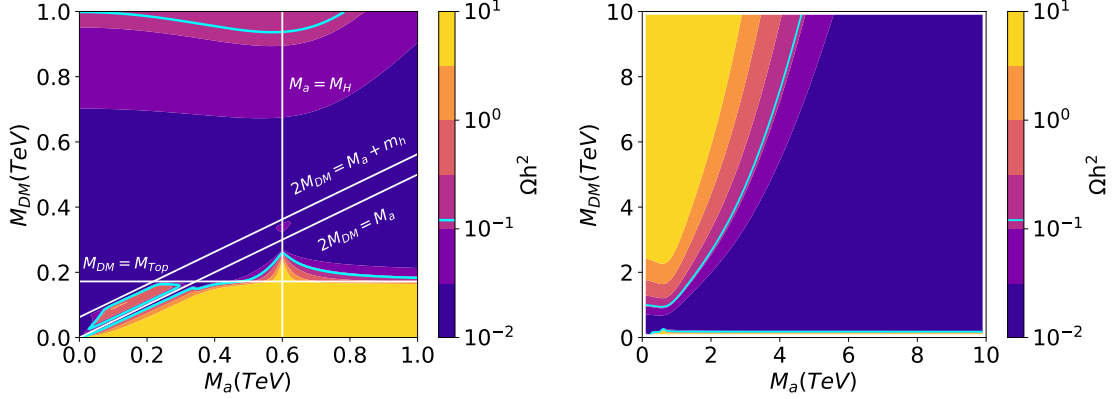


Figure 37: Predicted relic density for a two-dimensional scan of M_χ and M_a . The other parameters of the model remain fixed with $m_H = m_A = m_{H^\pm} = 600$ GeV and $\tan \beta = 1$, as well as the default choices described in the text. The color scale indicates the relic density, the cyan solid line shows the observed value of $\Omega h^2 = 0.12$. The color scale is truncated at its ends, i.e. values larger than the maximum or smaller than the minimum are shown in the same color as the maximum/minimum. While the left focuses on the mass region relevant to collider searches, the right panel shows the development of the relic density for a larger mass region.

of the value of M_a , indicating that a DM candidate that is mass degenerate with the top quark cannot be excluded by LHC searches alone.

The dependence of the relic density on the choice of M_χ is further explored by performing a one-dimensional scan as a function of the DM mass fixing $M_H = M_A = m_{H^\pm} = 600$ GeV, $M_a = 250$ GeV, and shown in Figure 38. The relic density confirms structures corresponding to the previously discussed regions of resonant enhancement and to the kinematic boundaries. Overall, the behavior is dominated by the low- M_χ suppression of the annihilation cross-section, the resonant enhancement at $M_\chi = M_a/2$ and the kinematic top thresholds. Other effects, such as the resonant enhancement of $\chi\chi \rightarrow A$ annihilation are present, but only have small effects.

The relic density values for the M_a - M_A/M_H scan described in ?? is shown in Figure 39. For the model parameters chosen in this whitepaper, the regions where the model generates a relic density compatible with the measured value are located at relatively small values of $M_a < 30$ GeV or $M_A = M_H = M_{H^\pm} < 30$ GeV, which are already excluded by LHC and LEP searches (see section 4 of Ref. [25]). The cosmological production of DM is largely driven by the choice of M_χ . As shown in subsubsection 6.2.4, the model kinematics is largely insensitive to this choice if $M_\chi < 2M_a$. Future experimental results that are sensitive to DM masses around 100 GeV which can yield the measured relic density can still be interpreted by rescaling samples generated according to this parameter scan.

The $\tan \beta$ -dependent scans, as a function of M_a and M_χ , are shown in Fig. 40. The choice of $\tan \beta$ acts as an overall modifier of the annihilation cross-section and thus the relic density, and the effect is largely independent of the choice of M_a and M_χ . For a

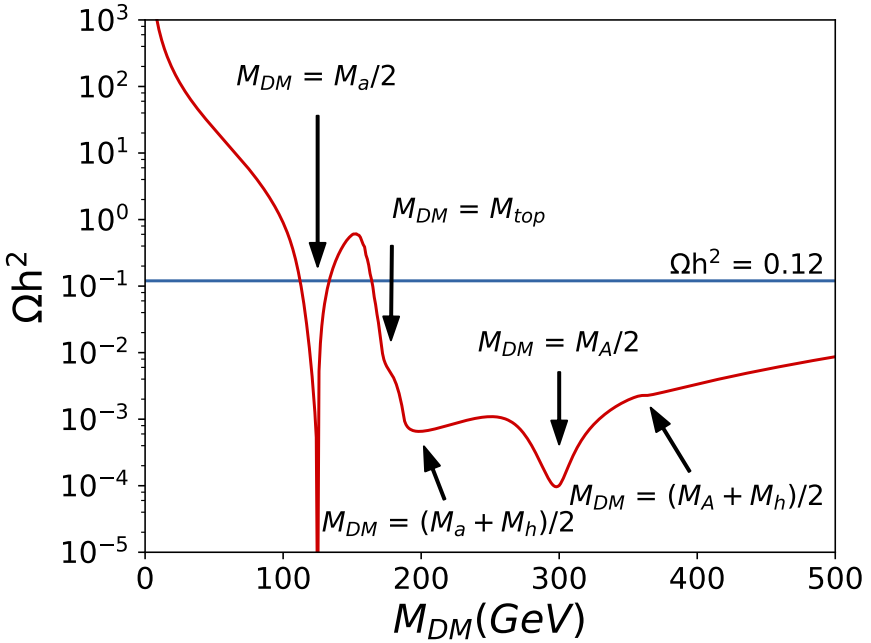


Figure 38: Relic density for a one-dimensional scan of M_χ . The other parameters of the model remain fixed with $m_H = m_A = m_{H^\pm} = 600$ GeV, $M_a = 250$ GeV and $\tan \beta = 1$, as well as the default choices described in the text. Various kinematic thresholds and regions of resonant enhancement are visible. Consistency with the observed value of $\Omega h^2 = 0.12$ is mainly controlled by the resonant enhancement of $\chi\chi \rightarrow a$, as well as the onset of $\chi\chi \rightarrow t\bar{t}$.

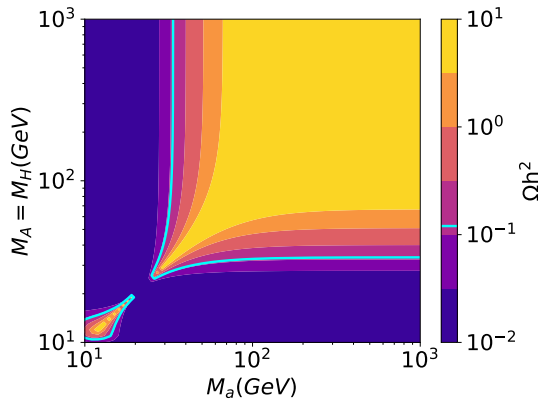


Figure 39: Predicted relic density for a two-dimensional scan of M_a and $M_A = M_H = M_{H^\pm}$. The other parameters of the model remain fixed with $M_\chi = 10$ GeV, $\tan \beta = 1$, $M_H = M_A = m_{H^\pm}$. The color coding is identical to Fig. 37.

choice of $\tan \beta \approx 0.6$, the relic density becomes maximal and steadily decreases for larger and smaller values of $\tan \beta$. In the M_χ dependent scan, where M_a is fixed to 250 GeV, the reduction of the relic density at low (≈ 0.1) and high (≈ 3) values of $\tan \beta$ leads to the

disappearance of the overabundant island around $M_\chi \approx M_a/2$.

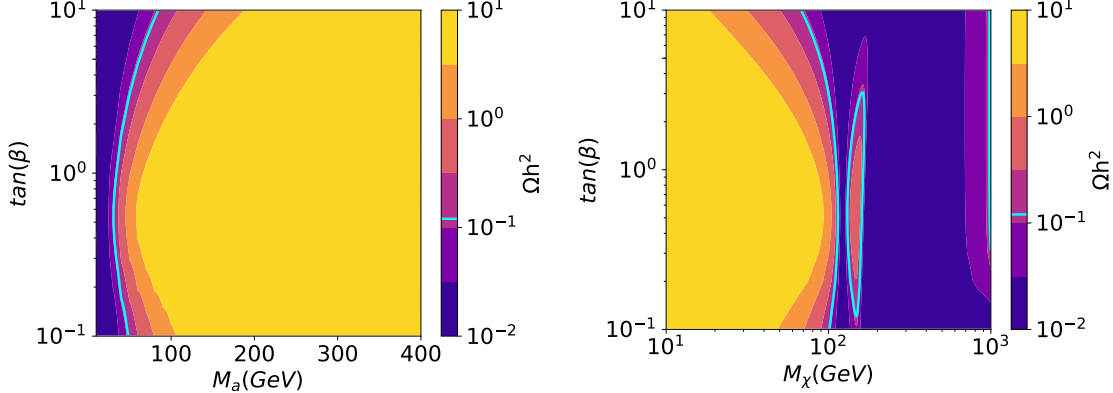


Figure 40: Predicted relic density for a two-dimensional scan of $\tan \beta$ and M_a (left), M_χ (right). In the case of the M_χ (M_a) dependent scan, $M_a = 250$ GeV ($M_\chi = 10$ GeV) is used. The other parameters of the model remain fixed with $m_H = m_A = m_{H^\pm} = 600$ GeV, as well as the default choices described in the text. The color coding is identical to Fig. 37.

10 Comparisons with non-collider experiments

10.1 Direct detection

The constraints from direct detection (DD) for a pseudoscalar mediator are generally suppressed at tree-level, so that the dominant contributions arise from loop graphs. The DD constraints in this section are generated using the 2016 LUX [110] and XENON1T [111] data, via an effective operator approach using tools from [112].

At tree level, the spin-independent scattering cross section is absent. The spin-independent cross section is non-zero, but highly suppressed due to a dependence on q_{tr}^4 . At loop level, however, a spin-independent cross section is generated through the diagrams in Fig. 41.

The triangle diagram in the left panel of Fig. 41 is proportional to m_q while the box diagrams in the central and right panels of Fig. 41 are proportional to m_q^3 , thus the box diagrams are sub-leading except for the case of Type II Yukawa couplings with $\tan \beta \gtrsim 50$, as found in [32]. The triangle diagram does not depend on the Yukawa sector of the 2HDM.
** cite our paper in preparation**

The DD limits for this model are presented in Fig. ?? and 42 for two benchmark points in $\cos \theta$ and M_A . Limits are calculated using ???. The heavier pseudoscalar is set to $M_A = 750$ GeV, and the mixing angles are fixed to $\sin \theta = 0.7$ in the left panel, $\sin \theta = 0.35$ in the right panel and $\cos \theta = 0.35$ in the bottom panel. In the first case, current limits are able to exclude the portion of parameter space with $20\text{GeV} \lesssim m_\chi \lesssim 200\text{GeV}$ and $M_a \lesssim 40\text{GeV}$. Projected limits for XENON1T and XENONnT could expand the excluded region to $10\text{GeV} \lesssim m_\chi \lesssim 1\text{TeV}$ and $M_a \lesssim 150\text{GeV}$. For $M_a \gtrsim 300\text{GeV}$ or $m_\chi \gtrsim 3\text{TeV}$, this model has cross-sections equivalent to those of neutrino scattering. The second case is

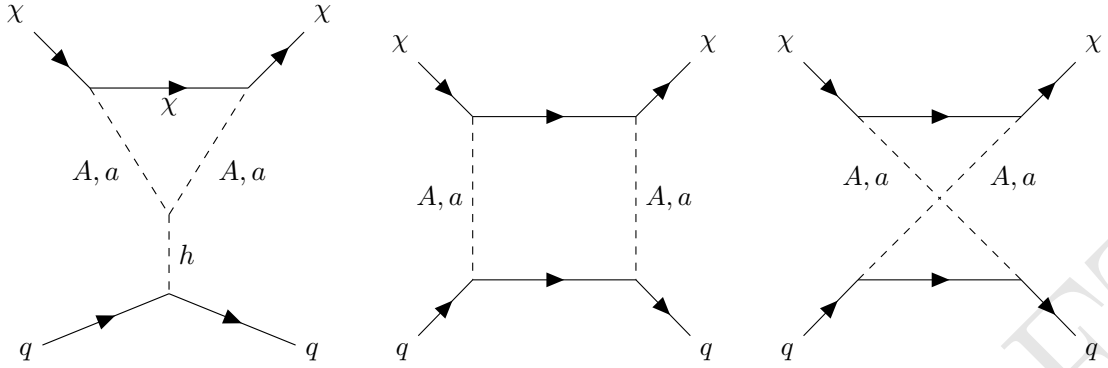


Figure 41: Spin-independent DM-nucleon scattering arises from the loop exchange of the mixing pseudoscalar mediators. Left panel: triangle diagram. Central and right panel: box diagrams.

quite similar to the first, with the limits just slightly weakened by the smaller mixing angle. In the last case, for $\cos \theta = 0.35$, current DD experiments can only probe a small portion of the parameter space, with $20\text{GeV} \lesssim m_\chi \lesssim 70\text{GeV}$ and $M_a \lesssim 4\text{GeV}$. Projected limits expand the range to up $M_a \sim 40\text{GeV}$ and $m_\chi \sim 400\text{GeV}$, while neutrino cross-sections are reached in region beyond $M_A \gtrsim 100\text{GeV}$ or $m_\chi \gtrsim 1\text{TeV}$. In the 3 panels we also include limits from the Higgs to invisible BR [68, 69], coming from 2 and 3 body decays, as described in [25]. They rule out the low m_χ, M_a mass region.

The DD sensitivity to the scalar model differs from that to pseudoscalar model, as the scalar model features an unsuppressed SI scattering cross section. For the scalar model, DD excludes significant parameter space, unless the scalar masses are approximately degenerate [71].

10.2 Indirect detection

Due to the large number of interactions the mediating pseudoscalar has with the Standard Model sector, the indirect detection signals for this model are quite complex. In short, Dark Matter can annihilate into many final state particle pairs, and an increasing number of distinct event topologies become kinematically accessible with increasing Dark Matter mass. Not only can the DM annihilate to various pairs of Standard Model particles, but DM may also annihilate into single SM gauge boson produced in association with an unstable Higgs sector particle, or into two Higgs sector particles. In turn, the Higgs sector particles will decay to pairs of SM particles, therefore the final states of DM annihilation may contain 2, 3 or 4 SM particles and the content of the dominant annihilation channel will not only depend on the Higgs sector parameters and Dark Matter mass. When fixing the coupling parameters and varying the DM mass, one can see the changes in the dominant DM annihilation channels as the different energy thresholds are crossed, as shown in this section.

To illustrate the complexity of the DM annihilation channels which contribute to indirect detection, Figure 43 shows the total DM annihilation rate vs Dark Matter mass

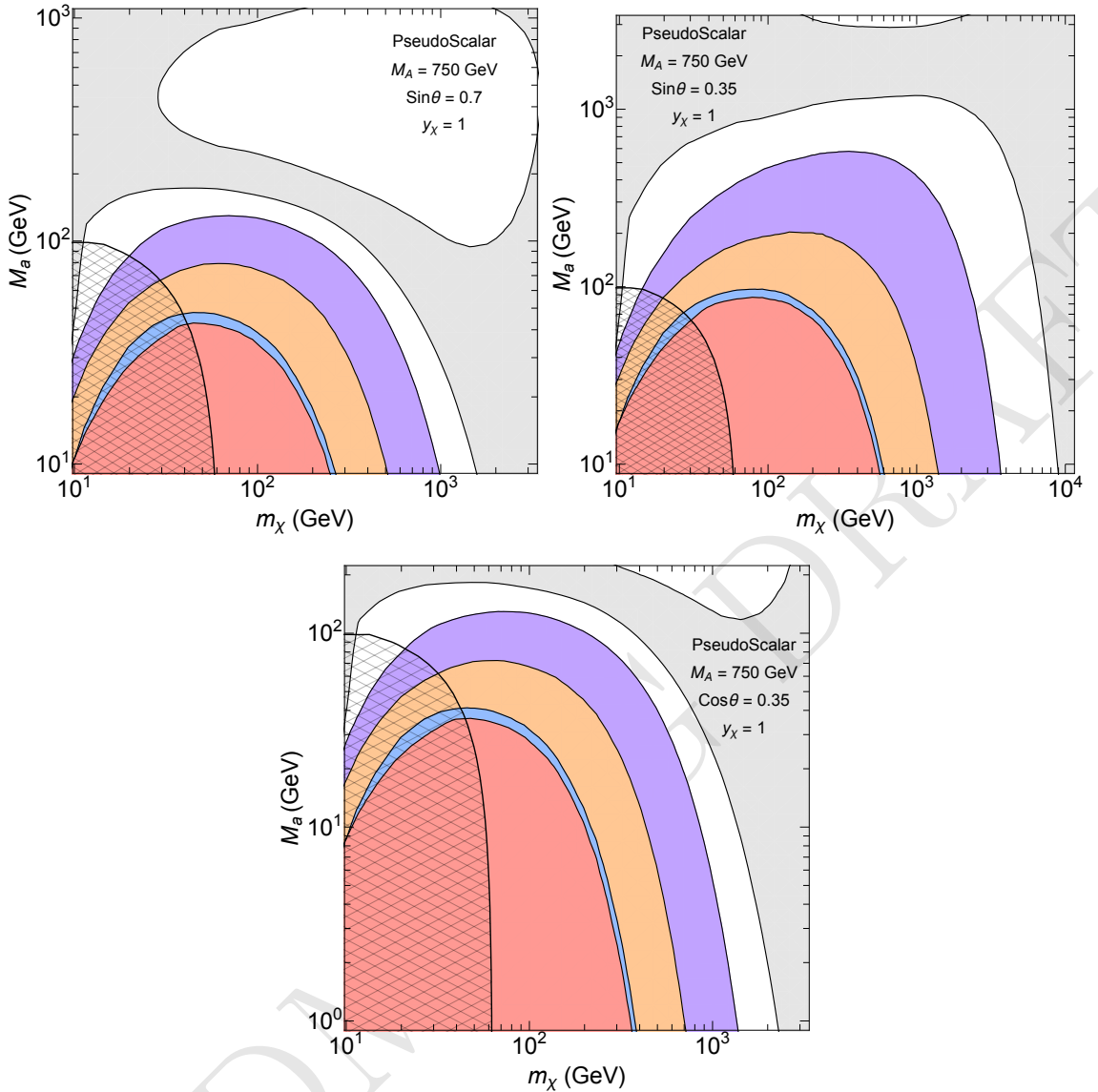


Figure 42: DD exclusion and projections for the two benchmark points in $\cos \theta$ and M_A for various experiments for this model. The various regions refer, in order, to LUX [110], XENON1T[111], XENON1T and XENONnT projections [113], and neutrino background [114]. Top Left panel uses $\sin \theta = 0.7$, top right panel uses $\cos \theta = 0.35$, bottom panel uses $\cos \theta = 0.35$, while $M_A = 750\text{GeV}$ in all the panels.

for specific benchmark values of the Higgs sector parameters. The cross sections were calculated using the Madgraph version of the model available on the DMWG repository ?? and the MadDM plugin[115].

As the DM mass increased the dominant annihilation channel varies greatly. For light Dark Matter masses, under about 150 GeV, the annihilation rate is dominated by b-quark pairs, as they are the kinematically accessible particles that have the largest Yukawa

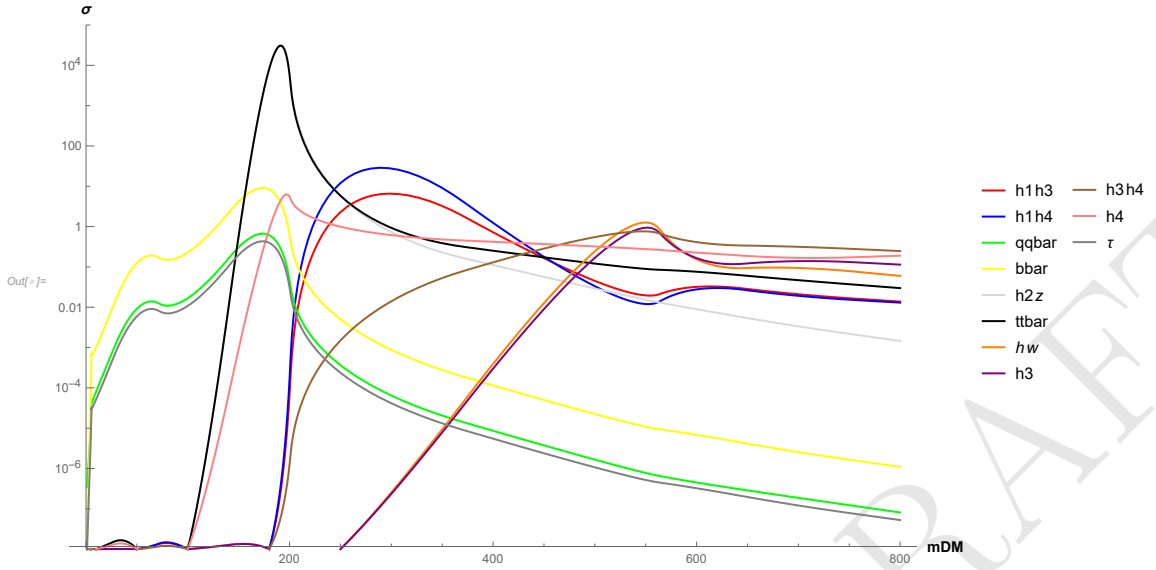


Figure 43: A Plot of the leading Dark Matter partial annihilation cross sections, in picobarns, to various final state particle pairs, vs Dark Matter Mass (GeV). The curves include annihilation rates into fermions, pairs of Higgs sector particles, and Vector Boson-Higgs pairs.

coupling to the Higgs-sector mediator. This situation resembles the light Higgs boson decay rates, dominated by bottom quarks. A new annihilation channel into a Higgs and Z boson opens when the threshold $m_{DM} \rightarrow m_h + m_Z$ is crossed. Next, the $m_{DM} \rightarrow m_t$, where the di-top channel opens and contributes significantly to the annihilation rate. The next threshold to be crossed is $2m_{DM} \rightarrow m_a + m_h$, where the light pseudo-scalar will decay to bottom quarks. The event is thus likely $2m_{DM} > 4b$, however the momentum distribution between the two pairs of bottoms will be asymmetric. It is expected that the total annihilation rate into this channel is appreciable since there is a large coupling between the Higgs and the pseudoscalar which also involves mass insertion. This type of event topology, $DMDM \rightarrow X + SM$, where X is a decaying hidden sector particle, has not been extensively studied on its own. Next, the threshold $2m_{DM} > m_V + m_H$ is crossed, where V is the mass of a heavy vector boson, and H is a heavier Higgs sector field. Along with all of this, modes will significantly contribute where DM annihilates to pairs of Higgs sector fields. The most important, and lowest threshold is $m_{DM} \rightarrow m_a$, where the annihilation channel into two pseudoscalars is open. There are also thresholds where DM annihilates to any pair of heavy (or one heavy and one light) Higgs sector field.

A few general notes are in order here. First, the effect of the new annihilation channels opening as thresholds are crossed may also be witnessed in figure 26 which charts the relic density as a function of DM mass for fixed values of the Higgs-sector parameters. One can see, for example, the effect of the di-top channel turning on as the overall annihilation rate is enhanced and the relic density drops. A similar powerful effect is observed as the threshold $2m_{DM} \rightarrow m_a + m_h$ is crossed. The significant drop in relic density at this

threshold demonstrates that this is an important annihilation channel which can compete or even dominate the list of partial annihilation rates. The annihilation rate is enhanced as the resonance thresholds $2m_{DM} = m_a, m_A$ are crossed, which will lead to stronger constraints from total photon flux measurements from indirect detection (ID) experiments.

We note that indirect detection constraints for models of the complexity of kinematics displayed here have not yet been well studied. In much of parameter space, the annihilation cross sections are not simply dominated by a single final state channel, several distinct channels often have significant contributions. Since many channels will contribute to over-all photon flux and limits obtained from flux observation will require that these distinct spectra using a method similar to reference [116, 117] to combine channels. The total photon flux expected from DM annihilations will be

$$\Phi_\gamma = \frac{1}{4\pi} \sum_f \frac{\langle \sigma v \rangle}{2m_\chi^2} \int_{E_{min}}^{E_{max}} \left(\frac{dN_\gamma}{dE_\gamma} \right)_f dE_\gamma J \quad (10.1)$$

where the J -factor ($\text{GeV}^2\text{cm}^{-5}$) is the line of sight integral of the DM density ρ , integrated over a solid angle: $\Delta\Omega$, m_χ is the Dark Matter mass, and we must sum over all accessible partial annihilation rates $\langle \sigma v \rangle_f$, where f specifies the distinct final state. These predictions of total integrated flux may then be compared to observational measurements, for example of dwarf galaxies or the galactic center, which may constrain the partial annihilation rates and thus provide limits on the model parameters. In reference [116], complex models with several annihilation channels were constrained using the Fermi dwarf galaxy data, where the observations of each dwarf galaxy was stacked in a joint-likelihood analysis. Such a procedure would be optimal for setting limits on this model from existing observational data. Below, we briefly describe the effect of various mass thresholds on the admixture of partial annihilation rates in our model.

The annihilations which involve the unstable Higgs fields will have more complicated kinematics than simple DM annihilation to 2 SM particles. Some work has been done regarding shifts in the annihilation spectrum resulting a very symmetric process where DM pairs annihilate to 2 or more identical heavy states that then decay to pairs of SM particles [118]. Our model presents this as a possible annihilation process, along with others which have not yet been analysed. These include the asymmetric process where 2 decaying Higgs sector particles of differing masses are produced and other asymmetric processes where light SM particle is produced in association with a heavier Higgs sector particle. The full parameter space of this model presents a wide area of admixtures of annihilation channels, and thus many possibilities for total integrates photon spectra. We see that this type of 2HDM is quite complex, both in the number of annihilation channels and in kinematics as well.

11 Conclusions

Appendix

A Details on MC generation

Mono-Higgs signature The studies of the $h(bb) + E_T^{\text{miss}}$ channel presented here are based on MC simulations with version 2.4.3 of MADGRAPH 5 [119] using a Universal FeynRules Output [120] implementation of the 2HDM with a Yukawa sector of type II with DM mediator (2HDM+a), as provided by the authors of [25]. The NNPDF30_lo_as_0130 set of parton distribution functions (PDF) at leading order in the five-flavor scheme, which assumes a massless b -quark, with $\alpha_S(m_Z) = 0.130$ is used for these simulations [121]. For consistency, five-flavor scheme and $m_b = 0$ GeV are chosen for the matrix element (ME) computation in MADGRAPH 5.

The ME generated for the parton-level studies presented in the following is $gg \rightarrow h\chi\chi$ represented in ?? The only exception is the $M_a - \tan\beta$ scan which will be discussed in the following and is summarised in Figure 31. In this scan also the ME $bb \rightarrow h\chi\chi$ is generated because at high $\tan\beta$, the bb initiated process can have an amplitude of a similar magnitude as the gluon fusion initiated process from ?? [25]. The gluon fusion is dominant in all the remaining parameter space, therefore the bb initiated process and other negligible contributions are not considered explicitly for all the scans.

Mono-Z signature: leptonic channel Simulated event samples for the leptonic mono-Z signature are produced with Madgraph5_aMC@NLO version 2.4.3, interfaced with Pythia version 8.2.2.6 for parton showering. The NNPDF3.0 PDF set is used at LO precision with the value of the strong coupling constant set to $\alpha_S(M_Z) = 0.130$ (NNPDF30_lo_as_0130). A five flavor scheme with a massless b -quark is used. Only contributions from gluon-gluon initial states and $l^+ l^- \chi\bar{\chi}$ final states are considered, where $l = e$ or μ . The bb initiated ME contribution is negligible for the range of $\tan\beta$ values studied. To increase calculation efficiency diagrams with an intermediate s-channel SM Higgs boson are explicitly rejected (generate $g\ g > xd\ xd\ l^+ l^- / h1$).

Mono-Z signature: hadronic channel Simulation of mono- Z hadronic events is performed using a setup similar to that used for the leptonic events. The Madgraph5_aMC@NLO version 2.4.3, interfaced with Pythia version 8.212 for parton showering and the LO NNPDF3.0 with $\alpha_S(M_Z) = 0.130$ for PDF in the matrix element calculations, is used for the event generation. Only gluon-gluon initial states are considered for the production of mono- Z events. In contrast to the leptonic case, the Z -boson is explicitly required in the intermediate state ($g\ g > xd\ xd \sim z$) to ensure that non- Z hadronic events are suppressed in the produced sample. The MadSpin is used for the Z decay to maintain a proper spin correlation between the Z decay quarks.

Table 1: Event selection requirements for the analysis of the Mono-Z signature with leptonic Z decays. The requirements are inspired to follow those used in typical experimental analyses.

Selection stage	Quantity	Requirement
Inclusive	lepton $ \eta $	< 2.5
	leading (trailing) lepton p_T	$> 25(20)$ GeV
Preselection	$ m_{ll} - m_{Z,\text{nominal}} / E_T^{\text{miss}}$	< 15 GeV > 40 GeV
	$\Delta\Phi(ll, E_T^{\text{miss}})$	> 2.7
	$ p_{T,ll} - E_T^{\text{miss}} / p_{T,ll}$	< 0.4
	$\Delta R(ll)$	< 1.8
Final selection	E_T^{miss}	> 80 GeV
	$\Delta\Phi(ll, E_T^{\text{miss}})$	> 2.7
	$ p_{T,ll} - E_T^{\text{miss}} / p_{T,ll}$	< 0.4
	$\Delta R(ll)$	< 1.8

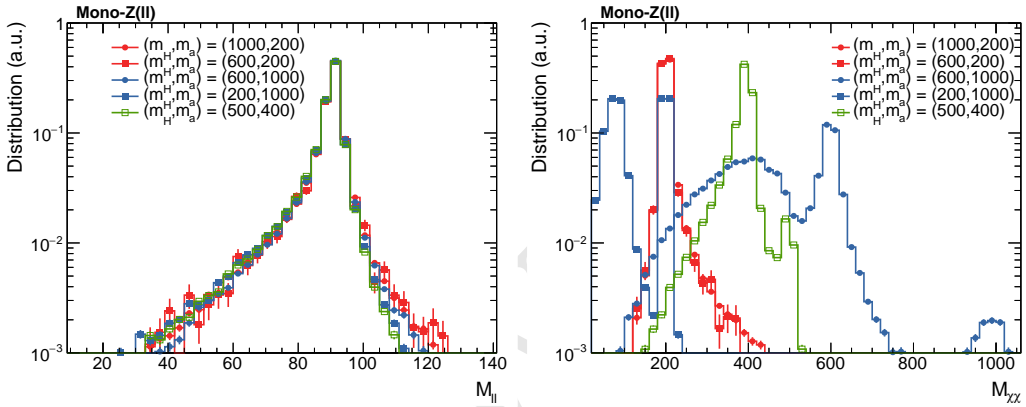


Figure 44: Distributions of the invariant mass of the dilepton (left) and $\chi\bar{\chi}$ systems (right) with no selection applied in addition to the generation cuts. The M_{ll} distribution is centered around the Z boson mass independent of the chosen parameter point, indicating that there is no contribution from γ^* exchange. The $M_{\chi\bar{\chi}}$ distribution

B Additional kinematic distributions

Signatures including a Z boson

Z + E_T^{miss} signature, leptonic channel Inclusive distributions of the invariant masses of the dilepton and $\chi\chi$ systems are shown in Figure 44 (before preselection). Independently of the parameters, the dilepton mass spectrum is centered at the Z peak, without any nonresonant contribution. The $M_{\chi\bar{\chi}}$ distribution illustrates the signal contributions from different diagrams. For $M_A > M_a$, DM is dominantly produced from on-shell a boson production. In the inverted mass region $M_A < M_a$, the situation is reversed, and H diagrams dominate.

The distributions of some relevant variables for this search are shown in Figure 45, after preselection.

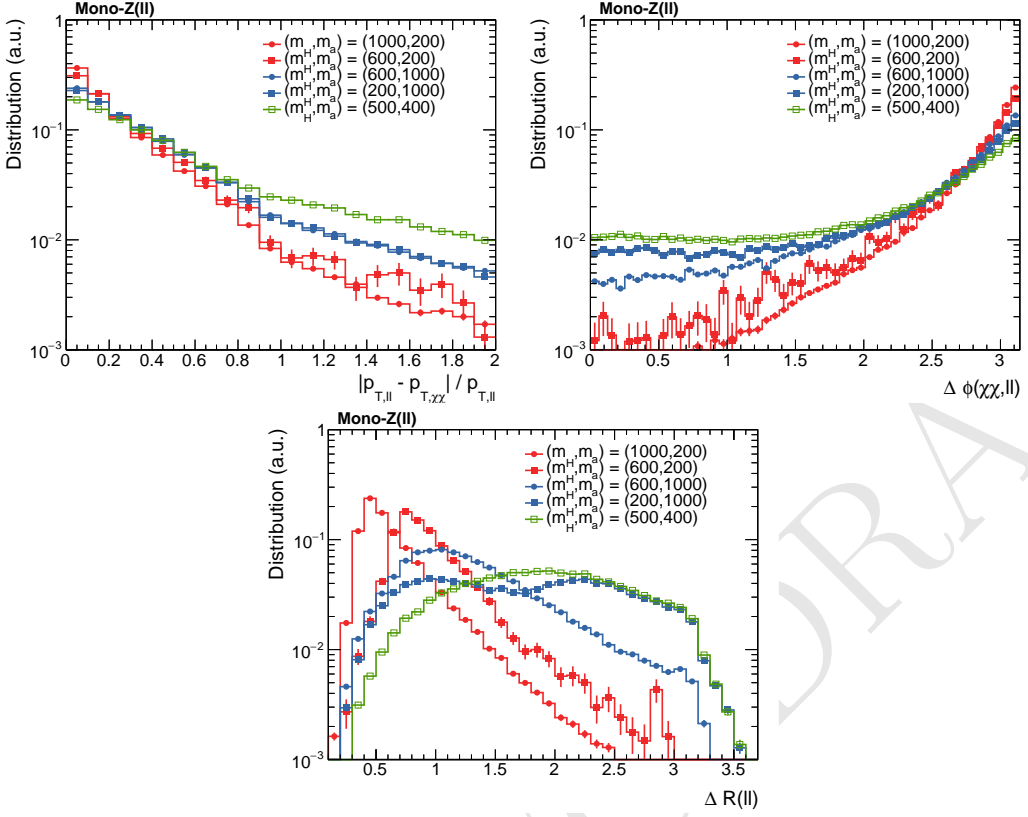


Figure 45: Distributions of the main selection variables after preselection: p_T balance (top panel), $\Delta\Phi$ (middle) and ΔR (bottom). The shown parameter points illustrate the different qualitative behavior in the three different mass regions.

Table 2: Event selections used in the analysis for the mono- Z hadronic signature with $Z \rightarrow q\bar{q}$ decays. The requirements are inspired from those used in a typical experimental analysis. The j (J) stands for the small-radius (large-radius) jet in the resolved (boosted) analysis.

Selection stage	Quantity	Requirement
Inclusive resolved and boosted selections	Jet radius	= 0.4 (1.0)
	Jet $ \eta $	< 2.5 (2.0)
	Jet p_T	> 25 GeV (200)
	Number of jets	≥ 2 (1)
Final resolved and boosted selections	$ m_{jj \text{ or } J} - m_Z $	< 15 GeV
	$\Delta\Phi(jj \text{ or } J, E_T^{\text{miss}})$	> 2
	E_T^{miss}	> 100 (250) GeV

$Z + E_T^{\text{miss}}$ signature, hadronic channel The event selection criteria used in this analysis are listed in Table 2.

Figure 46 shows the kinematic distributions of mono- Z events after applying the

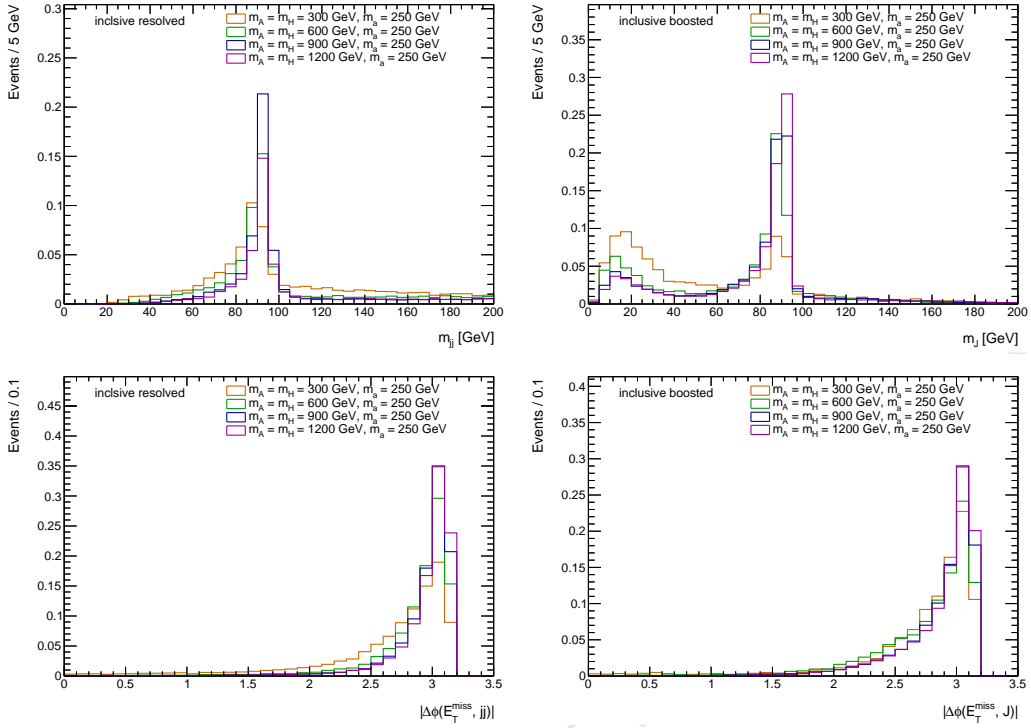


Figure 46: Dijet mass (top), $\Delta\Phi(jj, E_T^{\text{miss}})$ (bottom) distributions after applying the inclusive selections in the resolved analysis are shown on the left side. Large-radius jet mass (top), $\Delta\Phi(J, E_T^{\text{miss}})$ (bottom) distributions after applying the inclusive selections in the boosted analysis are shown on the right side. The signal masses are chosen to be $M_A = 300, 600, 900$ and 1200 GeV with the fixed $M_a = 250 \text{ GeV}$.

inclusive selections, separately for the resolved and boosted topologies. The M_a is fixed to 250 GeV and the M_A is chosen to be 300, 600, 900 and 1200 GeV in the figure. When the M_A gets closer to M_a , the Z -boson is less boosted, causing the large-radius jet mass to be more populated at mass below $\sim 30 \text{ GeV}$. When the $|M_A - M_a|$ becomes smaller than the Z -boson mass, the non-resonant production dominates as clearly seen in the E_T^{miss} spectrum for the resolved case. Figure 47 shows the same set of distributions when the M_A is fixed to 600 GeV and the M_a varies from 150 to 250, 350 and 450 GeV. The trend seen in Fig. 46 is also visible here when the M_a gets closer to M_A .

C Cross-section and acceptances for selected signatures

Signatures including a Z boson

Z+ E_T^{miss} signature, leptonic channel The overall cross-sections in the $\tan\beta$ and mass scans are shown in Fig. 48.

In the mass scan, maximal cross-sections are observed for the region of $M_a < M_A$ for values of $M_a \gtrsim 100 \text{ GeV}$. Towards higher values of both M_a and M_A , the cross-sections fall off, reaching values smaller than 1 fb at $M_a \approx 450 \text{ GeV}$ or $M_A \approx 1.1 \text{ TeV}$. In

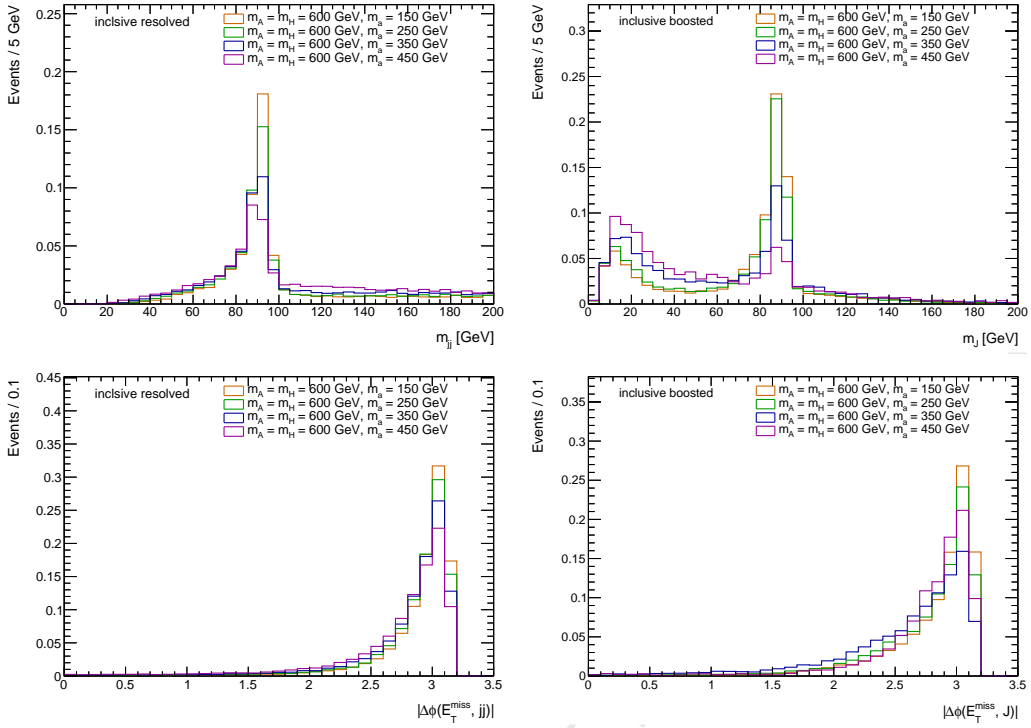


Figure 47: Dijet mass (top), $\Delta\Phi(jj, E_T^{\text{miss}})$ (bottom) distributions after applying the inclusive selections in the resolved analysis are shown on the left side. Large-radius jet mass (top), $\Delta\Phi(J, E_T^{\text{miss}})$ (bottom) distributions after applying the inclusive selections in the boosted analysis are shown on the right side. The signal masses are chosen to be $M_a = 150, 250, 350$ and 450 GeV with the fixed $M_A = 600 \text{ GeV}$.

the $M_a \approx M_A$ -region, the cross-section is suppressed by destructive interference. For the region with inverted mass hierarchy $M_a > M_A$, cross-sections of the order of multiple fb are observed, as long as $|M_a - M_A|$ remains sufficiently large. In the $\tan\beta$ scan, cross-sections smoothly fall with increasing M_a as well as $\tan\beta$. Cross-sections are typically larger than 1 fb up to $\tan\beta \approx 5$. The M_a dependence is modulated by the value of $\tan\beta$: Crossing the M_a range from 100 to 400 GeV, cross-sections are reduced by a factor ≈ 7 for small $\tan\beta \approx 1$, but only a factor ≈ 2 for higher values of $\tan\beta \approx 5$. In the $\sin\theta$ scan shown in Figure 49, cross sections depends on whether or not the $a \rightarrow \bar{t}t$ decays are accessible. For $M_a < 350 \text{ GeV}$ they are not accessible and cross section strictly increases with $\sin\theta$. For $M_a > 350 \text{ GeV}$, the $a \rightarrow \bar{t}t$ decays become possible causing the cross section to decrease for large values of $\sin\theta$.

Z+ E_T^{miss} signature, hadronic channel Figure 50 shows the production cross-section for mono-Z events in the M_a (M_A) range between 100 and 500 GeV (200 and 1200 GeV). Shown on the left (right) is the cross-section in the M_a vs M_A (M_a vs $\tan\beta$) grid. Note that the $Z \rightarrow q\bar{q}$ branching fraction is not included in the cross-section. The production cross-section tends to vanish in the region where the M_a gets close to M_A , as shown by the empty points in the grid.

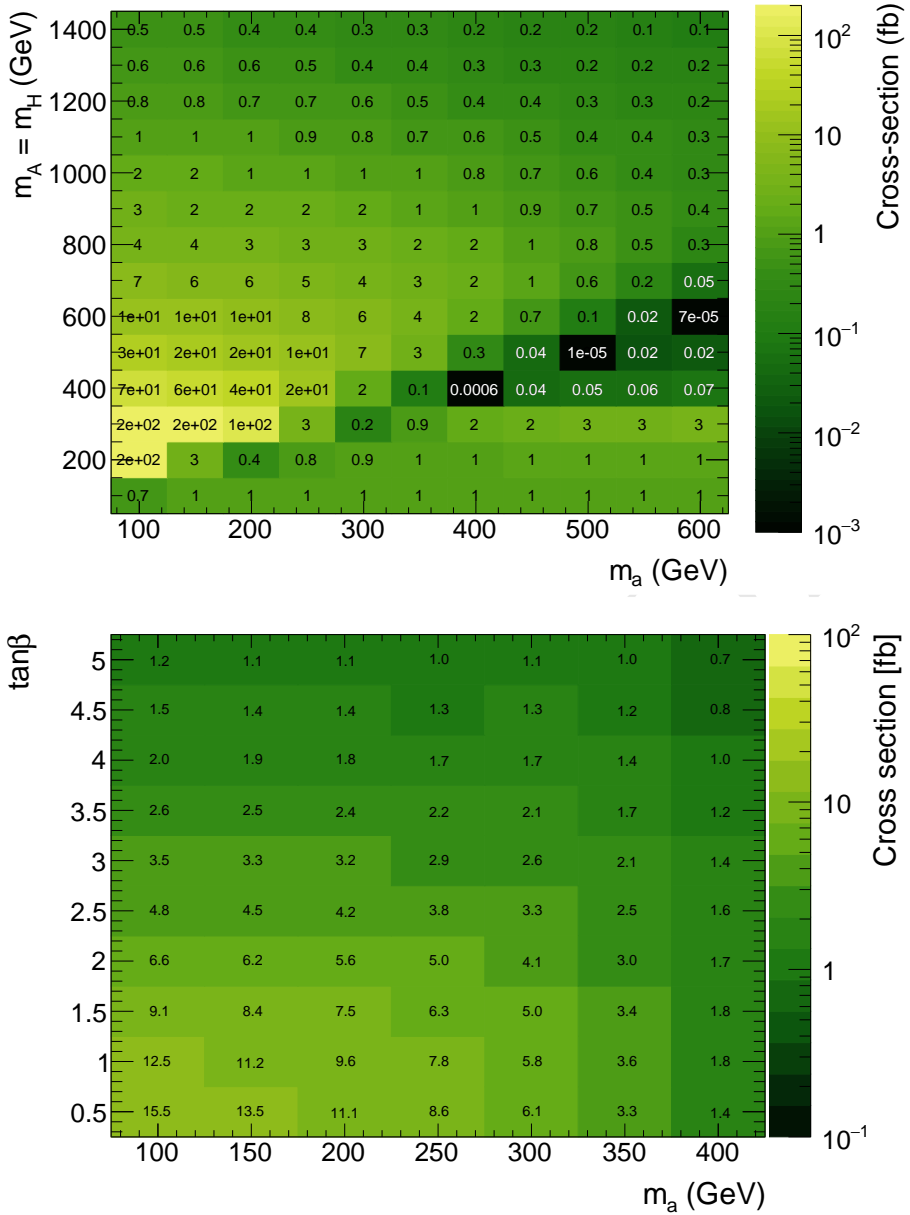


Figure 48: Inclusive cross-sections for $pp \rightarrow l^+l^-\chi\bar{\chi}$ in the M_a - M_A (top) and M_a - $\tan\beta$ scans (bottom).

The signal acceptance for the four sets of event selections given in Table 2 is summarized in Fig. 51 in the M_a vs M_A grid. Note again that the resolved and boosted selection criteria are applied separately for the inclusive case, while for the final selections the boosted criteria are applied first and then the resolved ones to those failing the boosted criteria. For the inclusive case, the mass dependence on the acceptance is weak for the resolved criteria while it is rather significant for the boosted criteria as the Z -boson is less boosted with decreasing M_A and hence less likely that the Z -decay products are merged

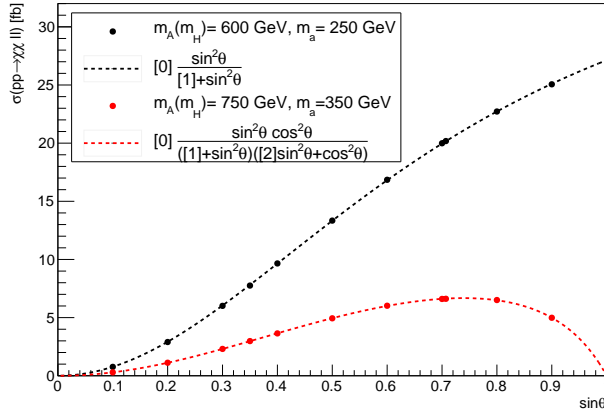


Figure 49: For two different mass points, this figure shows the cross section $pp \rightarrow \chi\chi\ell\ell$ as a function of $\sin \theta$. For $M_a < 350$ GeV, a decays solely to dark matter particles. As a consequence, the mixing angle only impacts the heavy scalar’s branching fraction to aZ and cross section strictly increases with $\sin \theta$. For M_a above 350 GeV, $t\bar{t}$ decays become accessible, introducing additional $\sin \theta$ and $\cos \theta$ dependences for the branching fraction of $a \rightarrow \chi\chi$. For M_a above 350 GeV for large values of $\sin \theta$, there is a turnover point where the reduced $a \rightarrow \chi\chi$ branching fraction outweighs the increased $H \rightarrow aZ$ branching and the net cross section decreases.

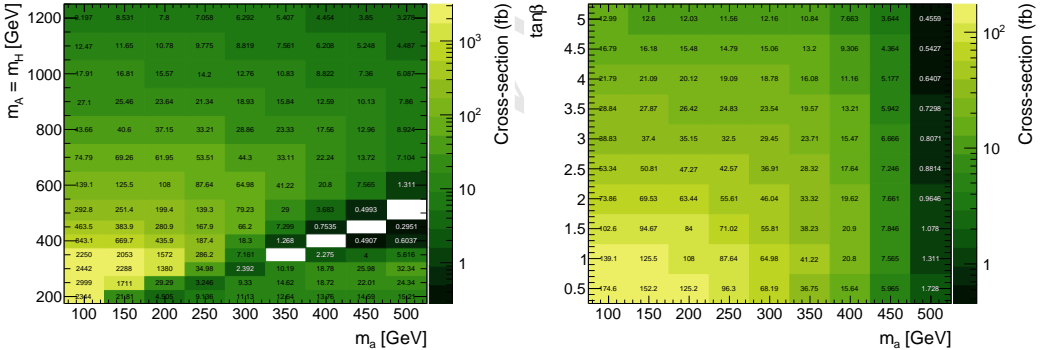


Figure 50: Inclusive cross-sections for the mono- Z hadronic events $pp \rightarrow Z(\rightarrow q\bar{q})\chi\bar{\chi}$ in the M_a vs M_A (left) and M_a vs $\tan \beta$ (right) grids. The $Z \rightarrow q\bar{q}$ branching fraction is not included in the cross-section.

into a single jet. The final boosted selections have acceptance larger than $\sim 20\%$ (40%) at $M_A > 800$ (1000) GeV and $M_a < 400$ GeV. The final resolved selections can recover 10-20% of signal events which fail the boosted criteria in the same mass regions. At $M_A < 600$ GeV the signal acceptance is dominated by the resolved selection criteria.

The signal acceptance in the M_a vs $\tan \beta$ space is shown in Fig. 52. The conventions used in Fig. 52 are the same as those in Fig. 51. The signal acceptance is rather independent of $\tan \beta$ except at low $\tan \beta$ region; the acceptance tends to be slightly lower at $\tan \beta < 1$

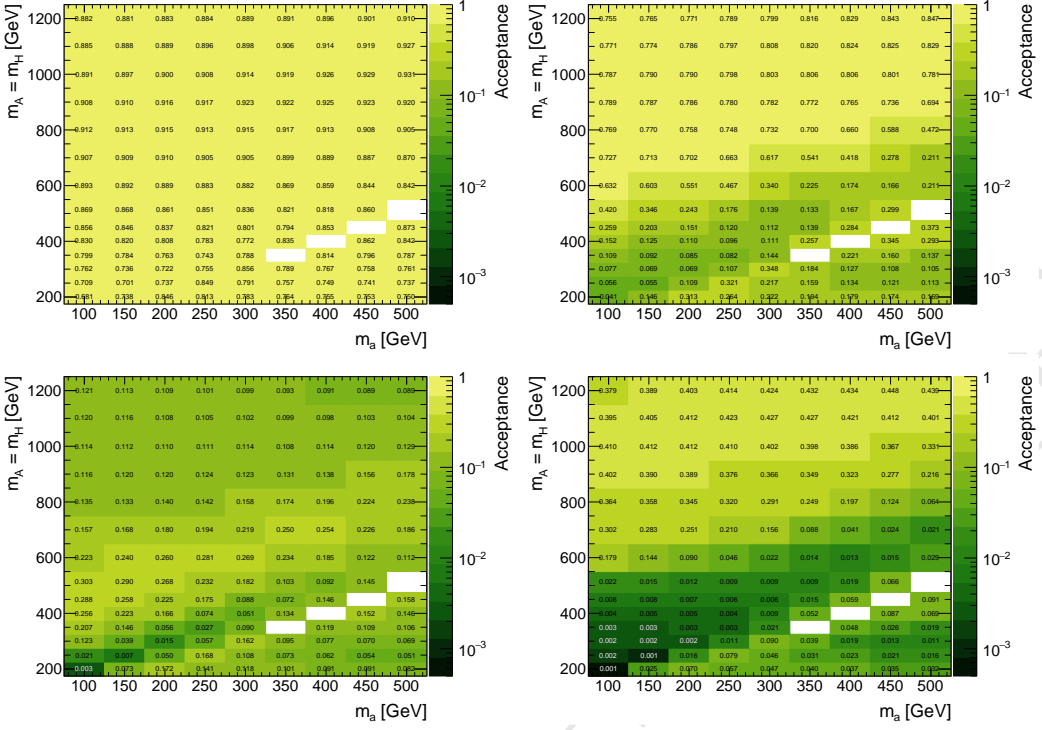


Figure 51: Acceptance for the inclusive (top) and final (bottom) selections for the mono- Z hadronic events $pp \rightarrow Z(\rightarrow q\bar{q})\chi\bar{\chi}$ in the M_a vs M_A grid. Shown on the left (right) is the acceptance for the resolved (boosted) analysis selections.

than at > 1 for $M_a < \sim 250$ GeV while it's opposite for $M_a > \sim 250$ GeV. The acceptance decreases with increasing M_a because the E_T^{miss} spectrum becomes softer with M_a , as shown in Fig. 47.

D Studies of other models of scalar sector

E Inert Doublet Model

The Inert Doublet model [79–81] is another intriguing model that extends the scalar sector of the Standard Model, providing dark matter candidates. It contains two scalar doublets Φ_S, Φ_D , redefining five physical states h, H, H^\pm, A , where h corresponds to the Standard Model Higgs particle and all other states originate from the second doublet. An additional Z_2 symmetry is imposed, with the discrete transformations defined as $\phi_D \rightarrow -\phi_D$, $\phi_S \rightarrow \phi_S$, $\text{SM} \rightarrow \text{SM}$. This leads to the following potential.

$$V = -\frac{1}{2} \left[m_{11}^2 (\phi_S^\dagger \phi_S) + m_{22}^2 (\phi_D^\dagger \phi_D) \right] + \frac{\lambda_1}{2} (\phi_S^\dagger \phi_S)^2 + \frac{\lambda_2}{2} (\phi_D^\dagger \phi_D)^2 + \lambda_3 (\phi_S^\dagger \phi_S) (\phi_D^\dagger \phi_D) + \lambda_4 (\phi_S^\dagger \phi_D) (\phi_D^\dagger \phi_S) + \frac{\lambda_5}{2} \left[(\phi_S^\dagger \phi_D)^2 + (\phi_D^\dagger \phi_S)^2 \right], \quad (\text{E.1})$$

with all parameters real (see e.g. [122]). After minimization, the model contains in total 7 free parameters which e.g. can be chosen as $(m_H, m_A, m_{H^\pm}, \lambda_2, \lambda_{345})$, where $\lambda_{345} \equiv$

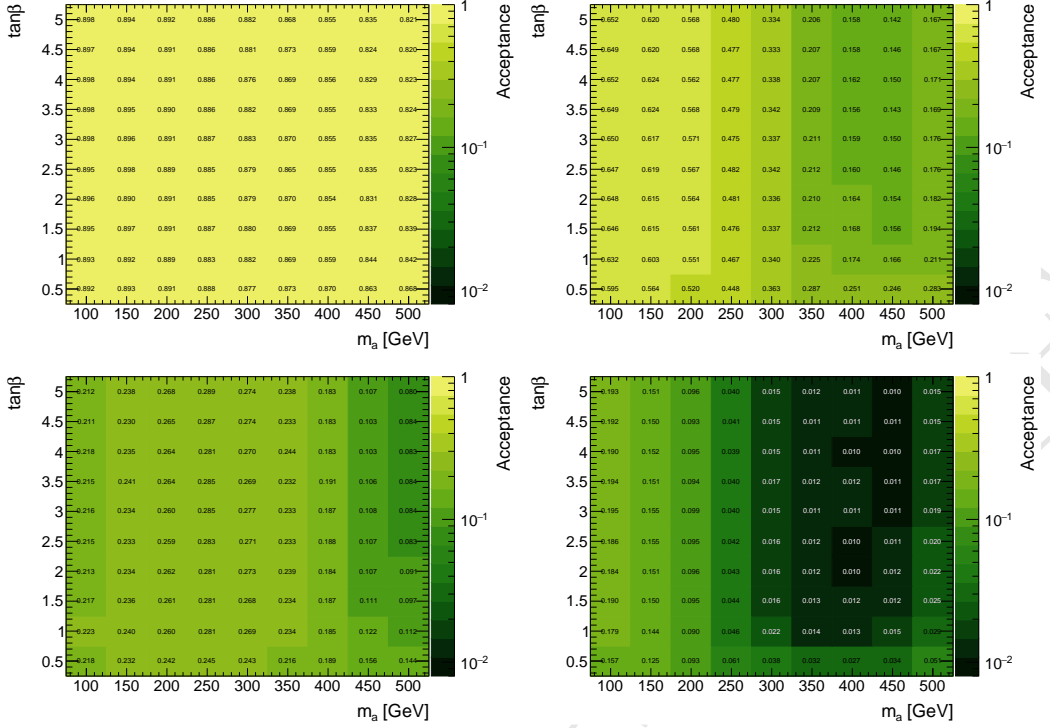


Figure 52: Acceptance for the inclusive (top) and final (bottom) selections for the mono- Z hadronic events $pp \rightarrow Z(\rightarrow q\bar{q})\chi\bar{\chi}$ in the M_a vs $\tan\beta$ grid. Shown on the left (right) is the acceptance for the resolved (boosted) analysis selections. The M_A is fixed to 600 GeV.

$\lambda_3 + \lambda_4 + \lambda_5$. The above Z_2 symmetry renders the lightest of the additional scalars stable, and the model therefore provides a good dark matter candidate. The following discussion focuses on H as the dark matter candidate. The model is subject to a large number of theoretical and experimental constraints, cf. e.g. [82, 86, 90, 91, 123–128] for recent discussions on the allowed parameter space. Most stringent constraints stem from direct detection experiments such as LUX [110] for large parts of the parameter space.

Due to the Z_2 symmetry, all scalars that originate from the second (dark) doublet can only be pair-produced. In addition, these dark scalars do not couple to fermions. The most prominent production channels are therefore Drell-Yan induced processes, i.e. the production of a single W or Z in the s-channel producing a pair of dark scalars. In principle AA final states can also be mediated via an h in the s-channel; however, the according couplings are strongly constrained from direct detection experiments, rendering the according contribution to the total cross section negligible. Therefore, the production cross sections for this model only depend on electroweak couplings as well as the masses of the produced dark scalars. Similarly, the dark scalars dominantly decay via $A \rightarrow ZH$ and $H^\pm \rightarrow W^\pm H$, with electroweak gauge bosons following SM decay patterns.

Total cross sections for scans as well as dedicated parameter points have been presented in [86, 90, 91]. Typical production cross sections for $Z + E_T^{\text{miss}}$ or $W^\pm + E_T^{\text{miss}}$ at the 13 TeV LHC are of the order of 30 fb, where no cuts have been applied. Production cross

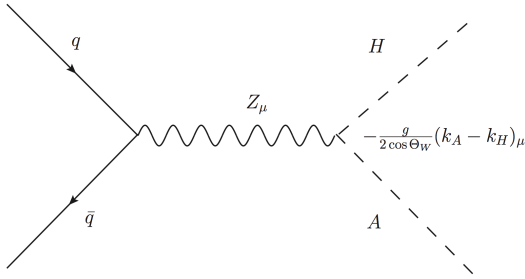


Figure 53: Feynman diagram for $Z + E_T^{\text{miss}}$ final states in the inert doublet model from $H A$ production at a hadron collider, with $A \rightarrow Z H$. Production and decay are determined by electroweak SM couplings and masses m_A, m_H .

sections for diboson final states and E_T^{miss} are suppressed by an additional factor 3-10³.

The UFO model file for the Inert Doublet Model has been presented in [129] and can readily be interfaced with Madgraph to produce event samples at all levels. Collider studies of this model at the LHC as well as a Linear Collider framework have e.g. been discussed in [84, 87–89, 124, 130].

For the most dominant production channels, i.e. mono gauge-boson production with missing energy, the production mode differs from the model discussed above, cf. Figure 53 (the diagram for $H^\pm H$ production is analogous). Both the nature of the s-channel mediator as well as the decay topology differ. Therefore, although final state signatures are identical within the two models, it can be expected that different selection cuts need to be applied for signal enhancement. Possible search strategies can e.g. be adopted from improvements of experimental cuts for supersymmetric searches in multilepton final states (see [85] for a recast of this model using 8 TeV LHC data).

References

- [1] D. Abercrombie et al., *Dark Matter Benchmark Models for Early LHC Run-2 Searches: Report of the ATLAS/CMS Dark Matter Forum*, [arXiv:1507.00966](https://arxiv.org/abs/1507.00966).
- [2] Q.-H. Cao, C.-R. Chen, C. S. Li, and H. Zhang, *Effective Dark Matter Model: Relic density, CDMS II, Fermi LAT and LHC*, *JHEP* **1108** (2011) 018, [[arXiv:0912.4511](https://arxiv.org/abs/0912.4511)].
- [3] M. Beltran, D. Hooper, E. W. Kolb, Z. A. Krusberg, and T. M. Tait, *Maverick dark matter at colliders*, *JHEP* **1009** (2010) 037, [[arXiv:1002.4137](https://arxiv.org/abs/1002.4137)].
- [4] J. Goodman, M. Ibe, A. Rajaraman, W. Shepherd, T. M. Tait, et al., *Constraints on Light Majorana dark Matter from Colliders*, *Phys.Lett.* **B695** (2011) 185–188, [[arXiv:1005.1286](https://arxiv.org/abs/1005.1286)].

³In principle, also monojet searches could render insight on this model. However, the according production cross sections are proportional to λ_{345}^2 . The value of this parameter is highly constrained by direct detection experiments.

- [5] Y. Bai, P. J. Fox, and R. Harnik, *The Tevatron at the Frontier of Dark Matter Direct Detection*, *JHEP* **1012** (2010) 048, [[arXiv:1005.3797](#)].
- [6] J. Goodman, M. Ibe, A. Rajaraman, W. Shepherd, T. M. Tait, et al., *Constraints on Dark Matter from Colliders*, *Phys. Rev.* **D82** (2010) 116010, [[arXiv:1008.1783](#)].
- [7] P. J. Fox, R. Harnik, J. Kopp, and Y. Tsai, *Missing Energy Signatures of Dark Matter at the LHC*, *Phys. Rev.* **D85** (2012) 056011, [[arXiv:1109.4398](#)].
- [8] P. J. Fox, R. Harnik, J. Kopp, and Y. Tsai, *LEP Shines Light on Dark Matter*, *Phys. Rev.* **D84** (2011) 014028, [[arXiv:1103.0240](#)].
- [9] I. M. Shoemaker and L. Vecchi, *Unitarity and Monojet Bounds on Models for DAMA, CoGeNT, and CRESST-II*, *Phys. Rev.* **D86** (2012) 015023, [[arXiv:1112.5457](#)].
- [10] G. Busoni, A. De Simone, E. Morgante, and A. Riotto, *On the Validity of the Effective Field Theory for Dark Matter Searches at the LHC*, *Phys. Lett.* **B728** (2014) 412–421, [[arXiv:1307.2253](#)].
- [11] O. Buchmueller, M. J. Dolan, and C. McCabe, *Beyond Effective Field Theory for Dark Matter Searches at the LHC*, *JHEP* **01** (2014) 025, [[arXiv:1308.6799](#)].
- [12] G. Busoni, A. De Simone, J. Gramling, E. Morgante, and A. Riotto, *On the Validity of the Effective Field Theory for Dark Matter Searches at the LHC, Part II: Complete Analysis for the s-channel*, *JCAP* **1406** (2014) 060, [[arXiv:1402.1275](#)].
- [13] G. Busoni, A. De Simone, T. Jacques, E. Morgante, and A. Riotto, *On the Validity of the Effective Field Theory for Dark Matter Searches at the LHC Part III: Analysis for the t-channel*, *JCAP* **1409** (2014) 022, [[arXiv:1405.3101](#)].
- [14] D. Racco, A. Wulzer, and F. Zwirner, *Robust collider limits on heavy-mediator Dark Matter*, *JHEP* **05** (2015) 009, [[arXiv:1502.04701](#)].
- [15] S. Bruggisser, F. Riva, and A. Urbano, *The Last Gasp of Dark Matter Effective Theory*, *JHEP* **11** (2016) 069, [[arXiv:1607.02475](#)].
- [16] S. Bruggisser, F. Riva, and A. Urbano, *Strongly Interacting Light Dark Matter*, *SciPost Phys.* **3** (2017), no. 3 017, [[arXiv:1607.02474](#)].
- [17] J. Abdallah et al., *Simplified Models for Dark Matter Searches at the LHC*, *Phys. Dark Univ.* **9–10** (2015) 8–23, [[arXiv:1506.03116](#)].
- [18] D. Curtin et al., *Exotic decays of the 125 GeV Higgs boson*, *Phys. Rev.* **D90** (2014), no. 7 075004, [[arXiv:1312.4992](#)].
- [19] U. Haisch, J. F. Kamenik, A. Malinauskas, and M. Spira, *Collider constraints on light pseudoscalars*, *JHEP* **03** (2018) 178, [[arXiv:1802.02156](#)].
- [20] N. F. Bell, Y. Cai, J. B. Dent, R. K. Leane, and T. J. Weiler, *Dark matter at the LHC: Effective field theories and gauge invariance*, *Phys. Rev.* **D92** (2015), no. 5 053008, [[arXiv:1503.07874](#)].
- [21] N. F. Bell, Y. Cai, and R. K. Leane, *Mono-W Dark Matter Signals at the LHC: Simplified Model Analysis*, *JCAP* **1601** (2016), no. 01 051, [[arXiv:1512.00476](#)].
- [22] U. Haisch, F. Kahlhoefer, and T. M. P. Tait, *On Mono-W Signatures in Spin-1 Simplified Models*, *Phys. Lett.* **B760** (2016) 207–213, [[arXiv:1603.01267](#)].
- [23] C. Englert, M. McCullough, and M. Spannowsky, *S-Channel Dark Matter Simplified Models and Unitarity*, *Phys. Dark Univ.* **14** (2016) 48–56, [[arXiv:1604.07975](#)].

- [24] D. Goncalves, P. A. N. Machado, and J. M. No, *Simplified Models for Dark Matter Face their Consistent Completions*, *Phys. Rev.* **D95** (2017), no. 5 055027, [[arXiv:1611.04593](#)].
- [25] M. Bauer, U. Haisch, and F. Kahlhoefer, *Simplified dark matter models with two Higgs doublets: I. Pseudoscalar mediators*, *JHEP* **05** (2017) 138, [[arXiv:1701.07427](#)].
- [26] P. Pani and G. Polesello, *Dark matter production in association with a single top-quark at the LHC in a two-Higgs-doublet model with a pseudoscalar mediator*, *Phys. Dark Univ.* **21** (2018) 8–15, [[arXiv:1712.03874](#)].
- [27] U. Haisch, F. Kahlhoefer, and J. Unwin, *The impact of heavy-quark loops on LHC dark matter searches*, *JHEP* **1307** (2013) 125, [[arXiv:1208.4605](#)].
- [28] P. J. Fox and C. Williams, *Next-to-Leading Order Predictions for Dark Matter Production at Hadron Colliders*, *Phys. Rev.* **D87** (2013) 054030, [[arXiv:1211.6390](#)].
- [29] M. R. Buckley, D. Feld, and D. Goncalves, *Scalar Simplified Models for Dark Matter*, *Phys. Rev.* **D91** (2015) 015017, [[arXiv:1410.6497](#)].
- [30] P. Harris, V. V. Khoze, M. Spannowsky, and C. Williams, *Constraining Dark Sectors at Colliders: Beyond the Effective Theory Approach*, *Phys. Rev.* **D91** (2015) 055009, [[arXiv:1411.0535](#)].
- [31] U. Haisch and E. Re, *Simplified dark matter top-quark interactions at the LHC*, *JHEP* **06** (2015) 078, [[arXiv:1503.00691](#)].
- [32] S. Ipek, D. McKeen, and A. E. Nelson, *A Renormalizable Model for the Galactic Center Gamma Ray Excess from Dark Matter Annihilation*, *Phys. Rev.* **D90** (2014), no. 5 055021, [[arXiv:1404.3716](#)].
- [33] J. M. No, *Looking through the pseudoscalar portal into dark matter: Novel mono-Higgs and mono-Z signatures at the LHC*, *Phys. Rev.* **D93** (2016), no. 3 031701, [[arXiv:1509.01110](#)].
- [34] P. Tunney, J. M. No, and M. Fairbairn, *Probing the pseudoscalar portal to dark matter via $\bar{b}bZ(\rightarrow \ell\ell) + \bar{q}q_T$: From the LHC to the Galactic Center excess*, *Phys. Rev.* **D96** (2017), no. 9 095020, [[arXiv:1705.09670](#)].
- [35] S. L. Glashow and S. Weinberg, *Natural Conservation Laws for Neutral Currents*, *Phys. Rev.* **D15** (1977) 1958.
- [36] E. A. Paschos, *Diagonal Neutral Currents*, *Phys. Rev.* **D15** (1977) 1966.
- [37] **ATLAS, CMS** Collaboration, G. Aad et al., *Measurements of the Higgs boson production and decay rates and constraints on its couplings from a combined ATLAS and CMS analysis of the LHC pp collision data at $\sqrt{s} = 7$ and 8 TeV*, *JHEP* **08** (2016) 045, [[arXiv:1606.02266](#)].
- [38] J. F. Gunion and H. E. Haber, *The CP conserving two Higgs doublet model: The Approach to the decoupling limit*, *Phys. Rev.* **D67** (2003) 075019, [[hep-ph/0207010](#)].
- [39] T. Hermann, M. Misiak, and M. Steinhauser, *$\bar{B} \rightarrow X_s\gamma$ in the Two Higgs Doublet Model up to Next-to-Next-to-Leading Order in QCD*, *JHEP* **11** (2012) 036, [[arXiv:1208.2788](#)].
- [40] M. Misiak et al., *Updated NNLO QCD predictions for the weak radiative B-meson decays*, *Phys. Rev. Lett.* **114** (2015), no. 22 221801, [[arXiv:1503.01789](#)].
- [41] M. Misiak and M. Steinhauser, *Weak radiative decays of the B meson and bounds on M_{H^\pm} in the Two-Higgs-Doublet Model*, *Eur. Phys. J.* **C77** (2017), no. 3 201, [[arXiv:1702.04571](#)].

- [42] L. F. Abbott, P. Sikivie, and M. B. Wise, *Constraints on Charged Higgs Couplings*, *Phys. Rev.* **D21** (1980) 1393.
- [43] C. Q. Geng and J. N. Ng, *Charged Higgs Effect in $B_d^0 - \bar{B}_d^0$ Mixing, $K \rightarrow \pi$ Neutrino Anti-neutrino Decay and Rare Decays of B Mesons*, *Phys. Rev.* **D38** (1988) 2857. [Erratum: *Phys. Rev.* D41, 1715 (1990)].
- [44] A. J. Buras, P. Krawczyk, M. E. Lautenbacher, and C. Salazar, *$B^0 - \bar{B}^0$ Mixing, CP Violation, $K^+ \rightarrow \pi^+ \nu \bar{\nu}$ and $B \rightarrow K\gamma X$ in a Two Higgs Doublet Model*, *Nucl. Phys.* **B337** (1990) 284–312.
- [45] M. Kirk, A. Lenz, and T. Rauh, *Dimension-six matrix elements for meson mixing and lifetimes from sum rules*, *JHEP* **12** (2017) 068, [[arXiv:1711.02100](#)].
- [46] W. Skiba and J. Kalinowski, *$B_s \rightarrow \tau^+ \tau^-$ decay in a two Higgs doublet model*, *Nucl. Phys.* **B404** (1993) 3–19.
- [47] H. E. Logan and U. Nierste, *$B_{s,d} \rightarrow \ell^+ \ell^-$ in a two Higgs doublet model*, *Nucl. Phys.* **B586** (2000) 39–55, [[hep-ph/0004139](#)].
- [48] P. H. Chankowski and L. Slawianowska, *$B_{d,s}^0 \rightarrow \mu^+ \mu^-$ decay in the MSSM*, *Phys. Rev.* **D63** (2001) 054012, [[hep-ph/0008046](#)].
- [49] C. Bobeth, T. Ewerth, F. Krüger, and J. Urban, *Analysis of neutral Higgs boson contributions to the decays $\bar{B}_{(s)} \rightarrow \ell^+ \ell^-$ and $\bar{B} \rightarrow K \ell^+ \ell^-$* , *Phys. Rev.* **D64** (2001) 074014, [[hep-ph/0104284](#)].
- [50] C. Bobeth, M. Gorbahn, T. Hermann, M. Misiak, E. Stamou, and M. Steinhauser, *$B_{s,d} \rightarrow l^+ l^-$ in the Standard Model with Reduced Theoretical Uncertainty*, *Phys. Rev. Lett.* **112** (2014) 101801, [[arXiv:1311.0903](#)].
- [51] **LHCb, CMS** Collaboration, V. Khachatryan et al., *Observation of the rare $B_s^0 \rightarrow \mu^+ \mu^-$ decay from the combined analysis of CMS and LHCb data*, *Nature* **522** (2015) 68–72, [[arXiv:1411.4413](#)].
- [52] **LHCb** Collaboration, R. Aaij et al., *Measurement of the $B_s^0 \rightarrow \mu^+ \mu^-$ branching fraction and effective lifetime and search for $B^0 \rightarrow \mu^+ \mu^-$ decays*, *Phys. Rev. Lett.* **118** (2017), no. 19 191801, [[arXiv:1703.05747](#)].
- [53] A. Denner, R. J. Guth, W. Hollik, and J. H. Kühn, *The Z width in the two Higgs doublet model*, *Z. Phys.* **C51** (1991) 695–705.
- [54] U. Haisch and A. Weiler, *Determining the Sign of the Z⁻ Penguin Amplitude*, *Phys. Rev.* **D76** (2007) 074027, [[arXiv:0706.2054](#)].
- [55] A. Freitas and Y.-C. Huang, *Electroweak two-loop corrections to $\sin^2 \theta_{eff}^{bb}$ and R_b using numerical Mellin-Barnes integrals*, *JHEP* **08** (2012) 050, [[arXiv:1205.0299](#)]. [Erratum: *JHEP* 10, 044 (2013)].
- [56] **ATLAS** Collaboration, M. Aaboud et al., *Search for additional heavy neutral Higgs and gauge bosons in the ditau final state produced in 36 fb⁻¹ of pp collisions at $\sqrt{s} = 13$ TeV with the ATLAS detector*, *JHEP* **01** (2018) 055, [[arXiv:1709.07242](#)].
- [57] **CMS** Collaboration, A. M. Sirunyan et al., *Search for additional neutral MSSM Higgs bosons in the $\tau\tau$ final state in proton-proton collisions at $\sqrt{s} = 13$ TeV*, [arXiv:1803.06553](#).
- [58] **ATLAS** Collaboration, M. Aaboud et al., *Search for Heavy Higgs Bosons A/H Decaying to a Top Quark Pair in pp Collisions at $\sqrt{s} = 8$ TeV with the ATLAS Detector*, *Phys. Rev. Lett.* **119** (2017), no. 19 191803, [[arXiv:1707.06025](#)].

- [59] ATLAS Collaboration, M. Aaboud et al., *Search for pair production of up-type vector-like quarks and for four-top-quark events in final states with multiple b-jets with the ATLAS detector*, [arXiv:1803.09678](#).
- [60] H. E. Haber and A. Pomarol, *Constraints from global symmetries on radiative corrections to the Higgs sector*, *Phys. Lett.* **B302** (1993) 435–441, [[hep-ph/9207267](#)].
- [61] A. Pomarol and R. Vega, *Constraints on CP violation in the Higgs sector from the rho parameter*, *Nucl. Phys.* **B413** (1994) 3–15, [[hep-ph/9305272](#)].
- [62] J. M. Gerard and M. Herquet, *A Twisted custodial symmetry in the two-Higgs-doublet model*, *Phys. Rev. Lett.* **98** (2007) 251802, [[hep-ph/0703051](#)].
- [63] B. Grzadkowski, M. Maniatis, and J. Wudka, *The bilinear formalism and the custodial symmetry in the two-Higgs-doublet model*, *JHEP* **11** (2011) 030, [[arXiv:1011.5228](#)].
- [64] H. E. Haber and D. O’Neil, *Basis-independent methods for the two-Higgs-doublet model III: The CP-conserving limit, custodial symmetry, and the oblique parameters S, T, U*, *Phys. Rev.* **D83** (2011) 055017, [[arXiv:1011.6188](#)].
- [65] ATLAS Collaboration, M. Aaboud et al., *Search for heavy resonances decaying into WW in the $e\nu\mu\nu$ final state in pp collisions at $\sqrt{s} = 13$ TeV with the ATLAS detector*, *Eur. Phys. J.* **C78** (2018), no. 1 24, [[arXiv:1710.01123](#)].
- [66] ATLAS Collaboration, M. Aaboud et al., *Search for heavy ZZ resonances in the $\ell^+\ell^-\ell^+\ell^-$ and $\ell^+\ell^-\nu\bar{\nu}$ final states using protonproton collisions at $\sqrt{s} = 13$ TeV with the ATLAS detector*, *Eur. Phys. J.* **C78** (2018), no. 4 293, [[arXiv:1712.06386](#)].
- [67] CMS Collaboration, A. M. Sirunyan et al., *Search for beyond the standard model Higgs bosons decaying into a $b\bar{b}$ pair in pp collisions at $\sqrt{s} = 13$ TeV*, [arXiv:1805.12191](#).
- [68] ATLAS Collaboration, G. Aad et al., *Constraints on new phenomena via Higgs boson couplings and invisible decays with the ATLAS detector*, *JHEP* **11** (2015) 206, [[arXiv:1509.00672](#)].
- [69] CMS Collaboration, V. Khachatryan et al., *Searches for invisible decays of the Higgs boson in pp collisions at $\text{sqrt}(s) = 7, 8, \text{and } 13$ TeV*, *JHEP* **02** (2017) 135, [[arXiv:1610.09218](#)].
- [70] N. F. Bell, G. Busoni, and I. W. Sanderson, *Self-consistent Dark Matter Simplified Models with an s-channel scalar mediator*, *JCAP* **1703** (2017), no. 03 015, [[arXiv:1612.03475](#)].
- [71] N. F. Bell, G. Busoni, and I. W. Sanderson, *Two Higgs Doublet Dark Matter Portal*, *JCAP* **1801** (2018), no. 01 015, [[arXiv:1710.10764](#)].
- [72] R. Mahbubani and L. Senatore, *The Minimal model for dark matter and unification*, *Phys. Rev.* **D73** (2006) 043510, [[hep-ph/0510064](#)].
- [73] R. Enberg, P. J. Fox, L. J. Hall, A. Y. Papaioannou, and M. Papucci, *LHC and dark matter signals of improved naturalness*, *JHEP* **11** (2007) 014, [[arXiv:0706.0918](#)].
- [74] T. Cohen, J. Kearney, A. Pierce, and D. Tucker-Smith, *Singlet-Doublet Dark Matter*, *Phys. Rev.* **D85** (2012) 075003, [[arXiv:1109.2604](#)].
- [75] C. Cheung and D. Sanford, *Simplified Models of Mixed Dark Matter*, *JCAP* **1402** (2014) 011, [[arXiv:1311.5896](#)].
- [76] A. Berlin, S. Gori, T. Lin, and L.-T. Wang, *Pseudoscalar Portal Dark Matter*, *Phys. Rev.* **D92** (2015) 015005, [[arXiv:1502.06000](#)].
- [77] G. Arcadi, *2HDM portal for Singlet-Doublet Dark Matter*, [arXiv:1804.04930](#).

- [78] M. Bauer, M. Klassen, and V. Tenorth, *Universal Properties of Pseudoscalar Mediators*, [arXiv:1712.06597](#).
- [79] N. G. Deshpande and E. Ma, *Pattern of Symmetry Breaking with Two Higgs Doublets*, *Phys. Rev.* **D18** (1978) 2574.
- [80] R. Barbieri, L. J. Hall, and V. S. Rychkov, *Improved naturalness with a heavy Higgs: An Alternative road to LHC physics*, *Phys. Rev.* **D74** (2006) 015007, [[hep-ph/0603188](#)].
- [81] Q.-H. Cao, E. Ma, and G. Rajasekaran, *Observing the Dark Scalar Doublet and its Impact on the Standard-Model Higgs Boson at Colliders*, *Phys. Rev.* **D76** (2007) 095011, [[arXiv:0708.2939](#)].
- [82] E. Dolle, X. Miao, S. Su, and B. Thomas, *Dilepton Signals in the Inert Doublet Model*, *Phys. Rev.* **D81** (2010) 035003, [[arXiv:0909.3094](#)].
- [83] X. Miao, S. Su, and B. Thomas, *Trilepton Signals in the Inert Doublet Model*, *Phys. Rev.* **D82** (2010) 035009, [[arXiv:1005.0090](#)].
- [84] M. Gustafsson, S. Rydbeck, L. Lopez-Honorez, and E. Lundstrom, *Status of the Inert Doublet Model and the Role of multileptons at the LHC*, *Phys. Rev.* **D86** (2012) 075019, [[arXiv:1206.6316](#)].
- [85] G. Belanger, B. Dumont, A. Goudelis, B. Herrmann, S. Kraml, and D. Sengupta, *Dilepton constraints in the Inert Doublet Model from Run 1 of the LHC*, *Phys. Rev.* **D91** (2015), no. 11 115011, [[arXiv:1503.07367](#)].
- [86] A. Ilnicka, M. Krawczyk, and T. Robens, *Inert Doublet Model in light of LHC Run I and astrophysical data*, *Phys. Rev.* **D93** (2016), no. 5 055026, [[arXiv:1508.01671](#)].
- [87] P. Poulose, S. Sahoo, and K. Sridhar, *Exploring the Inert Doublet Model through the dijet plus missing transverse energy channel at the LHC*, *Phys. Lett.* **B765** (2017) 300–306, [[arXiv:1604.03045](#)].
- [88] A. Datta, N. Ganguly, N. Khan, and S. Rakshit, *Exploring collider signatures of the inert Higgs doublet model*, *Phys. Rev.* **D95** (2017), no. 1 015017, [[arXiv:1610.00648](#)].
- [89] M. Hashemi and S. Najjari, *Observability of Inert Scalars at the LHC*, *Eur. Phys. J.* **C77** (2017), no. 9 592, [[arXiv:1611.07827](#)].
- [90] **LHC Higgs Cross Section Working Group** Collaboration, D. de Florian et al., *Handbook of LHC Higgs Cross Sections: 4. Deciphering the Nature of the Higgs Sector*, [arXiv:1610.07922](#).
- [91] A. Belyaev, G. Cacciapaglia, I. P. Ivanov, F. Rojas-Abatte, and M. Thomas, *Anatomy of the Inert Two Higgs Doublet Model in the light of the LHC and non-LHC Dark Matter Searches*, *Phys. Rev.* **D97** (2018), no. 3 035011, [[arXiv:1612.00511](#)].
- [92] B. Dutta, G. Palacio, J. D. Ruiz-Alvarez, and D. Restrepo, *Vector Boson Fusion in the Inert Doublet Model*, *Phys. Rev.* **D97** (2018), no. 5 055045, [[arXiv:1709.09796](#)].
- [93] S. von Buddenbrock, N. Chakrabarty, A. S. Cornell, D. Kar, M. Kumar, T. Mandal, B. Mellado, B. Mukhopadhyaya, R. G. Reed, and X. Ruan, *Phenomenological signatures of additional scalar bosons at the LHC*, *Eur. Phys. J.* **C76** (2016), no. 10 580, [[arXiv:1606.01674](#)].
- [94] **ATLAS** Collaboration, M. Aaboud et al., *Search for dark matter in association with a Higgs boson decaying to two photons at $\sqrt{s} = 13$ TeV with the ATLAS detector*, *Phys. Rev.* **D96** (2017), no. 11 112004, [[arXiv:1706.03948](#)].

- [95] **ATLAS** Collaboration, G. Aad et al., *Observation of a new particle in the search for the Standard Model Higgs boson with the ATLAS detector at the LHC*, *Phys. Lett.* **B716** (2012) 1–29, [[arXiv:1207.7214](#)].
- [96] **CMS** Collaboration, S. Chatrchyan et al., *Observation of a new boson at a mass of 125 GeV with the CMS experiment at the LHC*, *Phys. Lett.* **B716** (2012) 30–61, [[arXiv:1207.7235](#)].
- [97] L. Carpenter, A. DiFranzo, M. Mulhearn, C. Shimmin, S. Tulin, et al., *Mono-Higgs: a new collider probe of dark matter*, *Phys. Rev.* **D89** (2014) 075017, [[arXiv:1312.2592](#)].
- [98] A. A. Petrov and W. Shepherd, *Searching for dark matter at LHC with Mono-Higgs production*, *Phys. Lett.* **B730** (2014) 178–183, [[arXiv:1311.1511](#)].
- [99] **ATLAS** Collaboration, M. Aaboud et al., *Search for Dark Matter Produced in Association with a Higgs Boson Decaying to $b\bar{b}$ using 36 fb^{-1} of pp collisions at $\sqrt{s} = 13 \text{ TeV}$ with the ATLAS Detector*, [arXiv:1707.01302](#).
- [100] L. M. Carpenter, A. Nelson, C. Shimmin, T. M. Tait, and D. Whiteson, *Collider searches for dark matter in events with a Z boson and missing energy*, [arXiv:1212.3352](#).
- [101] N. F. Bell, J. B. Dent, A. J. Galea, T. D. Jacques, L. M. Krauss, et al., *Searching for dark matter at the LHC with a mono-Z*, *Phys. Rev.* **D86** (2012) 096011, [[arXiv:1209.0231](#)].
- [102] **ATLAS** Collaboration, M. Aaboud et al., *Search for an invisibly decaying Higgs boson or dark matter candidates produced in association with a Z boson in pp collisions at $\sqrt{s} = 13 \text{ TeV}$ with the ATLAS detector*, *Phys. Lett.* **B776** (2018) 318–337, [[arXiv:1708.09624](#)].
- [103] **CMS** Collaboration, A. M. Sirunyan et al., *Search for new physics in events with a leptonically decaying Z boson and a large transverse momentum imbalance in proton-proton collisions at $\sqrt{s} = 13 \text{ TeV}$* , [arXiv:1711.00431](#).
- [104] M. Backovic, M. Krämer, F. Maltoni, A. Martini, K. Mawatari, and M. Pellen, *Higher-order QCD predictions for dark matter production at the LHC in simplified models with s-channel mediators*, *Eur. Phys. J.* **C75** (2015), no. 10 482, [[arXiv:1508.05327](#)].
- [105] U. Haisch, P. Pani, and G. Polesello, *Determining the CP nature of spin-0 mediators in associated production of dark matter and $t\bar{t}$ pairs*, [arXiv:1611.09841](#).
- [106] G. Cowan, *Discovery sensitivity for a counting experiment with background uncertainty*, tech. rep., Royal Holloway, London, (2012). Available [online] <http://www.pp.rhul.ac.uk/~cowan/stat/medsig/medsigNote.pdf>.
- [107] A. Albert et al., *Recommendations of the LHC Dark Matter Working Group: Comparing LHC searches for heavy mediators of dark matter production in visible and invisible decay channels*, [arXiv:1703.05703](#).
- [108] M. Backovic, K. Kong, and M. McCaskey, *MadDM v.1.0: Computation of Dark Matter Relic Abundance Using MadGraph5*, *Physics of the Dark Universe* **5-6** (2014) 18–28, [[arXiv:1308.4955](#)].
- [109] M. Backovic, A. Martini, O. Mattelaer, K. Kong, and G. Mohlabeng, *Direct Detection of Dark Matter with MadDM v.2.0*, *Phys. Dark Univ.* **9-10** (2015) 37–50, [[arXiv:1505.04190](#)].
- [110] **LUX** Collaboration, D. S. Akerib et al., *Results from a search for dark matter in the complete LUX exposure*, *Phys. Rev. Lett.* **118** (2017), no. 2 021303, [[arXiv:1608.07648](#)].
- [111] **XENON** Collaboration, E. Aprile et al., *First Dark Matter Search Results from the XENON1T Experiment*, [arXiv:1705.06655](#).

- [112] M. Cirelli, E. Del Nobile, and P. Panci, *Tools for model-independent bounds in direct dark matter searches*, *JCAP* **1310** (2013) 019, [[arXiv:1307.5955](#)].
- [113] **XENON** Collaboration, E. Aprile et al., *Physics reach of the XENON1T dark matter experiment*, *JCAP* **1604** (2016), no. 04 027, [[arXiv:1512.07501](#)].
- [114] J. Billard, L. Strigari, and E. Figueroa-Feliciano, *Implication of neutrino backgrounds on the reach of next generation dark matter direct detection experiments*, *Phys. Rev.* **D89** (2014), no. 2 023524, [[arXiv:1307.5458](#)].
- [115] M. Backovic, A. Martini, K. Kong, O. Mattelaer, and G. Mohlabeng, *MadDM: New dark matter tool in the LHC era*, *AIP Conf. Proc.* **1743** (2016) 060001, [[arXiv:1509.03683](#)].
- [116] L. M. Carpenter, R. Colburn, J. Goodman, and T. Linden, *Indirect Detection Constraints on s and t Channel Simplified Models of Dark Matter*, *Phys. Rev.* **D94** (2016), no. 5 055027, [[arXiv:1606.04138](#)].
- [117] L. M. Carpenter, R. Colburn, and J. Goodman, *Indirect Detection Constraints on the Model Space of Dark Matter Effective Theories*, *Phys. Rev.* **D92** (2015), no. 9 095011, [[arXiv:1506.08841](#)].
- [118] G. Elor, N. L. Rodd, T. R. Slatyer, and W. Xue, *Model-Independent Indirect Detection Constraints on Hidden Sector Dark Matter*, *JCAP* **1606** (2016), no. 06 024, [[arXiv:1511.08787](#)].
- [119] J. Alwall, R. Frederix, S. Frixione, V. Hirschi, F. Maltoni, O. Mattelaer, H. S. Shao, T. Stelzer, P. Torrielli, and M. Zaro, *The automated computation of tree-level and next-to-leading order differential cross sections, and their matching to parton shower simulations*, *JHEP* **07** (2014) 079, [[arXiv:1405.0301](#)].
- [120] C. Degrande, C. Duhr, B. Fuks, D. Grellscheid, O. Mattelaer, and T. Reiter, *UFO - The Universal FeynRules Output*, *Comput. Phys. Commun.* **183** (2012) 1201–1214, [[arXiv:1108.2040](#)].
- [121] **NNPDF** Collaboration, R. D. Ball et al., *Parton distributions for the LHC Run II*, *JHEP* **04** (2015) 040, [[arXiv:1410.8849](#)].
- [122] I. Ginzburg, K. Kanishev, M. Krawczyk, and D. Sokolowska, *Evolution of Universe to the present inert phase*, *Phys. Rev.* **D82** (2010) 123533, [[arXiv:1009.4593](#)].
- [123] B. Swiezewska and M. Krawczyk, *Diphoton rate in the inert doublet model with a 125 GeV Higgs boson*, *Phys. Rev.* **D88** (2013), no. 3 035019, [[arXiv:1212.4100](#)].
- [124] A. Arhrib, Y.-L. S. Tsai, Q. Yuan, and T.-C. Yuan, *An Updated Analysis of Inert Higgs Doublet Model in light of the Recent Results from LUX, PLANCK, AMS-02 and LHC*, *JCAP* **1406** (2014) 030, [[arXiv:1310.0358](#)].
- [125] M. Krawczyk, D. Sokolowska, P. Swaczyna, and B. Swiezewska, *Constraining Inert Dark Matter by $R_{\gamma\gamma}$ and WMAP data*, *JHEP* **1309** (2013) 055, [[arXiv:1305.6266](#)].
- [126] M. A. Diaz, B. Koch, and S. Urrutia-Quiroga, *Constraints to Dark Matter from Inert Higgs Doublet Model*, *Adv. High Energy Phys.* **2016** (2016) 8278375, [[arXiv:1511.04429](#)].
- [127] A. Ilnicka, M. Krawczyk, T. Robens, and D. Sokolowska, *IDM and not only*, *PoS CORFU2016* (2017) 030, [[arXiv:1705.00225](#)].
- [128] B. Eiteneuer, A. Goudelis, and J. Heisig, *The inert doublet model in the light of Fermi-LAT gamma-ray data: a global fit analysis*, *Eur. Phys. J.* **C77** (2017), no. 9 624, [[arXiv:1705.01458](#)].

- [129] A. Goudelis, B. Herrmann, and O. Stal, *Dark matter in the Inert Doublet Model after the discovery of a Higgs-like boson at the LHC*, *JHEP* **1309** (2013) 106, [[arXiv:1303.3010](https://arxiv.org/abs/1303.3010)].
- [130] M. Hashemi, M. Krawczyk, S. Najjari, and A. F. arnecki, *Production of Inert Scalars at the high energy e^+e^- colliders*, [arXiv:1512.01175](https://arxiv.org/abs/1512.01175). [JHEP02,187(2016)].